Beam Phase Feedback in a Heavy-Ion Synchrotron with Dual-Harmonic Cavity System

Vom Fachbereich
Elektrotechnik und Informationstechnik
der Technischen Universität Darmstadt
zur Erlangung des akademischen Grades
eines Doktor-Ingenieurs (Dr.-Ing.)
genehmigte Dissertation

von

Dipl.-Ing. Jochen M. Grieser

geboren am 5. April 1984 in Göppingen

Referent:	Prof. Dr.-Ing. J. Adamy
Korreferent:	Prof. Dr.-Ing. H. Klingbeil
Tag der Einreichung:	16. September 2014
Tag der mündlichen Prüfung:	17. Dezember 2014

D17
Darmstadt 2015

Für Rolf und Gudrun.

Vorwort

Die vorliegende Arbeit entstand während meiner Tätigkeit als wissenschaftlicher Mitarbeiter am Fachgebiet Regelungsmethoden und Robotik der Technischen Universität Darmstadt. Bei Professor Jürgen Adamy möchte ich mich herzlich dafür bedanken, dass er mir die Bearbeitung dieses spannenden Promotionsthemas an seinem Fachgebiet ermöglicht hat. Seine Unterstützung und sein Vertrauen haben ebenso wie die sehr angenehmen Arbeitsbedingungen am Fachgebiet wesentlich zum Gelingen meiner Promotion beigetragen.

Des Weiteren danke ich Professor Harald Klingbeil für die Übernahme des Koreferats. Ihm verdanke ich durch sein Engagement nicht nur die Möglichkeit, mich im Rahmen der Kooperation mit dem GSI Helmholtzzentrum für Schwerionenforschung mit dem spannenden Thema der Beschleunigertechnik auseinandersetzen zu können, sondern er stand mir auch stets mit Rat und Tat zur Seite.

Viel Unterstützung, insbesondere bei der Durchführung der Strahlexperimente, habe ich auch durch die Abteilung Ring-HF der GSI erhalten, vor allem durch Kerstin Groß, Uta Hartel, Ulrich Laier, Dieter Lens, Klaus-Peter Ningel, Stefan Schäfer und Bernhard Zipfel.

Meine Arbeit am Fachgebiet wurde wesentlich erleichtert durch Birgit Heid, Sylvia Gelman und Susanne Muntermann, die mir bei administrativen und technischen Fragen stets eine große Hilfe waren, sowie durch die fachliche Unterstützung meiner vielen Kollegen, von denen ich stellvertretend Dieter Lens und Kerstin Groß hervorheben möchte. Unsere fachlichen Diskussionen haben mir den Einstieg in die Materie sehr erleichtert und bis zum Abschluss meiner Arbeit stets geholfen.

Valentina Ansel danke ich für die Anfertigung mehrerer Grafiken, die ich in dieser Arbeit verwenden durfte, und dafür, dass sie stets ein offenes Ohr für mich hat.

Für die kritische Durchsicht der Arbeit danke ich Dieter Lens, Benjamin Reichardt, Stefan Klingelschmitt und Armin Grieser.

Meiner Familie und meinen Freunden danke ich für ihre Unterstützung im Studium und während meiner Promotion, insbesondere meinen Eltern

und meinem Bruder, sowie Annika für all das Schöne, das durch sie in mein Leben kam.

Jochen Michael Grieser, Stuttgart, im März 2015

Contents

List of Symbols

Some symbols are used for more than one quantity which is made clear in the respective context. A multiple used symbol is listed in the following in more than one category. Furthermore only frequently used symbols are listed.

Abbreviations

AGS	Alternating Gradient Synchrotron at BNL
AWG	arbitrary wave generator
BNL	Brookhaven National Laboratory
BPM	beam position monitor
CCR	central control room
CEL	calibration electronics
CERN	Conseil Européen pour la Recherche Nucléaire
DDS	direct digital synthesizer
DSP	digital signal processor
FCT	fast current transformer
FAIR	Facility for Antiproton and Ion Research at GSI
Fermilab	Fermi National Accelerator Laboratory
FOH	fiber optical hub
FPGA	field programmable gate array
GSI	GSI Helmholtzzentrum für Schwerionenforschung GmbH
LMI	linear matrix inequality
PID controller	proportional/integral/derivative controller
PS Booster	proton synchrotron booster at CERN
RF	radio frequency
RHIC	Relativistic Heavy Ion Collider at BNL
SIS18	Schwerionensynchrotron 18 (Heavy-Ion Synchrotron 18) at GSI
SIS100/300	Schwerionensynchrotron 100/300, new FAIR synchrotron at GSI

SNR	signal-to-noise ratio

General Notations

x	scalar
$\boldsymbol{x}$	column vector
$\boldsymbol{x}^{\mathrm{T}}$	row vector
x_i	element i of vector $\boldsymbol{x}$
$\boldsymbol{X}$	matrix
$\boldsymbol{X} = \mathrm{diag}\,(x_1,\ \ldots\ x_n)$	diagonal matrix of elements $x_1\ ,\ \ldots\ ,\ x_n$
$\bar{\boldsymbol{X}}$	complex conjugate of $\boldsymbol{X}$
$\boldsymbol{X}^* = \bar{\boldsymbol{X}}^{\mathrm{T}}$	adjoint (complex transposed) of $\boldsymbol{X}$
$\Delta\boldsymbol{x}$	deviation of reference or nominal value
$\boldsymbol{X} \succ \boldsymbol{0} (\prec \boldsymbol{0})$	positive (negative) definiteness of matrix $\boldsymbol{X}$
$\tilde{x}$, $\tilde{\boldsymbol{x}}$	normalized coordinate or value
t	continuous time variable
k	discrete time variable
z	complex variable of the z-transform
$\boldsymbol{I}_{\mathrm{n}}$	identity matrix of dimension n
$\boldsymbol{o}$, $\boldsymbol{O}$	vector or matrix containing only ones
$\mathbb{R}$, $\mathbb{C}$	space of real and complex numbers
$\Re(x)$	real part of complex number x
$\Im(x)$	imaginary part of complex number x
j	imaginary unit, $j^2 = -1$
$\mathrm{int}(x)$	nearest integer to x
$\dim(\boldsymbol{x})$	dimension (number of elements) of vector $\boldsymbol{x}$
$\mathrm{E}(\boldsymbol{x})$	expected value

Physical Constants

c	speed of light in vacuum, $c = 299\,792\,458\,\mathrm{m/s}$
e	elementary charge, $e = 1.602\,176\,565 \cdot 10^{-19}\,\mathrm{C}$
ϵ_0	electric constant, $\epsilon_0 = 8.854\,187\,817\,620... \cdot 10^{-12}\ \frac{\mathrm{As}}{\mathrm{Vm}}$
$\mu_0 = \frac{1}{c^2 \epsilon_0}$	magnetic constant, $\mu_0 = 4\pi \cdot 10^{-7}\ \frac{\mathrm{Vs}}{\mathrm{Am}}$
$Z_0 = \sqrt{\mu_0 / \epsilon_0}$	vacuum impedance, $Z_0 = 376.7\,\Omega$

Parameters in Relation to Synchrotron and Beam

R	subscript for reference value
B	subscript for bunch barycenter
λ	longitudinal particle line density
E	total energy
E_{kin}	kinetic energy
f_{syn}	synchrotron frequency of single particle
$f_{\mathrm{syn,coh}}$	coherent synchrotron frequency, i. e. synchrotron frequency of coherent oscillation due to disturbance
$f_{\mathrm{syn,0}}$	coherent synchrotron frequency of linearized single-harmonic bucket
$f_{\mathrm{R}} = \frac{1}{T_{\mathrm{R}}}$	revolution frequency of reference particle
f_{RF}	radio frequency of cavity voltage
h	harmonic number
L	orbit length along beam pipe, for SIS18: $L_{\mathrm{R}} = 216.72\,\mathrm{m}$
p	momentum
q	particle charge
$\hat{V}_i$	voltage amplitude of cavity i
$\boldsymbol{v}$	velocity
$\beta = \frac{v}{c}$	ratio of velocity to speed of light
$\gamma = \sqrt{\frac{1}{1-\beta^2}}$	Lorentz factor
γ_{t}	Lorentz factor at transition energy, machine parameter
$\eta = \frac{1}{\gamma_{\mathrm{t}}^2} - \frac{1}{\gamma^2}$	phase slip factor
$\kappa_1 = \frac{\omega_{\mathrm{RF}}^2 \eta_{\mathrm{R}}}{\beta_{\mathrm{R}}^2 E_{\mathrm{R}}}$	modeling parameter
$\kappa_2 = \frac{q\hat{V}_1}{2\pi h}$	modeling parameter
ψ	adjustable phase shift between voltages of cavity 1 and cavity 2
$\Delta\varphi_{\mathrm{sx}}$, ΔW_{sx}	relative phase and normalized energy deviation of separatrix
N	number of particles in one bunch
Z_{sp}	space charge impedance
Z_{rw}	resistive wall impedance

$\sum Z_{\mathrm{res}}$	resonator impedance
a, b	beam and pipe radius
g_0	geometry factor
$\mathcal{H}$	Hamiltonian function
$\mathcal{L}$	Lagrange function
$m_{n_\mathrm{x},n_\mathrm{y}}$	raw moment of order $n = n_\mathrm{x} + n_\mathrm{y}$
$\mu_{n_\mathrm{x},n_\mathrm{y}}$	central moment of order $n = n_\mathrm{x} + n_\mathrm{y}$

Coordinates (spatial and in phase space)

z, $\boldsymbol{e}_z$	longitudinal axis with unit vector
x, $\boldsymbol{e}_x$ / y, $\boldsymbol{e}_y$	transverse axes with unit vectors
ϕ	absolute longitudinal phase
φ	longitudinal phase, relative to voltage zero crossing
τ	arrival time, relative to voltage zero crossing
$\Delta E = E - E_\mathrm{R}$	energy deviation with respect to reference energy
$\Delta W = \frac{\Delta E}{\omega_\mathrm{RF}}$	normalized energy deviation

Control Theory

$\boldsymbol{x}$, $\boldsymbol{y}$, $\boldsymbol{u}$	state, output and input variables of a system
n, q, p	dimension of state, output and input variable of a system
z	measurement offset
$\boldsymbol{A}$, $\boldsymbol{B}$, $\boldsymbol{C}$, $\boldsymbol{D}$	system matrix, input matrix, output matrix, feedthrough matrix
$\boldsymbol{G}(z)$, $\boldsymbol{g}(z)$	transfer matrix, transfer vector
$\boldsymbol{E}$	system matrix of descriptor system
$\boldsymbol{k}^T$	controller gain of output or state feedback
$\boldsymbol{l}$	observer gain
$\boldsymbol{\lambda}$	poles of a system
$\Delta\varphi_\mathrm{u}$	phase shift (actuating variable) to damp dipole oscillations
$h(t)$, $H(\omega)$	impulse response and frequency response of filter in the feedback loop
K	gain of filters in the feedback loop
T_s	sampling period

f_s	sampling frequency
N	number of output measurements which are fed back
$\boldsymbol{R}$	Lyapunov matrix
ϑ	adjustable phase shift of matched filter to compensate time delays
f_pass	passing frequency of filter in the feedback loop

Abstract

This dissertation contributes to the design and analysis of bunch phase feedback systems in a heavy-ion synchrotron which is operated with a dual-harmonic cavity system.

Due to the ring structure of the synchrotron the particles are focused in transverse and longitudinal direction forming particle bunches, which may be subject to various disturbances. Depending on the disturbance, bunch oscillations may occur, which lower the beam quality and may also lead to particle loss. This compromises the efforts which are constantly taken to increase the beam intensity, energy and quality. Thus, control measures are taken to stabilize the beam, which are usually based on the linearized single particle dynamics. In the present case, however, the accelerating voltage is supplied by two cavities running with different frequencies, introducing an additional nonlinearity, and simple linearization of the voltage is no longer possible.

The problem of modeling and damping of rigid dipole oscillations in case of a dual-harmonic cavity system is treated here by deriving a simple linear model based on central moments, which is accurate enough to serve as a base for various control design approaches. Beside the feedback already existing at GSI Helmholtzzentrum für Schwerionenforschung GmbH for single-harmonic operation based on a finite impulse response filter, which is transferred here to the dual-harmonic case, an alternative filter design for the feedback is presented, along with different output controllers based on pole placement and a state feedback combined with an observer.

The effectiveness of the feedback with a finite impulse response filter was demonstrated in two beam experiments, which are also presented in this dissertation.

Kurzfassung

Die vorliegende Doktorarbeit leistet einen Beitrag zur Analyse und zum Entwurf von Strahlphasenregelungen in einem Schwerionensynchrotron, das mit einem doppeltharmonischen Kavitätensystem betrieben wird.

Aufgrund der Ringstruktur des Synchrotrons werden die Teilchen in transversaler und longitudinaler Richtung fokussiert, wodurch sich Teilchenwolken bilden, die verschiedenen Störungen ausgesetzt sein können. Abhängig von der Störung können Strahlschwingungen auftreten, welche die Strahlqualität verringern und eventuell zu Teilchenverlust führen. Dies läuft dem Bestreben zuwider, die Strahlintensität, -energie und -qualität fortwährend zu erhöhen. Um den Strahl zu stabilisieren werden daher Regelungsmaßnahmen ergriffen, die im Allgemeinen auf einer Linearisierung der Dynamik eines einzelnen Teilchens basieren. Im vorliegenden Fall setzt sich die beschleunigende Spannung allerdings aus den Teilspannungen zweier Kavitäten zusammen, welche mit unterschiedlichen Frequenzen betrieben werden, wodurch eine weitere Nichtlinearität in der Strecke auftritt und eine Linearisierung der Spannung unmöglich wird.

Dem Problem der Modellierung und der Dämpfung starrer Dipolschwingungen im Falle eines doppeltharmonischen Kavitätensystems wird hier durch die Herleitung eines einfachen linearen Modells basierend auf zentralen Momenten begegnet, welches akkurat genug ist, um als Grundlage für verschiedene Reglerentwürfe zu dienen. Neben der bereits am GSI Helmholtzzentrum für Schwerionenforschung GmbH für den einfachharmonischen Betrieb bestehenden Regelung, basierend auf einem Filter mit endlicher Impulsantwort, welche im Rahmen dieser Arbeit auf den doppeltharmonischen Fall übertragen wird, wird ein alternativer Filterentwurf vorgestellt, sowie verschiedene auf einer Polvorgabe beruhende Ausgangsrückführungen und eine Zustandsrückführung in Kombination mit einem Beobachter.

Die Effektivität der Regelung basierend auf einem Filter mit endlicher Impulsantwort wurde anhand zweier Strahlexperimente demonstriert, welche ebenfalls in der vorliegenden Arbeit vorgestellt werden.

1 Introduction

All men by nature desire knowledge.
- Aristotle (384 BC - 322 BC), *Metaphysics, bk. 1, ch. 1*

For centuries it has been a need of mankind to understand the physics behind our environment and the world we live in for which increasing efforts are taken. An important role in this scientific process is played by particle accelerators. They were not only used in the beginning of modern experimental physics, e. g. for the discovery of X-rays, but nowadays also allow an insight into the structure of matter by supplying particle beams at very high energies [84].

Modern particle accelerators are built since the beginning of the 20th century and are by now used in various fields covering e. g. physical, medicinal and biological research areas, cancer treatment and several industrial applications like ion implantation for the production of semiconductor devices, material irradiation, nondestructive inspection and many more, cf. e. g. [28, 36, 37, 74]. Common accelerators can be clustered in three groups: linear accelerators with DC or RF (radio frequency) voltages and circular accelerators. An overview on the historical development of accelerators, different accelerator types and their applications can be found e. g. in [41, 61, 99]. Linear accelerators with DC voltages are simple to construct but have the disadvantage that the particle energies which can be reached are limited as the maximum voltage is limited by the electrical insulation material. Linear accelerators with RF voltages can reach higher energies but require huge lengths of up to several kilometers like the linear accelerator at *SLAC National Accelerator Laboratory* in Menlo Park, California [75]. Circular accelerators can overcome this drawback by using the same voltage multiple times to accelerate the beam, although the number of turns can be limited (e. g. in a cyclotron [61]).

A theoretically unlimited number of turns can be accomplished in a synchrotron, a ring accelerator characterized by a constant reference orbit making it necessary to focus the beam during the whole acceleration cycle in transverse (perpendicular to the beam orbit) as well as in longitudinal direction (along the beam orbit). Transverse focusing is realized by

magnetic fields in the *quadrupole magnets* while longitudinal (or phase) focusing is accomplished by an electric well created in one or more *cavities*. Deviations of the single particles from the reference orbit will thus lead to incoherent oscillations instead of particle loss.

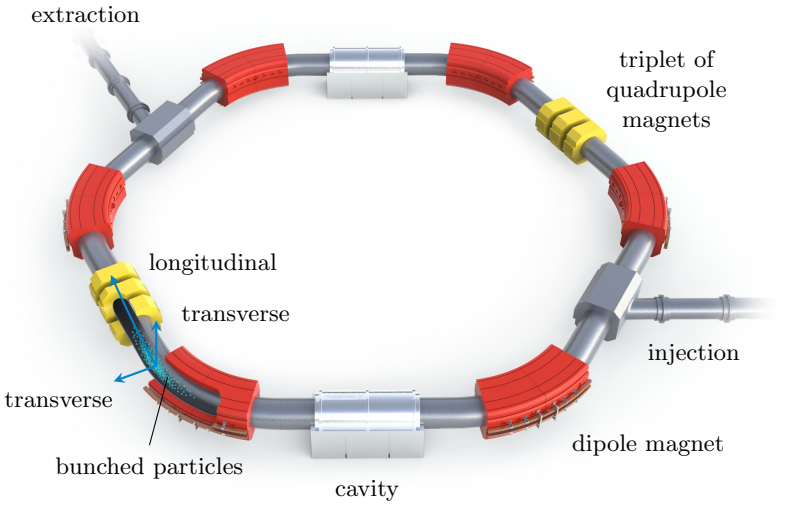

Figure 1.1: Simplified scheme of a synchrotron with illustration of the transverse and longitudinal axes

The synchrotron was proposed independently in 1945 by E. M. McMillan [73] and V. I. Veksler [96], whose discovery of the phase focusing principle led to the construction of the *Cosmotron* at the *Brookhaven National Laboratory* in 1952, the first weak-focusing proton synchrotron [61]. Weak-focusing means that the beam is only weakly focused in transverse direction, only allowing low beam intensities. In the same year however the strong-focusing principle was discovered by E. D. Courant, H. S. Snyder and M. S. Livingston, combining focusing and defocusing magnets [26].

Fig. 1.1 shows a simplified scheme of a synchrotron. The *dipole magnets* are used to bend the particle beam orbit. Only two triplets [1] of the quadrupole magnets are shown, which in reality are present along the whole circumference. In addition also higher order magnets can occur

[1] Also other set-ups than triplets are possible.

which were omitted in the illustration. The cavities provide the acceleration voltages and the already mentioned phase focusing. Due to phase focusing the particle beam is *bunched*. Although the particle bunches are usually much longer, only a short bunch is shown in Fig. 1.1 for sake of lucidity. The magnetic fields created by dipole and quadrupole magnets are shown in Fig. 1.2.

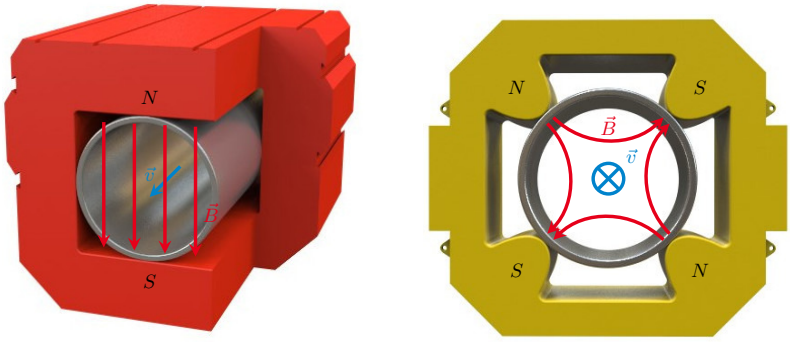

(a) Scheme of dipole magnet to bend the particle orbit

(b) Scheme of quadrupole magnet focusing in vertical and defocusing in horizontal direction (for positively charged particles)

Figure 1.2: Dipole and quadrupole magnets in a synchrotron

Since the dawn of accelerator physics huge efforts have been taken to increase beam intensities, maximum energies and beam quality making synchrotrons one of the most complex research facilities. Due to this development the stabilization of particle beams becomes more and more important. In addition to the incoherent oscillation of single particles, disturbances of the beam may lead to undesired coherent oscillations which result in a lower beam quality or even in beam loss. Disturbances cannot only occur because of inaccurate beam processing, or errors or noise in the electromagnetic fields, but also because of the interaction of the charged particles with their environment, which becomes more important at higher beam intensities [23]. Furthermore, interaction of the particles with each other due to their electrical charge (*space charge*) is usually blamed for the loss of damping effects (cf. e. g. [15]), which is however controversially discussed in literature (cf. e. g. [76]). As the requirements for both, better beam qualities and higher intensities are increasing, stabilizing controllers

become more and more essential.

1.1 Objectives, Contribution and Structure of the Dissertation

This dissertation contributes to the development of the new *Facility for Antiproton and Ion Research* (FAIR), which is currently under construction at *GSI Helmholtzzentrum für Schwerionenforschung GmbH* (short: GSI) [2] [1, 27]. After its completion the existing synchrotron SIS18 [3] will be used as a pre-accelerator for the new synchrotron SIS100/300, and the standard operation mode of its cavity system will be switched from single-harmonic (both cavities running with the same frequency) to dual-harmonic (second cavity running with double frequency). In a single-harmonic cavity system the voltage strictly focuses the particles around the reference point. The dual-harmonic voltage under consideration in this dissertation however is characterized by a saddle point in the phase-voltage diagram introducing a drift section where no phase focusing is present, leading to a lengthening of the particle bunch (*bunch lengthening mode, BLM*). As the particle beam may be subject to various disturbances, beam oscillations may occur which lower the beam quality and may lead to particle loss. Beam oscillations are therefore usually damped by a beam feedback system whose design is based on a linear model of the beam oscillations. The classical modeling approach used in the single-harmonic case is to linearize the voltage around the reference point to obtain a linear oscillator, which is however no longer valid in the dual-harmonic case due to the introduced nonlinearity in the combined cavity voltage. This rises the question about how to design the controller and how to analyze stability if a dual-harmonic cavity system is present.

The dissertation is structured as follows and as depicted in Fig. 1.3.

In Chap. 2 the fundamentals of longitudinal single-particle dynamics are reviewed. After a detailed introduction to synchrotron oscillation the characteristics of the dual-harmonic cavity system are discussed. In addition, a brief overview on the procedure of an acceleration cycle is given before the chapter ends with a discussion.

[2] Planckstraße 1, 64291 Darmstadt, `www.gsi.de`

[3] SIS18 stands for Schwerionensynchrotron 18, named after its maximum magnetic rigidity $B_{\max} \cdot \rho = 1.8\,\mathrm{T} \cdot 10\,\mathrm{m}$, the maximum magnetic field times the bending radius of the dipole magnets.

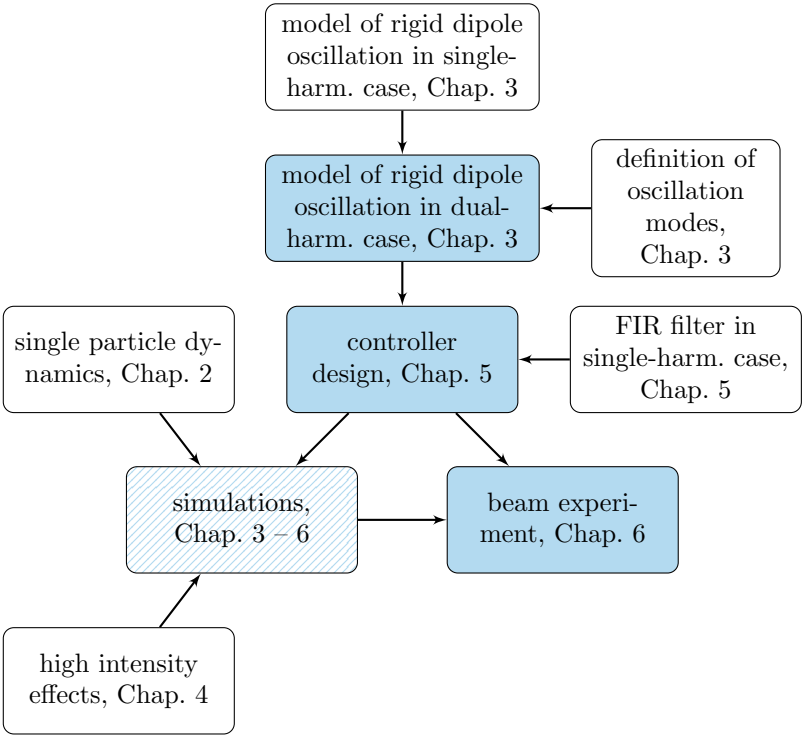

Figure 1.3: Structure of the dissertation. Contributions are marked blue, and patterned if only partly new developed; existing theory is not colored.

Chap. 3 is concerned with the dynamics of coherent bunch motion and reviews properties of particle bunches, filamentation and Landau damping. Furthermore, a modeling approach based on central moments of a distribution function of the particles in phase space is presented which was first proposed for heavy-ion synchrotrons and successfully applied to single-harmonic cavity systems in [62]. Linearizing the obtained state space model about a reference point yields a harmonic oscillator, which can be used for controller and observer designs. In addition, it yields a method to estimate the coherent synchrotron frequency, i. e. the oscillation frequency of the rigid dipole mode. The model is on the one hand accurate enough to reflect the behavior of the bunch barycenter subject to rigid dipole

oscillations, and on the other hand simple enough for an easy controller design.

High intensity effects of particle bunches are outlined in Chap. 4, where space charge, wall impedance and resonator effects are discussed. All high intensity effects are however treated as external disturbances from a control engineering point of view and are not discussed exhaustively.

In Chap. 5 different controller designs for a beam phase feedback are presented after a short overview on previous developments. The currently used finite impulse response (FIR) filter for single-harmonic operation is discussed against the background of a dual-harmonic cavity system and compared to a matched filter design of variable filter length. Using the model derived in Chap. 3, an output feedback which can again be considered as an FIR filter is designed and its limitations and sensitivity against design parameters are outlined. These limitations are overcome by a state feedback in combination with an observer representing an infinite impulse response (IIR) filter. All controllers are verified in macro-particle simulations.

The damping of dipole oscillations with an FIR filter was tested in two beam experiments whose results are presented and compared to simulations in Chap. 6.

The model derived in Chap. 3, the controllers presented in Chap. 5 and the beam experiment in Chap. 6 are the main contributions of the dissertation at hand. For the beam experiment, the beam phase feedback in case of a dual-harmonic cavity system was implemented for the SIS18 and its effectiveness was demonstrated. The behavior of the beam phase feedback is now understood also in the dual-harmonic case in theory and in practice.

2 Longitudinal Single Particle Dynamics

This chapter reviews and summarizes fundamentals of longitudinal beam dynamics and the equations of motion in phase space. After a short introduction, an overview on synchrotron oscillation in Sec. 2.2 follows, including the definition of the *reference particle*, the description of the applied coordinate systems and an introduction to the dual-harmonic cavity system. In addition, the longitudinal equations of motion of single particles are derived and the phase-focusing principle is reviewed in detail. Important characteristics of a beam in the dual-harmonic cavity setting like the *bucket area* and the *synchrotron frequency* are discussed in Sec. 2.3. A complete acceleration cycle from injection to extraction of the particles is depicted in Sec. 2.4 before the chapter ends with a discussion in Sec. 2.5.

The chapter is mainly based on [61, 62] and partly on [98], which give a good overview on the subject.

2.1 Introduction

In a synchrotron, one or more cavities are used to provide radio frequency (RF) voltages. The RF field creates a potential well which accelerates the particles but also focuses the beam and creates so-called *particle bunches*. To make sure that the beam is constantly accelerated and focused, the radio frequency $f_{\mathrm{RF},0}(t)$ has to be synchronized with the reference revolution frequency $f_{\mathrm{R}}(t)$ of the particles,

$$f_{\mathrm{RF},0}(t) = h f_{\mathrm{R}}(t)\,. \tag{2.1}$$

The *harmonic number* $h \in \mathbb{N}$ denotes the maximum number of bunches which can be accelerated simultaneously [61, 62] and the index 0 indicates that the radio frequency can differ from its nominal value, resulting in the frequency

$$f_{\mathrm{RF}} = f_{\mathrm{RF},0} + \Delta f_{\mathrm{RF,z}}\,,$$

omitting the notation of the time-dependency. The disturbance $\Delta f_{\mathrm{RF,z}}$ can occur e. g. due to an incorrect setting or parameter deviations in the cavities.

Fig. 2.1 illustrates the particle line density $\lambda(z)$ of a bunched beam along the longitudinal axis z for $h = 2$ and a reference orbit length L_{R}.

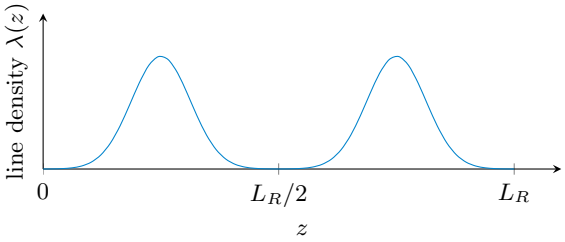

Figure 2.1: Particle line density along the longitudinal axis for $h = 2$

While longitudinal beam dynamics are mainly determined by the RF voltage, transverse dynamics are mainly affected by the magnetic lattice consisting of bending dipole magnets, focusing quadrupole magnets and, where required, of higher order magnets [62, 98].

Focusing in transverse as well as in longitudinal direction is necessary because of unavoidable deviations of the particles from reference states like position and velocity, which would otherwise lead to particle loss. In the presence of focusing, however, deviations lead to incoherent particle oscillations around a reference point [1].

Particle oscillations in transverse direction were first observed in betatrons which is why they are referred to as *betatron oscillations* [46, 61]. In longitudinal direction, particle oscillations are named *synchrotron oscillations* accordingly. Accelerator components are usually constructed in such a way that betatron and synchrotron motion are not or only little coupled. Furthermore, betatron oscillation has a much higher frequency than synchrotron oscillation [98]. For these reasons, particle dynamics in transverse direction will not be considered in this work, apart from the fact that energy deviations will lead to different path lengths and therefore different revolution times depending on the magnetic lattice, an effect which corresponds to an average over many betatron oscillations during one turn [61].

[1] Longitudinal focusing is always present if RF voltages with a certain amplitude are used, i. e. no additional components are needed beside the cavities.

2.2 Synchrotron Oscillation

In this section the longitudinal dynamics of single particles are described. Therefore, the so-called reference particle is introduced in Subsec. 2.2.1. Accounting for the ring shape of the synchrotron, a curvilinear coordinate system as well as the longitudinal phase space coordinates are introduced in Subsec. 2.2.2. The already mentioned dual-harmonic cavity mode is motivated and the resulting combined voltage is explained in Subsec. 2.2.3, based on which both the discrete and continuous longitudinal equations of motion are derived in Subsec. 2.2.4. Subsec. 2.2.5 introduces the principle of *Hamiltonian dynamics* as well as *Liouville's theorem* of area preservation which is an important characteristic of the discrete equations of motion. The Hamiltonian function will finally be used in Subsec. 2.2.6 to explain the phase stability principle.

2.2.1 The Reference Particle

All particles which are accelerated within one cycle are assumed to have the same rest mass m_0 and charge q [2], but to a certain extent different velocities $\boldsymbol{v}$. Due to the ring structure of the synchrotron with a small beam pipe radius, however, the particles still have to travel close to a reference orbit making it necessary to focus the beam. An ideal (but usually non-existing) particle which follows the reference orbit exactly is referred to as the *synchronous* or *reference* particle as illustrated in Fig. 2.2. This implies that the reference particle also always has the reference energy and revolution period, to which the frequency and amplitude of the cavities as well as the magnetic fields are synchronized. Throughout this dissertation all values referring to the reference particle will be labeled with the subscript R.

2.2.2 The Curvilinear Coordinate System and Longitudinal Phase Coordinates

To fully describe a particle in the beam pipe, six coordinates are needed, namely the three space coordinates x, y and z together with the three momenta p_x, p_y and p_z. While the horizontal axis x and the vertical axis y are perpendicular to the beam reference orbit, the longitudinal axis z is curved along the reference orbit according to Fig. 2.3.

[2] In principle the particles only need to have the same ratio $\frac{m_0}{q}$, see Subsec. 2.2.4

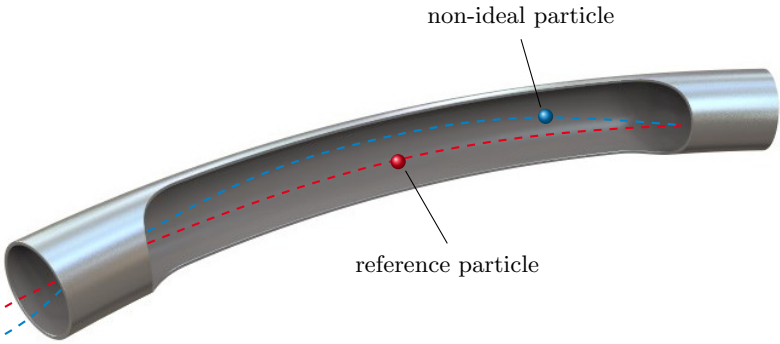

Figure 2.2: Illustration of the reference particle

The synchrotron SIS18 at GSI is presently equipped with two equally constructed cavities [3] located at opposite sites of the ring having the reference orbit length L_R. The zero point of the coordinate system is placed in the middle of the first cavity ($z = 0$) whereby the second cavity is located at $z = \frac{L_\mathrm{R}}{2}$. The longitudinal axis z points in the direction of the reference beam velocity.

As all components of the accelerator are synchronized with the reference particle, however, it is usually sufficient to describe the particles not with absolute values but with respect to the reference R. In this case relative coordinates Δx, Δy and Δz are used which are defined as

$$\Delta\xi = \xi - \xi_\mathrm{R} \ ,$$

where ξ is an arbitrary variable. The origin of the relative coordinate system is located at

$$\begin{bmatrix} x_{\mathrm{rel},0} \\ y_{\mathrm{rel},0} \\ z_{\mathrm{rel},0} \end{bmatrix} = \begin{bmatrix} 0 \\ 0 \\ z_\mathrm{R}(t) \end{bmatrix}$$

on the reference orbit.

As already motivated in the introduction, longitudinal and transverse motion can be considered to be decoupled which is why in the following

[3] Additional cavities are currently added but were not yet in operation during the beam experiments presented in Chap. 6. In this dissertation the present state of the synchrotron in July 2014 is considered.

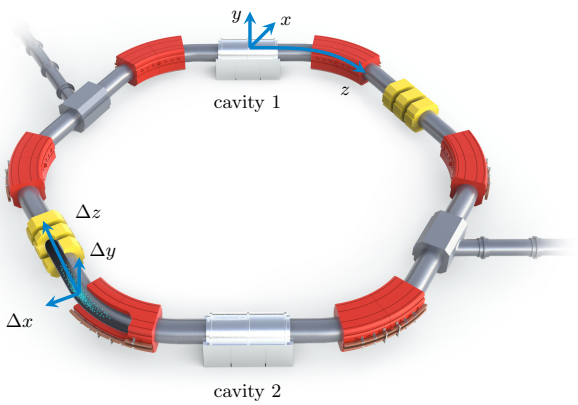

Figure 2.3: Illustration of the curvilinear coordinate system with zero point in the middle of the first cavity

only longitudinal coordinates will be studied in more detail. Any coupling effects that still occur are treated as disturbances.

First of all it can be more convenient to consider the phase $\phi(t)$ of a particle with respect to the accelerating voltage

$$V(t) = \hat{V}(t) \sin\left(\phi(t) - \Delta\phi_{\mathrm{u}}(t)\right)$$

instead of the location z, as for longitudinal beam dynamics mainly the voltage present in the cavity during crossing of the particle is important, and not the absolute location of the particle in the ring [61, 62, 98]. The phase $\phi(t)$ can be expressed as

$$\begin{aligned}\phi(t) &= 2\pi \int_{t_0}^{t} \left[f_{\mathrm{RF,0}}\left(\tilde{t}\right) + \Delta f_{\mathrm{RF,z}}\left(\tilde{t}\right)\right] \mathrm{d}\tilde{t} + \phi(t_0) \\ &= \phi_0(t) + \Delta\phi_{\mathrm{z}}(t) + \phi(t_0)\,. \end{aligned} \tag{2.2}$$

The voltage amplitude is changed during the acceleration cycle (cf. Sec. 2.3) and is therefore a function of time t. The phase shift $\Delta\phi_{\mathrm{u}}$ is introduced by a possible phase feedback. Although a disturbance $\Delta f_{\mathrm{RF,z}}$ may change the phase $\phi(t)$, this will be omitted further on, and $\phi(t) = \phi_0(t) + \phi(t_0)$ is understood to represent the nominal phase.

Crossing the cavity with a gap length L_{gap} across which the voltage is applied takes particle i the time T_{cross}. The particle is assumed to enter the cavity gap at time $t_i - T_{\mathrm{cross}}/2$ and leave the gap at time $t_i + T_{\mathrm{cross}}/2$. The cavities in the SIS18 have a gap length of $L_{\mathrm{gap}} = 0.15\,\mathrm{m} \ll L_{\mathrm{R}} = 216.72\,\mathrm{m}$ [30] in which the RF voltage is applied. Therefore also the crossing time T_{cross} is much smaller than the revolution time T_R and the approximation $T_{\mathrm{cross}} \to 0$ is justified [61, 62]. It can therefore also be assumed that ω_{RF} and $\hat{V}(t) = \hat{V}$ are constant during crossing, and the voltage seen by the particle is

$$\begin{aligned} V_i &= \frac{1}{T_{\mathrm{cross}}} \int_{t_i - T_{\mathrm{cross}}/2}^{t_i + T_{\mathrm{cross}}/2} \hat{V} \sin(\omega_{\mathrm{RF}} t + \phi(t_0) - \Delta\phi_{\mathrm{u}}(t))\,\mathrm{d}t \\ &\approx \hat{V} \sin(\omega_{\mathrm{RF}} t_i + \phi(t_0) - \Delta\phi_{\mathrm{u}}(t)) = V(t_i) \end{aligned}$$

for $\Delta f_{\mathrm{RF,z}} = 0$. Now t_i denotes the arrival time instant of the particle at the cavity, which the particle leaves immediately for its next turn.

All variables can be considered in the continuous and the discrete time domain. In the latter case the variables are sampled at time instant $t_i(k)$, i. e. at the arrival time of the particle under consideration in turn k at the cavity. If more than one cavity is present, their voltages add up as will be explained later, and $t_i(k)$ refers to the arrival time at a virtual cavity which is assumed to supply the combined voltage. In Eq. (2.2) the absolute RF phase at time t depending on its initial value $\phi(t_0)$ is given, but for the acceleration of a particle only a relative phase with respect to the zero crossing of the voltage is important. For a given harmonic number h, as many bunches can be placed in the synchrotron, and in each turn k there are h zero crossings of the positive as well as of the negative slope of $V(t)$, as illustrated in Fig. 2.4 for $h = 2$.

Defining $\phi_m^+(k) = \phi\left(t_m^+(k)\right)$ as the absolute phase at time $t_m^+(k)$ denoting the time instant of the zero crossing of the positive slope in turn k of bunch $m \in \{1, \ldots, h\}$, the relative phase of particle i crossing the cavity in the time instant t_i is

$$\varphi(t_i(k)) = \phi(t_i(k)) - \phi\left(t_m^+(k)\right)\ ,$$

as shown in Fig. 2.5.

The relative phase $\varphi(t_i(k))$ thus refers to the zero crossing of the positive slope if no feedback system is present. The feedback can be accounted for by the phase shift

$$\Delta\phi_{\mathrm{u}}(t_i(k)) \approx \Delta\phi_{\mathrm{u}}(k)$$

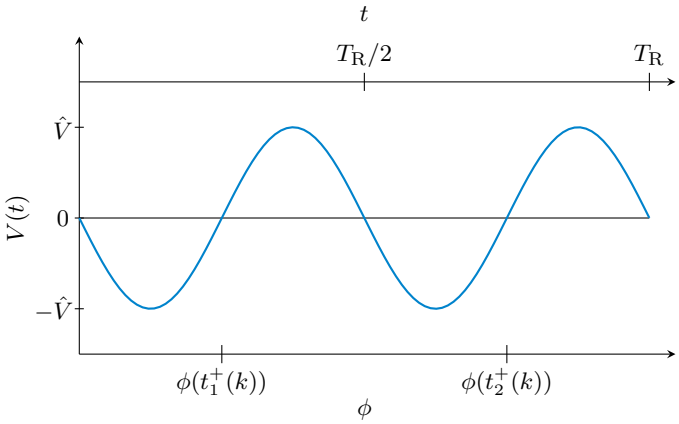

Figure 2.4: Illustration of $V(t)$ for $h = 2$

assuming that the phase shift introduced by the feedback system barely changes between the crossing of individual particles and therefore $\Delta\phi_u(k)$ is identical for all particles i. The voltage $V(t_i(k))$ now reads

$$V(t_i(k)) = \hat{V}_1 \sin(\varphi(t_i(k)) - \Delta\varphi_u(k)) ,$$

where also the phase shift $\Delta\varphi_u(k)$ due to a feedback systems was expressed relative to the voltage zero crossing of the unshifted voltage.

To improve readability, further on the notation $\xi_i(k)$ will be used instead of $\xi(t_i(k))$ for an arbitrary variable ξ.

In [62] also a relative arrival time τ is introduced, where

$$\varphi_i(k) = \omega_{RF}(k)\tau_i(k) . \tag{2.3}$$

Eq. (2.3) holds if the RF frequency changes *adiabatically*, i. e. if changes are small compared to absolute values. This is true if [61]

$$\alpha_{ad} = \left| \frac{1}{\omega_{syn}^2} \frac{d\omega_{syn}}{dt} \right| \ll 1$$

where ω_{syn} is the angular *synchrotron frequency* explained in detail in Sec. 2.3. Adiabatic changes are assumed throughout this dissertation. In this case ω_{RF} can be considered constant during one turn.

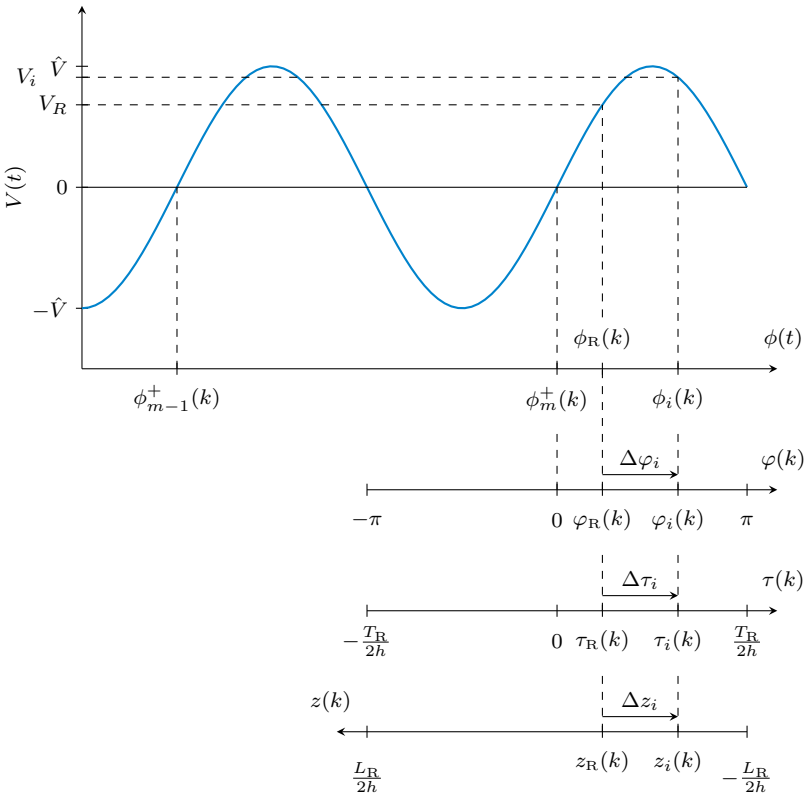

Figure 2.5: Absolute (ϕ_i) and relative phase ($\Delta\varphi_i$) of particle i within bunch m in turn k, together with its relative arrival time ($\Delta\tau_i$) and relative location (Δz_i)

Both the phase φ and the arrival time τ can again be referred to the reference particle,

$$\Delta\varphi = \varphi - \varphi_\mathrm{R} \,,$$
$$\Delta\tau = \tau - \tau_\mathrm{R} \,.$$

Note that the relative phase $\Delta\varphi$ and arrival time $\Delta\tau$ are positive for particles traveling behind the reference particle, whereas the relative location Δz is negative.

Besides the absolute phase $\phi_i(k)$ and the relative phase $\varphi_i(k)$, Fig. 2.5 also illustrates the relative arrival time $\tau_i(k)$ and the relative location $\Delta z_i(k)$ of a particle i within bunch m in turn k.

2.2.3 Introduction to Dual-Harmonic Cavity System

Currently the SIS18 is operated in single-harmonic mode which means that both cavities run with the same frequency f_RF providing the same voltage $V_{1,2}(t) = \hat{V}(t)\sin(\phi_{1,2}(t))$. Taking into account the position of the cavities by an appropriate phase shift $\phi_{1,2}(t_0)$, each particle i experiences the same voltage

$$V_i(k) = \hat{V}\sin(\varphi_i(k) - \Delta\varphi_\mathrm{u}(k))$$

twice per turn.

After construction of the FAIR, however, operation will be switched to the so-called dual-harmonic mode in which the second cavity [4] runs with twice the fundamental frequency [77]

$$f_\mathrm{RF,2} = 2f_\mathrm{RF,0} + \Delta f_\mathrm{RF,z,2} \,.$$

If a beam phase feedback is active, twice the actuating phase shift of the first cavity has to be applied to the second one. In the beam pipe electric fields $\boldsymbol{\mathcal{E}}$ provided by the cavities and magnetic fields $\boldsymbol{B}$ created by the magnets are present, in which the particles with charge q and velocity $\boldsymbol{v}$ experience the Lorentz force

$$\boldsymbol{F}_\mathrm{L} = q\boldsymbol{\mathcal{E}} + q(\boldsymbol{v}\times\boldsymbol{B}) \,,$$

which is also valid for relativistic particles [61]. The kinetic energy of a particle crossing a cavity is changed by the amount

$$\Delta E_\mathrm{kin} = \int \boldsymbol{F}_\mathrm{L}\,\mathrm{d}z = \int q\boldsymbol{\mathcal{E}}\,\mathrm{d}z + \int q(\boldsymbol{v}\times\boldsymbol{B})\boldsymbol{v}\,\mathrm{d}t = qV$$

[4] If wide-band cavities are used, dual-harmonic operation can also be obtained with a single cavity [92].

linear in V. If the particle crosses two cavities, their voltages add up to the combined voltage

$$V(\varphi_i) = \hat{V}_1 \sin(\varphi_i - \Delta\varphi_\mathrm{u}) + \hat{V}_2 \sin(2\varphi_i - 2\Delta\varphi_\mathrm{u} + \psi) \,,$$

where ψ is an adjustable phase shift between the cavity voltages. Doubling $\Delta\varphi_\mathrm{u}$ when applied to the second cavity guarantees that the shape of the combined voltage is not changed. The following derivations are carried out for $\Delta\varphi_\mathrm{u} = 0$, but also hold otherwise.

The amplitude $\hat{V}_2$ of the second voltage and the phase ψ represent additional degrees of freedom which are used to lengthen the bunch by creating a saddle point in the voltage at the reference phase φ_R. Thereby beam current peaks are reduced and higher beam currents can be handled [12, 77]. A saddle point at φ_R requires that

$$V(\varphi_\mathrm{R}) = \hat{V}_1 \sin(\varphi_\mathrm{R}) + \hat{V}_2 \sin(2\varphi_\mathrm{R} + \psi) = V_\mathrm{R} \,, \tag{2.4a}$$

$$\left.\frac{\mathrm{d}V(\varphi)}{\mathrm{d}\varphi}\right|_{\varphi=\varphi_\mathrm{R}} = \hat{V}_1 \cos(\varphi_\mathrm{R}) + 2\hat{V}_2 \cos(2\varphi_\mathrm{R} + \psi) = 0 \,, \tag{2.4b}$$

$$\left.\frac{\mathrm{d}^2V(\varphi)}{\mathrm{d}\varphi^2}\right|_{\varphi=\varphi_\mathrm{R}} = -\hat{V}_1 \sin(\varphi_\mathrm{R}) - 4\hat{V}_2 \sin(2\varphi_\mathrm{R} + \psi) = 0 \,. \tag{2.4c}$$

Eq. (2.4) hold for [49]

$$\hat{V}_2 = -\frac{\hat{V}_1 \cos(\varphi_\mathrm{R})}{2\cos(2\varphi_\mathrm{R} + \psi)} \,, \tag{2.5a}$$

$$\varphi_\mathrm{R} = \arcsin\left(\frac{4}{3}\frac{V_\mathrm{R}}{\hat{V}_1}\right) \,, \tag{2.5b}$$

$$\psi = \arctan\left(\frac{1}{2}\tan(\varphi_\mathrm{R})\right) - 2\varphi_\mathrm{R} \,. \tag{2.5c}$$

For $\varphi_\mathrm{R} < \frac{\pi}{2}$ the saddle point is located in the positive slope of the combined voltage, while for $\varphi_\mathrm{R} > \frac{\pi}{2}$ the saddle point is in the negative slope. Both options are possible and depend on the energy of the beam which will be discussed in Subsec. 2.2.4. Fig. 2.6 illustrates the combined voltage for $V_\mathrm{R} = 0.3 \cdot \hat{V}_1$ and $\varphi_\mathrm{R} < \frac{\pi}{2}$.

In the following, the dual-harmonic cavity mode is considered as the standard setting for which the longitudinal equations of motion are derived.

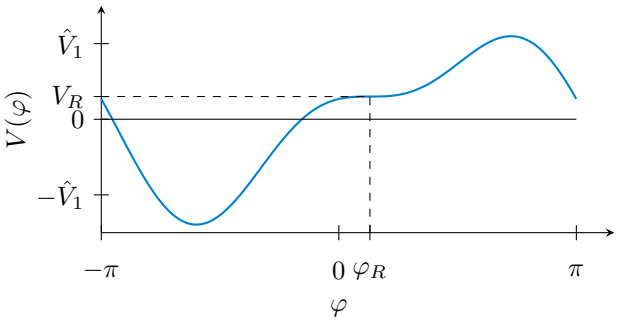

Figure 2.6: Illustration of the combined dual-harmonic voltage for $V_\mathrm{R} = 0.3 \cdot \hat{V}_1$

2.2.4 Longitudinal Equations of Motion

As the particles in the beam in general have phases $\varphi_i(k) \neq \varphi_\mathrm{R}(k)$, they are accelerated or decelerated by a voltage $V(\varphi_i(k)) \neq V_\mathrm{R}(k)$ leading to a change of their kinetic energy of

$$\Delta E_{\mathrm{kin},i}(k) = qV_i(k) \neq qV_\mathrm{R}(k)\,,$$

where

$$V(\varphi_i(k)) = \hat{V}_1(k)\sin(\varphi_i(k)) + \hat{V}_2(k)\sin(2\varphi_i(k) + \psi(k))\,,$$

and the total energy of the particle in turn $k+1$ is

$$E_i(k+1) = E_i(k) + \Delta E_{\mathrm{kin},i}(k)\,.$$

The total energy

$$E_i = \gamma_i m_0 c^2$$

of a particle consists of the rest energy

$$E_0 = m_0 c^2$$

and the kinetic energy

$$E_{\mathrm{kin},i} = (\gamma_i - 1) m_0 c^2$$

where

$$\gamma = \sqrt{\frac{1}{1 - \frac{v^2}{c^2}}}$$

is the so-called *Lorentz factor*, $v = |\boldsymbol{v}|$ is the velocity and c the speed of light in vacuum.

As the rest energy is constant and equals the rest energy of the reference particle, it is again convenient not to regard total energies but only deviations

$$\Delta E_i = E_i - E_\mathrm{R} = E_{\mathrm{kin},i} - E_{\mathrm{kin,R}}$$

from the reference. The energy deviation in turn $k+1$ is therefore

$$\begin{aligned}\Delta E_i(k+1) &= \Delta E_i(k) + \Delta E_{\mathrm{kin},i}(k) - \Delta E_{\mathrm{kin,R}}(k) \\ &= \Delta E_i(k) + q\left(V(\varphi_i(k)) - V_\mathrm{R}(k)\right) \,. \end{aligned} \tag{2.6}$$

An energy deviation $\Delta E_i(k+1) \neq 0$ results in a revolution period of $T_i(k+1) \neq T_\mathrm{R}(k+1)$. Neglecting energy losses due to synchrotron radiation or collisions with residual gas particles in the non-ideal vacuum, the revolution period $T_i(k)$ remains constant during the whole turn k and for an adiabatic process, also ω_RF does not change significantly. Therefore the relative phase at the end of turn $k+1$ is

$$\begin{aligned}\Delta\varphi_i(k+1) &= \Delta\varphi_i(k) + \omega_\mathrm{RF}(k+1)(T_i(k+1) - T_\mathrm{R}(k+1)) \\ &= \Delta\varphi_i(k) + \omega_\mathrm{RF}(k+1)\Delta T_i(k+1) \,. \end{aligned} \tag{2.7}$$

From Eq. (2.6) the change of energy is known, which has now to be set in relation to a change of the period ΔT. The revolution period T_i, being close to the reference period T_R for particles within the bunch, can be expressed in terms of reference values as

$$T_i = \frac{L_i}{v_i} = \frac{L_\mathrm{R}}{v_\mathrm{R}} + \frac{1}{v_\mathrm{R}}\Delta L_i - \frac{L_\mathrm{R}}{v_\mathrm{R}^2}\Delta v_i + \mathcal{T}\left(\Delta L_i^{(n>1)}, \Delta v_i^{(n>1)}\right) \,,$$

where $\mathcal{T}\left(\Delta L_i^{(n>1)}, \Delta v_i^{(n>1)}\right)$ denotes higher order terms of the Taylor series. In a linear approximation

$$\Delta T_i = T_i - T_\mathrm{R} \approx \frac{1}{v_\mathrm{R}}\Delta L_i - \frac{L_\mathrm{R}}{v_\mathrm{R}^2}\Delta v_i$$

follows.

Setting ΔT_i in relation to T_R yields

$$\frac{\Delta T_i}{T_\mathrm{R}} \approx \frac{\Delta L_i}{L_\mathrm{R}} - \frac{\Delta v_i}{v_\mathrm{R}} \,. \tag{2.8}$$

According to Eq. (A.1) in the appendix

$$\frac{\Delta v_i}{v_\mathrm{R}} \approx \frac{1}{\beta_\mathrm{R}^2 \gamma_\mathrm{R}^2} \frac{\Delta E_i}{E_\mathrm{R}} \,, \tag{2.9}$$

which sets the velocity deviation in relation to the energy deviation. The relation between the energy of a particle and the length of the corresponding orbit depends on the *lattice* of the accelerator under consideration, i. e. on the magnetic setting consisting of the dipole, the quadrupole and higher order magnets [61, 62, 98]. In the literature usually

$$\frac{L_i}{L_\mathrm{R}} = 1 + \alpha_0 \delta_i + \alpha_1 \delta_i^2 + \alpha_2 \delta_i^3 + \cdots = 1 + \frac{\Delta L_i}{L_\mathrm{R}} \tag{2.10}$$

can be found where

$$\delta_i = \frac{\Delta p_i}{p_\mathrm{R}} = \frac{p_i - p_\mathrm{R}}{p_\mathrm{R}} \approx \frac{1}{\beta_\mathrm{R}^2} \frac{\Delta E_i}{E_\mathrm{R}} \tag{2.11}$$

is the fractional momentum using the approximation for small deviations given in (A.1). The parameters α_ν, $\nu \in \mathbb{N}_0$ depend on the magnetic lattice.

Inserting (2.9) and (2.10) into (2.8) using (2.11) yields

$$\begin{aligned} \frac{\Delta T_i}{T_\mathrm{R}} \approx \alpha_0 \frac{1}{\beta_\mathrm{R}^2} \frac{\Delta E_i}{E_\mathrm{R}} + \alpha_1 \left(\frac{1}{\beta_\mathrm{R}^2} \frac{\Delta E_i}{E_\mathrm{R}} \right)^2 + \alpha_2 \left(\frac{1}{\beta_\mathrm{R}^2} \frac{\Delta E_i}{E_\mathrm{R}} \right)^3 \\ - \frac{1}{\beta_\mathrm{R}^2 \gamma_\mathrm{R}^2} \frac{\Delta E_i}{E_\mathrm{R}} \,. \end{aligned}$$

Neglecting again higher order terms finally results in

$$\frac{\Delta T_i}{T_\mathrm{R}} \approx \left(\alpha_0 - \frac{1}{\gamma_\mathrm{R}^2} \right) \frac{1}{\beta_\mathrm{R}^2} \frac{\Delta E_i}{E_\mathrm{R}} = \eta_\mathrm{R} \frac{1}{\beta_\mathrm{R}^2} \frac{\Delta E_i}{E_\mathrm{R}} \,, \tag{2.12}$$

and inserting (2.12) into (2.7) using (2.1) yields

$$\Delta \varphi_i(k+1) = \Delta \varphi_i(k) + \left. \frac{\omega_\mathrm{RF} \eta_\mathrm{R} T_\mathrm{R}}{\beta_\mathrm{R}^2 E_\mathrm{R}} \right|_{(k+1)} \Delta E_i(k+1) \,,$$

which for nominal $\omega_\mathrm{RF} = \omega_{\mathrm{RF},0} = h\omega_\mathrm{R}$ reads

$$\Delta \varphi_i(k+1) = \Delta \varphi_i(k) + \left. \frac{2\pi h \eta_\mathrm{R}}{\beta_\mathrm{R}^2 E_\mathrm{R}} \right|_{(k+1)} \Delta E_i(k+1) \,. \tag{2.13}$$

The parameter α_0 is called the *momentum compaction factor* and can also be expressed in terms of the so-called *transition energy* γ_t which is defined as

$$\alpha_0 = \frac{1}{\gamma_\mathrm{t}^2} \,.$$

The *phase slip factor*

$$\eta_\mathrm{R} = \frac{1}{\gamma_\mathrm{t}^2} - \frac{1}{\gamma_\mathrm{R}^2}$$

compares the normalized reference energy γ_R to the transition energy. Eq. (2.6) and (2.13) form the discrete longitudinal equations of motion of a single particle and span the longitudinal phase space. They are also referred to as the mapping or tracking equations of a particle, because they track the trajectory of the particle in phase space, and can also be expressed in different coordinates, which will be elucidated in Subsec. 2.2.5.

Remark 1. *Eq.* (2.13) *describes the change of the relative phase* $\Delta\varphi_i = \varphi_i - \varphi_R$*. Of course also* φ_R *changes during the acceleration cycle (see Sec. 2.4). It can however be regarded as constant during one turn if changes are adiabatic. In this case* (2.13) *still holds and* $\varphi_i(k+1) = \varphi_R(k+1) + \Delta\varphi_i(k+1)$*.*

For beam energies below transition energy, i. e. for $\gamma_\mathrm{R} < \gamma_\mathrm{t}$ the phase slip factor η_R is negative, which means that a positive energy deviation ΔE_i leads to a decrease of the relative phase $\Delta\varphi_i$ (and vice versa). Particles which arrive at the cavities later than the reference particle (i. e. with a phase $\varphi_i > \varphi_\mathrm{R}$) thus have to be accelerated relative to the reference particle by crossing a voltage $V_i > V_\mathrm{R}$. Particles which arrive earlier than the reference particle, on the other hand, have to cross a voltage $V_i < V_\mathrm{R}$ in order to decrease their relative energy.

Above transition energy however, η_R is positive, and a positive energy deviation $\Delta E_i > 0$ results in an increase of the phase and of the arrival time, respectively.

Increasing the energy of a particle has two effects:

1. The velocity v of the particle is increased.

2. The relativistic mass $m = \gamma m_0$ of the particle is increased.

If the kinetic energy of the particle is small, the Lorentz factor γ is small and the first effect predominates, which is the case below transition energy. The particle is faster and completes the orbit L in a shorter time. For

highly relativistic particles above transition energy with a velocity closer to the speed of light, however, the second effect predominates. In this case, the particle mainly gets heavier and the centripetal force in the dipole magnets with bending radius ρ,

$$F_\mathrm{c} = \frac{\gamma m_0 v^2}{\rho}$$

outbalances the Lorentz force

$$F_\mathrm{L} = qvB$$

leading to an increased orbit L for which the particle needs more time to complete as $v \approx \text{const}$.

These effects can also be seen in Eq. (2.8) where enlarging the orbit length and increasing the velocity both affect the revolution period T_i. If the particle has exactly transition energy, both effects cancel each other out (in a linear approximation) and small changes to the particle energy do not change its phase at the cavity.

Particles above transition therefore have to cross a negative energy if they arrive at the cavities later than the reference in order to decrease their mass, while early particles have to gain energy. This is accomplished by changing the phase of the accelerating voltages, and for a stable beam the *stability condition* (see also Subsec. 2.2.6)

$$-\eta_\mathrm{R} \cos(\varphi_R) > 0\,, \tag{2.14}$$

discovered by E. M. McMillan [73] and V. I. Veksler [96], must be fulfilled. The resulting voltages below and above transition in the stationary case, i. e. in the absence of beam acceleration, are shown in Fig. 2.7.

At transition energy, $\eta_\mathrm{R} = 0$ and no phase focusing is present. If needed, crossing of transition energy is therefore usually done as fast as possible. In this dissertation only energies below transition are considered. The results, however, are in principle also transferable to energies above transition.

Remark 2. *Equating F_c and F_L, after some transformations, yields $B\rho = \frac{\gamma m_0 v}{q} = \frac{p}{q}$, where $B\rho$ is the magnetic rigidity, which is the same for all particles having the same velocity and mass-to-charge ratio $\frac{m_0}{q}$. This means that in principle different particles can be accelerated simultaneously as long as they have the same mass to charge ratio.*

Remark 3. *Close to the transition energy, η strongly depends on δ and reads $\eta(\delta) = \eta_0 + \eta_1\delta + \eta_2\delta^2 + \dots$. The non-constant terms have been neglected here due to linear approximations done during the derivation of* (2.12) [61].

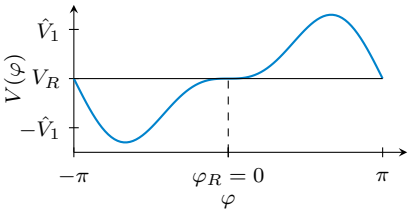

(a) Below transition energy: $\hat{V}_2 = 0.5 \cdot \hat{V}_1$, $\psi = \pi$

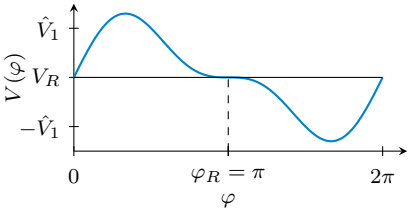

(b) Above transition energy: $\hat{V}_2 = 0.5 \cdot \hat{V}_1$, $\psi = 0$

Figure 2.7: Required voltage below and above transition energy for $V_\mathrm{R} = 0$ for a stable operation

The discrete mapping equations (2.6) and (2.13) can be transferred to the continuous time domain by simply forming the forward difference quotient

$$\frac{\Delta\xi_i(k+1) - \Delta\xi_i(k)}{T_\mathrm{R}} \approx \Delta\dot{\xi}_i(t)\,. \tag{2.15}$$

This approximation is valid because the particle dynamics are much slower than the revolution in the synchrotron, which will be discussed in detail in Sec. 2.3.2. The continuous equations of motion read

$$\Delta\dot{E}_i(t) = \frac{q}{T_\mathrm{R}}\left(V(\varphi_i(t)) - V_\mathrm{R}\right) , \tag{2.16a}$$

$$\Delta\dot{\varphi}_i(t) = \frac{\omega_\mathrm{RF}\eta_\mathrm{R}}{\beta_\mathrm{R}^2 E_\mathrm{R}}\Delta E_i(t) . \tag{2.16b}$$

Eq. (2.16a) is to be discussed further. It is assumed that the phase of the particle relative to the voltage zero crossing is continuous which means that a voltage is applied continuously along the whole ring. The continuous voltage leads to the same energy change as the assumed voltage kick in the discrete domain, resulting in the already mentioned assumption $T_\mathrm{cross} \to 0$.

2.2.5 Hamiltonian Function of Longitudinal Motion

An elegant way to describe the trajectories of the particles in phase space is the use of the *Hamiltonian function*. It has the benefit that the contour lines of the Hamiltonian function equal the trajectories in phase space of the single particles. A general overview on Hamiltonian dynamics can for example be found in [11, 33, 44, 81]. For their applications to synchrotron motion refer to e. g. [61, 62, 98].

For one-dimensional [5] canonical conjugate variables Q and P the Hamiltonian function is defined as

$$\mathcal{H}(Q,P) = P\dot{Q} - \mathcal{L} ,$$

where P is called the *generalized momentum* to the *generalized coordinate* Q, and $\mathcal{L}$ is the *Lagrange function*. Considering a particle in a potential field $\Phi(Q,t)$ depending on the location Q and possibly on time t, the Lagrange function is

$$\mathcal{L} = E_\mathrm{kin} - \Phi(Q,t) .$$

The generalized coordinates P and Q are also called *canonical conjugate* variables. Differentiating the Hamiltonian function $\mathcal{H}(Q,P)$ with respect to Q and P gives the equations of motion,

$$\dot{Q} = \frac{\partial\mathcal{H}}{\partial P} , \quad \dot{P} = -\frac{\partial\mathcal{H}}{\partial Q} .$$

[5] The Hamiltonian can also be formulated for multi-dimensional variables $\boldsymbol{Q}$ and $\boldsymbol{P}$, but as only the longitudinal motion is regarded here, the treatment of one-dimensional variables is sufficient in the present context.

Hamiltonian systems have the important property that they preserve area in phase space, known as *Liouville's theorem* [81]. This means that any element defined by the area between nearby points moving in phase space has a constant value, although its shape may change with time. Expressing the equations of motion in the discrete time-domain with the sampling period T_R,

$$P(k+1) = P(k) - T_\mathrm{R}\frac{\partial \mathcal{H}(Q(k),P(k),t(k))}{\partial Q(k)}\,, \tag{2.17a}$$

$$Q(k+1) = Q(k) + T_\mathrm{R}\frac{\partial \mathcal{H}(Q(k),P(k+1),t(k+1))}{\partial P(k+1)}\,, \tag{2.17b}$$

the flow is area-preserving as shown e. g. in [49, 62, 81], if the determinant of the Jacobian of the transformation $[Q(k), P(k)] \to [Q(k+1), P(k+1)]$,

$$\det J = \left|\frac{\partial[Q(k+1), P(k+1)]}{\partial[Q(k), P(k)]}\right| = \begin{vmatrix} \frac{\partial P(k+1)}{\partial P(k)} & \frac{\partial P(k+1)}{\partial Q(k)} \\ \frac{\partial Q(k+1)}{\partial P(k)} & \frac{\partial Q(k+1)}{\partial Q(k)} \end{vmatrix} = 1\,.$$

Note that in (2.17b) the value of P for the sample $k+1$ is used instead of the value $P(k)$, as it was already done in (2.13). This is necessary for area-preservation [50, 62].

It is interesting to note that area preservation also holds for non-conjugate pairs of variables if the beam is stationary. If however an acceleration is simulated, care has to be taken that only canonical conjugate variables are used, which can e. g. be obtained from another pair of canonical conjugate variables by the transformation

$$\tilde{Q} = g(t)Q\,, \quad \tilde{P} = \frac{1}{g(t)}P$$

with a (possibly) slowly time-varying factor $g(t)$ [62]. Using other transformations may lead to reduction or increasing of the bunch size in phase space during acceleration of the beam. There are however exceptions like the pair ($\Delta\varphi$, $\Delta E/\omega_\mathrm{R}$) which is obtained from the canonical conjugate pair ($\Delta\tau$, ΔE) by the transformation

$$\Delta\varphi = h\omega_\mathrm{R}\Delta\tau\,, \quad \Delta E/\omega_\mathrm{R} = \frac{\Delta E}{\omega_\mathrm{R}}\,.$$

As the harmonic number h is constant, area is also preserved during acceleration.

Tab. 2.1 gives an overview on some combinations of longitudinal coordinates and which pairs are canonical conjugate or preserve area in phase space also during acceleration. Transformations are given with respect to the pair $(\Delta\tau, \Delta E)$.

Table 2.1: Overview on some combinations of longitudinal coordinates

coordinates	can. conj.?	area preserv.?	unit of phase space area
$(\Delta z = -\beta_\mathrm{R} c \Delta\tau,$ $\Delta p = \frac{1}{\beta_\mathrm{R} c}\Delta E)$	yes	yes	Js
$(\Delta\tau, \Delta E)$	yes	yes	Js
$(\Delta\varphi = \omega_\mathrm{RF}\Delta\tau, \Delta E)$	no	no	rad · J
$(\Delta\varphi, \frac{\Delta E}{\omega_\mathrm{R}})$	no	yes	rad · Js
$(\Delta\varphi, \Delta W = \frac{\Delta E}{\omega_\mathrm{RF}})$	yes	yes	rad · Js
$(\Delta\varphi, \delta = \frac{\Delta p}{p_\mathrm{R}} \approx \frac{1}{\beta_\mathrm{R}^2}\frac{\Delta E}{E_\mathrm{R}})$	no	no	rad

Below, the longitudinal coordinates $(\Delta\varphi, \Delta W = \frac{\Delta E}{\omega_\mathrm{RF}})$ will be used for the following reasons:

- the pair is area preservative.
- regardless of the radio frequency f_RF, the phase interval (in rad) of a stable bunch remains constant.

The continuous equations of motion and the associated Hamiltonian of selected coordinate pairs from Tab. 2.1 are listed in Tab. 2.2. They are only valid if changes are adiabatic, i. e. if the parameters can be assumed to be constant during one turn, and for small deviations of reference values such that Eq. (A.1) holds. For simulations, the equations of motion are discretized analogously to (2.15) and evaluated for each turn in the synchrotron with constant parameters. If the beam is accelerated, the parameters have to be adjusted in each simulation loop, i. e. for each turn. The potential $\tilde{V}(\vartheta, \xi_\mathrm{R}, \Delta\xi)$ given in Tab. 2.2 reads

$$\tilde{V}(\vartheta,\xi_\mathrm{R}, \Delta\xi) = \hat{V}_1 \left[\frac{1}{\vartheta}\cos\left(\vartheta \cdot (\xi_\mathrm{R} + \Delta\xi)\right) - \frac{1}{\vartheta}\cos\left(\vartheta \cdot \xi_\mathrm{R}\right) + \Delta\xi \sin\left(\vartheta \cdot \xi_\mathrm{R}\right)\right]$$

$$+\hat{V}_2\left[\frac{1}{2\vartheta}\cos\left(2\vartheta\cdot(\xi_\mathrm{R}+\Delta\xi)+\psi\right)-\frac{1}{2\vartheta}\cos\left(2\vartheta\cdot\xi_\mathrm{R}+\psi\right)\right.$$
$$\left.+\Delta\xi\sin\left(2\vartheta\cdot\xi_\mathrm{R}+\psi\right)\right]. \tag{2.18}$$

Table 2.2: Overview on equations of motion and associated Hamiltonian functions for different coordinates with $\tilde{V}(\vartheta,\xi_\mathrm{R},\Delta\xi)$ according to (2.18)

$\underline{(\Delta z,\Delta p)}$: $\Delta\dot{z}=-\frac{\beta_\mathrm{R}c\eta_\mathrm{R}}{p_\mathrm{R}}\Delta p\,,\quad \Delta\dot{p}=\frac{q}{T_\mathrm{R}\beta_\mathrm{R}c}\left[\hat{V}_1\sin\left(-\frac{\omega_\mathrm{RF}}{\beta_\mathrm{R}c}(z_\mathrm{R}+\Delta z)\right)\right.$ $\left.+\hat{V}_2\sin\left(-2\frac{\omega_\mathrm{RF}}{\beta_\mathrm{R}c}(z_\mathrm{R}+\Delta z)+\psi\right)-V_\mathrm{R}\right]$ $\mathcal{H}(\Delta z,\Delta p)=-\frac{\beta_\mathrm{R}c\eta_\mathrm{R}}{2p_\mathrm{R}}\Delta p^2+\frac{q}{T_\mathrm{R}\beta_\mathrm{R}c}\tilde{V}\left(-\frac{\omega_\mathrm{RF}}{\beta_\mathrm{R}c},z_\mathrm{R},\Delta z\right)$
$\underline{(\Delta\tau,\Delta E)}$: $\Delta\dot{\tau}=\frac{\eta_\mathrm{R}}{\beta_\mathrm{R}^2E_\mathrm{R}}\Delta E\qquad \Delta\dot{E}=\frac{q}{T_\mathrm{R}}\left[\hat{V}_1\sin\left(\omega_\mathrm{RF}(\tau_\mathrm{R}+\Delta\tau)\right)\right.$ $\left.+\hat{V}_2\sin\left(2\omega_\mathrm{RF}(\tau_\mathrm{R}+\Delta\tau)+\psi\right)-V_\mathrm{R}\right]$ $\mathcal{H}(\Delta\tau,\Delta E)=\frac{\eta_\mathrm{R}}{2\beta_\mathrm{R}^2E_\mathrm{R}}\Delta E^2+\frac{q}{T_\mathrm{R}}\tilde{V}(\omega_\mathrm{RF},\tau_\mathrm{R},\Delta\tau)$
$\underline{(\Delta\varphi,\Delta E)}$: $\Delta\dot{\varphi}=\frac{\omega_\mathrm{RF}\eta_\mathrm{R}}{\beta_\mathrm{R}^2E_\mathrm{R}}\Delta E\,,\quad \Delta\dot{E}=\frac{q}{T_\mathrm{R}}\left[\hat{V}_1\sin\left(\varphi_\mathrm{R}+\Delta\varphi\right)\right.$ $\left.+\hat{V}_2\sin\left(2\varphi_\mathrm{R}+2\Delta\varphi+\psi\right)-V_\mathrm{R}\right]$ $\mathcal{H}(\Delta\varphi,\Delta E)=\frac{\omega_\mathrm{RF}\eta_\mathrm{R}}{2\beta_\mathrm{R}^2E_\mathrm{R}}\Delta E^2+\frac{q}{T_\mathrm{R}}\tilde{V}(1,\varphi_\mathrm{R},\Delta\varphi)$
$\underline{(\Delta\varphi,\Delta W)}$: $\Delta\dot{\varphi}=\frac{\omega_\mathrm{RF}^2\eta_\mathrm{R}}{\beta_\mathrm{R}^2E_\mathrm{R}}\Delta W\qquad \Delta\dot{W}=\frac{q}{2\pi h}\left[\hat{V}_1\sin\left(\varphi_\mathrm{R}+\Delta\varphi\right)\right.$ $\left.+\hat{V}_2\sin\left(2\varphi_\mathrm{R}+2\Delta\varphi+\psi\right)-V_\mathrm{R}\right]$ $\mathcal{H}(\Delta\varphi,\Delta W)=\frac{\omega_\mathrm{RF}^2\eta_\mathrm{R}}{2\beta_\mathrm{R}^2E_\mathrm{R}}\Delta W^2+\frac{q}{2\pi h}\tilde{V}(1,\varphi_\mathrm{R},\Delta\varphi)$

2.2.6 Phase Stability Principle

The ring-shape structure of the synchrotron requires that the momenta of all particles are within a certain range such that their trajectories in the ring determined by the magnetic lattice lay within the vacuum pipe. This is achieved by longitudinal phase focusing which leads to an oscillation of the single particles around the reference particle, as was demonstrated in Sec. 2.2.4. The trajectories in phase space are determined by the Hamiltonian function which is a constant of motion along the trajectories for adiabatic synchrotron motion [61]. Fig. 2.8 depicts the contour lines of the Hamiltonian in the $(\Delta\varphi,\ \Delta W)$-plane for $V_\mathrm{R} = 0$ and $h = 2$.

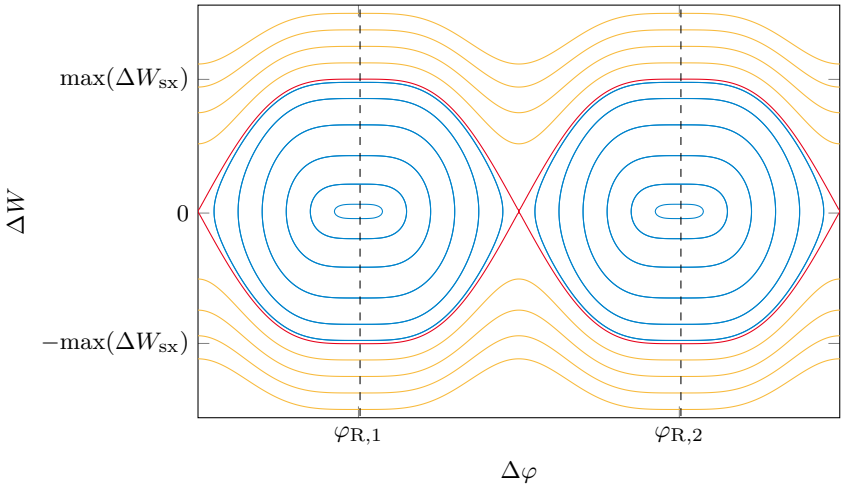

Figure 2.8: Trajectories for $V_\mathrm{R} = 0$ in phase space, being contour lines of the Hamiltonian function

The contour lines equal the trajectories of the single particles and are closed curves where the particles perform a stable oscillation around one of the two reference points, shown in blue. The red line is the so-called *separatrix* which separates the stable from the unstable area (yellow trajectories) and encloses the so-called *bucket*. All particles that are located within the buckets remain bunched as long as the separatrix is not changed, e. g. by a change of the voltage amplitudes. The trajectories for $V_\mathrm{R} = 0.4 \cdot \hat{V}_1$ below transition energy ($\gamma_\mathrm{R} < \gamma_\mathrm{t}$) can be seen in Fig. 2.9.

In this case particles outside the bucket may get lost if their orbit differs

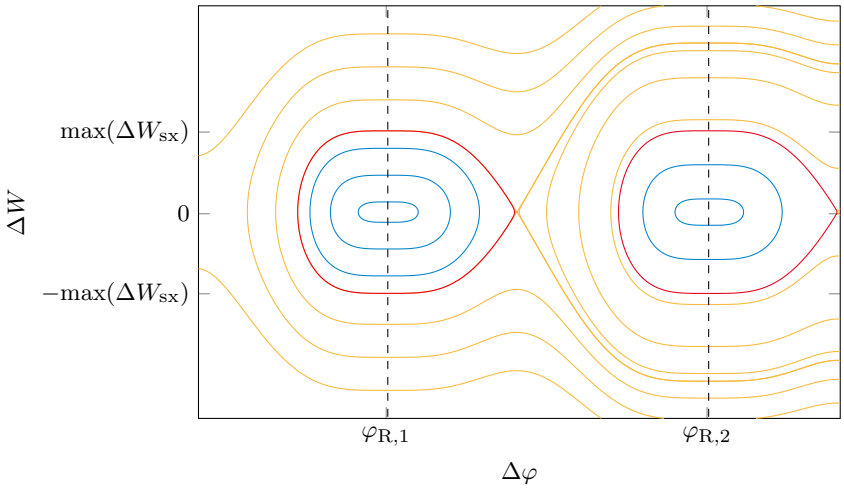

Figure 2.9: Trajectories for $V_\mathrm{R} = 0.4 \cdot \hat{V}_1$ in phase space

too much from the reference orbit because there are trajectories which lead to an unlimited ΔW. Above transition energy the buckets would be flipped at the dashed lines. Please note that the scale of the ΔW axis was not changed compared to Fig. 2.8. Instead, the bucket area decreased as will be discussed in the following section.

Each bucket has two fixed points [61] where

$$\Delta\dot{W} = 0\,, \quad \Delta\dot{\varphi} = 0\,,$$

namely the stable fixed point ($\varphi_\mathrm{sfp} = \varphi_\mathrm{R}$, $\Delta W_\mathrm{sfp} = 0$) and the unstable fixed point ($\varphi_\mathrm{ufp}, \Delta W_\mathrm{ufp} = 0$) where

$$\varphi_\mathrm{ufp} \in \mathcal{M}\,,\ \mathcal{M} = \{\varphi \,|\, -\pi < \varphi \leq \pi\,,\ \hat{V}_1 \sin(\varphi) + \hat{V}_2 \sin(2\varphi + \psi) = V_\mathrm{R}\} \setminus \varphi_\mathrm{R}\,. \tag{2.19}$$

In general the condition in Eq. (2.19) is only numerically solvable, except for $\varphi_\mathrm{R} = 0$ where $\varphi_\mathrm{ufp} = \pi$. The plot shows that although particles with different energies can be accelerated simultaneously as a bunch, their maximum energy deviation is limited to $\Delta W_i \leq \max(\Delta W_\mathrm{sx})$, the maximum energy deviation on the separatrix, if they do not have an additional phase deviation. In the latter case their allowed energy deviation is further decreased. Also note that the bucket size is decreased if $V_\mathrm{R} \neq 0$. This is accounted for by increasing the voltage amplitudes which is discussed

in more detail in Section 2.3.1. A bucket exists as long as the stability condition (2.14),

$$-\eta_{\mathrm{R}} \cos(\varphi_{\mathrm{R}}) > 0$$

holds. This is valid for a single- as well as for a dual-harmonic cavity system. However, the bucket shrinks faster (in terms of the reference voltage) in the latter case as $\cos(\varphi_{\mathrm{R}}) = 0$ is already met for $V_{\mathrm{R}} = 0.75\hat{V}_1$ in dual-harmonic mode (cf. Eq. 2.5b).

2.2.7 Summary

The longitudinal "position" of a particle relative to the reference can be specified for example by the spatial coordinate Δz, by the phase $\Delta\varphi$ or the arrival time $\Delta\tau$. They can be converted into each other by the relation

$$\Delta\varphi = \omega_{\mathrm{RF}}\Delta\tau = -\frac{\omega_{\mathrm{RF}}}{\beta_{\mathrm{R}} c}\Delta z\,.$$

Each of them can be regarded as a generalized coordinate for which a generalized momentum exists. The trajectories in phase space are the contour lines of the Hamiltonian function associated with the chosen phase space coordinate pair, and the flow is area-preserving according to Liouville's theorem. The trajectories are closed (quasi closed) curves if processes are stationary (adiabatic), and the equations of motion can be expressed either in the discrete domain, assuming that the crossing time T_{cross} which the particles need to cross the cavity gap is zero, or they can be expressed in the continuous domain assuming that the electric field is applied continuously along the orbit. The particles are bunched, and each bunch is placed within a bucket, which exists if the stability condition (2.14) is fulfilled.

2.3 Characteristics of the Dual-Harmonic Bucket

In literature usually only single-harmonic cavity systems are discussed [41, 62, 98]. This section shortly summarizes some characteristics of the dual-harmonic voltage which are obtained analogously to the single-harmonic case. All results are given for the phase space variables $(\Delta\varphi, \Delta W)$.

2.3.1 Bucket Area

As the bucket is enclosed by the separatrix, its area equals twice the integral over the function $\Delta W_{\mathrm{sx}}(\Delta\varphi)$ denoting the corresponding value of energy deviation on the separatrix for a given relative phase. Along the separatrix the associated Hamiltonian is constant and has the value

$$H_{\mathrm{sx}} = H(\Delta\varphi = \varphi_{\mathrm{ufp}} - \varphi_{\mathrm{R}}, \Delta W = 0)\,,$$

which is the Hamiltonian evaluated at the unstable fix point. The function $\Delta W_{\mathrm{sx}}(\Delta\varphi)$ describing the separatrix can thus be obtained by solving

$$H(\Delta\varphi, \Delta W_{\mathrm{sx}}(\Delta\varphi)) = H_{\mathrm{sx}} \tag{2.20}$$

for $\Delta W_{\mathrm{sx}}(\Delta\varphi)$.

Bucket Area in Stationary Case

For $V_{\mathrm{R}} = 0$, corresponding to $\varphi_{\mathrm{R}} = 0$, the unstable fix point equals π, and the Hamiltonian along the separatrix is easy to evaluate:

$$\begin{aligned} H_{\mathrm{sx}} &= H(\Delta\varphi = \pi, \Delta W = 0) \\ &= \frac{q}{2\pi h}\left[\hat{V}_1\left(\cos(\pi) - \cos(0) + \pi\sin(0)\right)\right. \\ &\qquad \left. + \hat{V}_2\left(\frac{1}{2}\cos(2\pi + \psi) - \frac{1}{2}\cos(\psi) + \pi\sin(\psi)\right)\right]\,, \end{aligned}$$

where according to (2.5) $\hat{V}_2 = \frac{1}{2}\hat{V}_1$ and $\psi = \pi$. Therefore,

$$H_{\mathrm{sx}} = -\frac{q\hat{V}_1}{\pi h} \tag{2.21}$$

follows. Inserting (2.21) into (2.20) yields

$$\begin{aligned} &\frac{\omega_{\mathrm{RF}}^2\eta_{\mathrm{R}}}{2\beta_{\mathrm{R}}^2 E_{\mathrm{R}}}\Delta W_{\mathrm{sx}}^2(\Delta\varphi) \\ &\quad + \frac{q\hat{V}_1}{2\pi h}\left[\cos(\Delta\varphi) - \cos(0) + \Delta\varphi\sin(0)\right. \\ &\qquad \left. + \frac{1}{2}\left(\frac{1}{2}\cos(2\Delta\varphi + \pi) - \frac{1}{2}\cos(\pi) + \Delta\varphi\sin(\pi)\right)\right] = -\frac{q\hat{V}_1}{\pi h}\,, \end{aligned}$$

$$\Leftrightarrow \Delta W_{\mathrm{sx}}^2(\Delta\varphi) = -\frac{2\beta_{\mathrm{R}}^2 E_{\mathrm{R}}}{\omega_{\mathrm{RF}}^2 \eta_{\mathrm{R}}} \frac{q\hat{V}_1}{2\pi h} \Bigg[2 + \cos(\Delta\varphi) - 1 + \frac{1}{4}\cos(2\Delta\varphi + \pi) + \frac{1}{4} \Bigg] ,$$

$$\Leftrightarrow \Delta W_{\mathrm{sx}}(\Delta\varphi) = \sqrt{-\frac{q\hat{V}_1 \beta_{\mathrm{R}}^2 E_{\mathrm{R}}}{4\omega_{\mathrm{RF}}^2 \eta_{\mathrm{R}} \pi h} \left[5 + 4\cos(\Delta\varphi) + \cos(2\Delta\varphi + \pi)\right]} .$$

The bucket area in the stationary case thus reads

$$A_{\mathrm{buck,st}} = \sqrt{-\frac{q\hat{V}_1 \beta_{\mathrm{R}}^2 E_{\mathrm{R}}}{\omega_{\mathrm{RF}}^2 \eta_{\mathrm{R}} \pi h}} \int_{-\pi}^{\pi} \sqrt{5 + 4\cos(\Delta\varphi) + \cos(2\Delta\varphi + \pi)}\, \mathrm{d}\Delta\varphi .$$

$$\approx 12.986 \cdot \sqrt{-\frac{q\hat{V}_1 \beta_{\mathrm{R}}^2 E_{\mathrm{R}}}{\omega_{\mathrm{RF}}^2 \eta_{\mathrm{R}} \pi h}} \tag{2.22}$$

Note that the bucket area was derived for $\varphi_{\mathrm{R}} = 0$ corresponding to the stable reference phase of a beam below transition energy. In this case $\eta_{\mathrm{R}} < 0$ holds and the argument of the square root is positive.

Bucket Area in Case of Acceleration

For $\varphi_{\mathrm{R}} \neq 0$ the unstable fix point φ_{ufp} and therefore also the bucket area can only be obtained numerically. For increasing V_{R} and fixed $\hat{V}_1$, $A_{\mathrm{buck,acc}}$ is shown in Fig. 2.10 as a multiple of the stationary bucket area $A_{\mathrm{buck,st}}$. The bucket vanishes for $V_{\mathrm{R}} = 0.75 \cdot \hat{V}_1$ corresponding to $\varphi_{\mathrm{R}} = \pi/2$. In the literature the approximation

$$\frac{A_{\mathrm{buck,acc}}}{A_{\mathrm{buck,st}}} \approx \frac{1 - \sin(\varphi_{\mathrm{R}})}{1 + \sin(\varphi_{\mathrm{R}})} \tag{2.23}$$

for the ratio of the bucket area in case of acceleration and the stationary bucket for fixed $\hat{V}$ in the single-harmonic case can be found [61]. A similar result for the dual-harmonic cavity mode can be obtained by means of a least squares approximation. Taking (2.23) as an ansatz, the area of an accelerating bucket can be approximated as

$$\frac{A_{\mathrm{buck,acc}}}{A_{\mathrm{buck,st}}} \approx \frac{(1 - \sin(\varphi_{\mathrm{R}}))^p}{(1 + \sin(\varphi_{\mathrm{R}}))^q} = \frac{\left(1 - \frac{4}{3}\frac{V_{\mathrm{R}}}{\hat{V}_1}\right)^p}{\left(1 + \frac{4}{3}\frac{V_{\mathrm{R}}}{\hat{V}_1}\right)^q} \tag{2.24}$$

with

$$p = 1.02595\,, \quad q = 0.06378\,.$$

Taking a look at Fig. 2.10 also suggests an approximation

$$\frac{A_{\mathrm{buck,acc}}}{A_{\mathrm{buck,st}}} \approx -\frac{4}{3}\frac{V_{\mathrm{R}}}{\hat{V}_1} + 1 \tag{2.25}$$

affine in V_{R}. Both approximations are also shown in Fig. 2.10. The relative error

$$\epsilon = \frac{A_{\mathrm{buck,acc,approx}} - A_{\mathrm{buck,acc}}}{A_{\mathrm{buck,acc}}}$$

is depicted in Fig. 2.11 for $0 \leq V_{\mathrm{R}}/\hat{V}_1 \leq 0.5$. For larger V_{R} the relative error increases strongly as $A_{\mathrm{buck,acc}}$ approaches zero. For reasonable reference voltages, Eq. (2.25) is thus a simple and eventually sufficiently accurate approximation. During operation the bucket area decrease is usually compensated by increasing the voltage amplitude $\hat{V}$. The length of the bucket along the phase axis in nonetheless decreased.

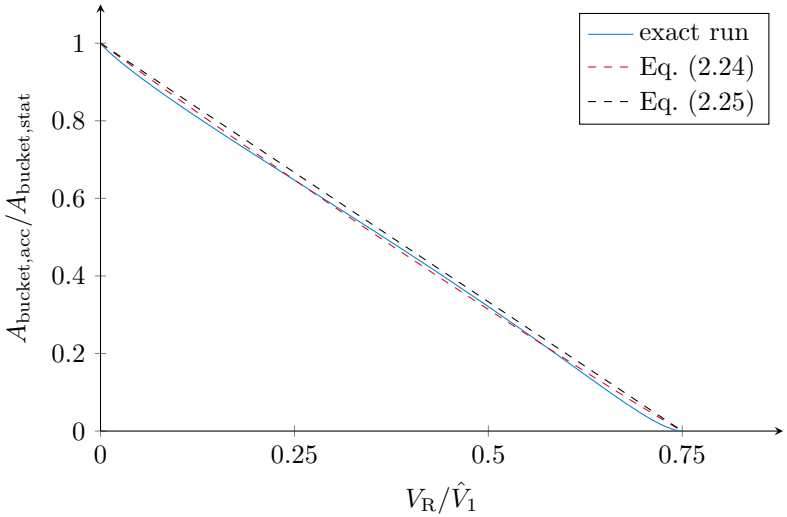

Figure 2.10: Bucket area for accelerated beam

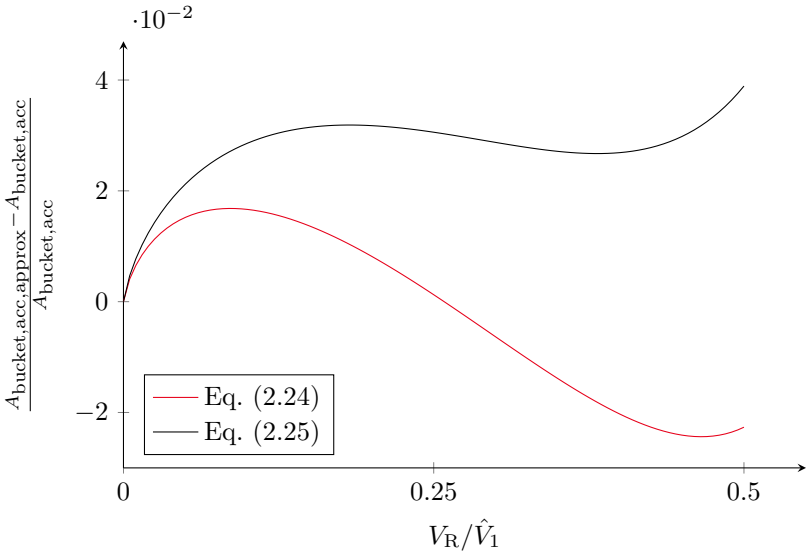

Figure 2.11: Relative error of bucket area approximations

2.3.2 Synchrotron Frequency

The *synchrotron frequency* f_{syn} denotes the oscillation frequency of a single particle around the reference. A common way to estimate f_{syn} in the single-harmonic case is to linearize the sinusoidal voltage around the reference, which is assumed to be close to zero [61, 98]. The estimation furthermore only holds for small bunches [62] for which the synchrotron frequency of the linearized bucket reads

$$f_{\text{syn},0} = f_{\text{R}} \sqrt{-\frac{hq\hat{V}\eta_{\text{R}} \cos(\varphi_{\text{R}})}{2\pi\beta_{\text{R}}^2 E_{\text{R}}}} \tag{2.26}$$

with the amplitude $\hat{V}$ of the total voltage provided by both cavities. For a dual-harmonic cavity system, linearization of the combined voltage around $\Delta\varphi = 0$ is not constructive due to the saddle point at φ_{R}. Instead, the synchrotron frequency has to be calculated by an integration along the trajectory under consideration depending on the oscillation amplitude, similar to the case of big amplitudes in the single-harmonic case [61, 62]:

$$\Delta\dot{\varphi} = \frac{\mathrm{d}\Delta\varphi}{\mathrm{d}t}$$

$$\Leftrightarrow T_{\mathrm{syn}} = \oint \mathrm{d}t = \oint \frac{1}{\Delta\dot{\varphi}}\,\mathrm{d}\Delta\varphi\,. \tag{2.27}$$

The dependency of $\Delta\dot{\varphi}$ in (2.27) on ΔW according to (2.16b) can be eliminated by using the fact that the Hamiltonian is constant along the trajectory. Considering an arbitrary trajectory with the extrema $\Delta\varphi^-$ and $\Delta\varphi^+$, the associated Hamiltonian has the value

$$\mathcal{H}_{\mathrm{traj}} = \frac{q}{2\pi h}\tilde{V}(1,\varphi_{\mathrm{R}},\Delta\varphi^+) = \frac{q}{2\pi h}\tilde{V}(1,\varphi_{\mathrm{R}},\Delta\varphi^-)\,,$$

where again the abbreviation $\tilde{V}(\xi,\varphi_{\mathrm{R}},\Delta\varphi)$ according to (2.18) was used. Thus

$$\Delta\dot{\varphi} = \frac{\omega_{\mathrm{RF}}^2\eta_{\mathrm{R}}}{\beta_{\mathrm{R}}^2 E_{\mathrm{R}}}\sqrt{\frac{2\beta_{\mathrm{R}}^2 E_{\mathrm{R}}}{\omega_{\mathrm{RF}}^2\eta_{\mathrm{R}}}\left(\mathcal{H}_{\mathrm{traj}} - \frac{q}{2\pi h}\tilde{V}(1,\varphi_{\mathrm{R}},\Delta\varphi)\right)}$$

and Eq. (2.27) reads

$$T_{\mathrm{syn}}(\Delta\varphi^+) = \oint \left[\frac{\omega_{\mathrm{RF}}^2\eta_{\mathrm{R}}q}{\pi h\beta_{\mathrm{R}}^2 E_{\mathrm{R}}}\left(\tilde{V}(1,\varphi_{\mathrm{R}},\Delta\varphi^+) - \tilde{V}(1,\varphi_{\mathrm{R}},\Delta\varphi)\right)\right]^{-1/2}\mathrm{d}\Delta\varphi\,. \tag{2.28}$$

The synchrotron frequency $f_{\mathrm{syn}} = \frac{1}{T_{\mathrm{syn}}}$ as a function of $\Delta\varphi^+$ is depicted in Fig. 2.12 for $V_{\mathrm{R}} = 0$. The corresponding bunch parameters can be found in Tab. B.1 in the appendix.

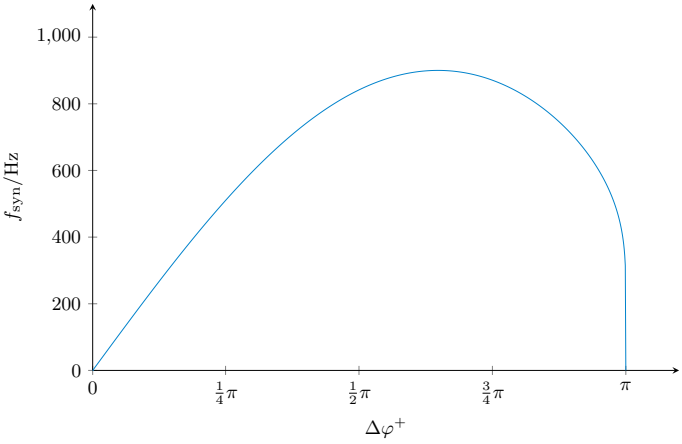

Figure 2.12: Synchrotron frequency for different trajectories and $V_{\mathrm{R}} = 0$

2.4 Acceleration Cycle

This section intends to give a short overview on the process of an acceleration cycle covering injection of the particles into the synchrotron, capturing, acceleration and extraction.

Pre-acceleration and Injection:

Before injection, the particles are pre-accelerated in a linear accelerator. The *UNILAC* at GSI Helmholtzzentrum für Schwerionenforschung GmbH is able to accelerate any (stable) element from the periodic table [3]. Via a so-called *kicker magnet* the particles are injected into the synchrotron as micro bunches which then debunch into a coasting beam. The coasting beam is *captured* as explained in the following.

Another possibility of injection, which is however not given for the SIS18, is the injection of an already bunched beam, e. g. by another synchrotron. In this case the cavity system of the receiving synchrotron has to provide an appropriate voltage to establish adequate buckets. The injection has to be done with caution or elsewise coherent bunch oscillations (see Chap. 3) or particle loss may occur.

Capturing:

The voltage amplitudes of the cavities are kept low after injection of the micro bunches and slowly increased after the particles have debunched into a coasting beam. The coasting beam is then re-captured in bunches placed in the buckets. As the bucket area is directly linked to the voltage amplitude $\hat{V}_1$ according to (2.22), increasing the voltage enables particles with an energy deviation $\Delta W \neq 0$ to enter the bucket. Fig. 2.13 depicts the capturing process.

Acceleration:

In order to apply an accelerating reference voltage $V_\mathrm{R} \neq 0$, the reference phase φ_R has to be changed. This is done by simultaneously ramping the magnetic dipole fields $\boldsymbol{B}$ and the cavity frequency f_RF. In order to run an adiabatic process, however, $\dot{\boldsymbol{B}}$ must not jump as is demonstrated below. During acceleration, the bucket area decreases as demonstrated in Sec. 2.3.1. This is compensated by increasing the cavity voltage amplitudes accordingly.

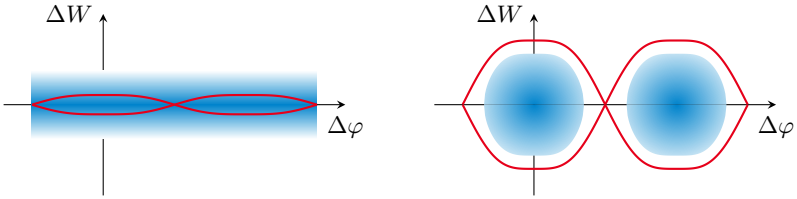

(a) Coasting beam with small voltage amplitudes

(b) Captured bunches after increasing the voltage amplitudes

Figure 2.13: Schematic drawing of capturing process

The required reference voltage V_R is given by the equilibrium of the Lorentz and the centripetal force, reading

$$\begin{aligned}
F_\mathrm{L,R} &= F_\mathrm{c,R} \\
\Leftrightarrow q v_\mathrm{R} B &= \frac{\gamma_\mathrm{R} m_0 v_\mathrm{R}^2}{\rho} \\
\Leftrightarrow q\rho\dot{B} &= m_0(\dot{\gamma}_\mathrm{R} v_\mathrm{R} + \dot{v}_\mathrm{R}\gamma_\mathrm{R}) \\
&= m_0\dot{\gamma}_\mathrm{R}\left(v_\mathrm{R} + \frac{c^2}{v_\mathrm{R}\gamma_\mathrm{R}^2}\right) \\
&= m_0\dot{\gamma}_\mathrm{R}\frac{c^2}{v_\mathrm{R}} \\
\Leftrightarrow q\rho L_\mathrm{R}\dot{B} &= m_0 T_\mathrm{R}\dot{\gamma}_\mathrm{R} c^2 \\
&= T_\mathrm{R}\dot{E}_\mathrm{R} \\
&\approx E_\mathrm{R}(k+1) - E_\mathrm{R}(k) \\
&= q V_\mathrm{R} \\
\Rightarrow V_\mathrm{R} &= \rho L_\mathrm{R}\dot{B}\,,
\end{aligned}$$

where the relations

$$\dot{\gamma} = \gamma^3\frac{v\dot{v}}{c^2}$$

and

$$\frac{c^2}{v\gamma^2} = \frac{c^2}{v} - v$$

were used. As $\dot{B} \sim V_\mathrm{R} = 0.75\hat{V}_1\sin(\varphi_\mathrm{R})$, the reference phase would jump if $\dot{B}$ jumps and the process would not be adiabatic. The radius ρ is de-

termined by the bending radius of the dipole magnets and amounts to 10 m for the SIS18. A schematic drawing of the beam energy E_R and the derivative of the magnetic dipole fields $\dot{B}$ is shown in Fig. 2.14. The beam is extracted after reaching the extraction energy $E_\mathrm{R,ext}$. In the synchrotron SIS18 the magnets can be ramped with a maximum derivative of $\dot{B}_\mathrm{max} = 4.2\,\frac{\mathrm{T}}{\mathrm{s}}$ [30].

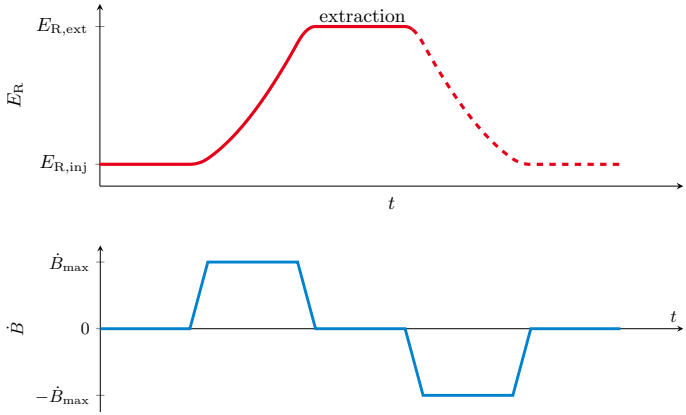

Figure 2.14: Schematic drawing of beam energy gain and magnetic ramp

Extraction:

Extraction of the beam can be done in two different ways denoted as fast and slow extraction. Fast extraction means that one or more bunches are extracted completely within one turn. To extract the beam slowly, it can either remain bunched or be debunched by decreasing the voltage amplitudes before extraction, losing phase focusing. After extraction the particles are for example directed on a target, stored in a storage ring or further accelerated in another synchrotron.

2.5 Discussion

The longitudinal beam dynamics of single particles relative to the reference particle can be described either in the continuous or in the discrete time domain. Each particle represents a Hamiltonian system where the

Hamiltonian is a constant of motion along the trajectories in phase space, and the trajectories are closed curves if the particles are within a bucket and changes are adiabatic. Buckets exist only if the stability condition

$$-\eta_{\mathrm{R}} \cos(\varphi_{\mathrm{R}}) > 0$$

holds and their area decreases for increasing φ_{R} if the voltage amplitudes are unchanged. Due to the dual-harmonic cavity system another nonlinear term is introduced in the equations of motion of the particles, and a saddle point is created around the reference point. Thus the bunch is lengthened and the particle trajectories contain a drift section.

3 Coherent Bunch Oscillation

While the previous chapter treated the longitudinal dynamics of single particles, this chapter focuses on the behavior of the entire bunch in the presence of guiding fields and disturbances, which is of more interest than the characteristics of a single particle from an operational point of view.

After a short introduction, the density function of a bunch denoting the distribution of the particles in phase space is considered in Sec. 3.2. A bunch is called *undisturbed* or *matched*, if the contour lines of the density function match the trajectories of the single particles. If the bunch is unmatched, however, coherent bunch oscillations of different order occur, depending on the type of disturbance. The single particle still follows its dedicated trajectory, but the shape of the bunch as well as the bunch barycenter may oscillate as illustrated in Sec. 3.1 and discussed in more detail in the following. Because the voltage as a function of $\Delta\varphi$ is nonlinear, there is a synchrotron frequency spread resulting in a *filamentation* of the bunch, changing its shape respectively the distribution function, but also ceasing longitudinal bunch oscillations. The frequency spread also leads to *Landau damping* named after L. D. Landau who described the principle for an electronic plasma in 1946 [60]. Sec. 3.3 explores the subject in depth. Modeling of coherent bunch oscillations is treated in Sec. 3.4 before the chapter ends with a discussion in Sec. 3.5.

3.1 Introduction

Assuming an ideal synchrotron with ideal components, ideal operation and no interference between the single particles or between the beam and the surroundings, a bunch would always be matched and no coherent motion would occur. Energy deviations would simply lead to stable incoherent synchrotron oscillations in the longitudinal direction as discussed in Chap. 2, and to stable betatron oscillations in the transverse directions [62]. A real bunch is however subject to various disturbances, possibly driving coherent bunch oscillations. Examples for the most common disturbances according to [16] are

- fluctuations of the magnetic field leading for instance to a varying orbit length and thus to arrival time or phase errors,
- incorrect injection of a bunched beam leading to phase errors if the bunch is injected at the wrong moment, and to voltage amplitude errors if the bucket height is incorrect,
- noise in the frequency generators of the cavities resulting in phase errors,
- ripples in the cavity power amplifiers resulting in voltage amplitude errors.

Another source of coherent dipole oscillations in the SIS18 is described in [15]. If the energy of the particles injected from the linear accelerator does not match the cavity frequency, the bunches are captured with an energy offset. An oscillation of the bunch barycenter is denoted as *dipole oscillation*, whereas an oscillation of the bunch length is called *quadrupole oscillation*. Higher order modes are called *sextupole, octupole*, etc. accordingly and refer to an oscillation of the bunch shape in phase space. They occur in rarer cases and are not considered in this dissertation. In the following, only the dipole oscillation is subject to beam feedback design and analysis. Dipole oscillations occur, if a phase or energy error exists, while quadrupole oscillations are driven by voltage amplitude errors.

An overview on the different oscillation modes can be found e. g. in [51, 62, 80, 86] and is also given in Fig. 3.1 for dipole and quadrupole oscillation, where the bunch in phase space along with the corresponding particle line density λ is depicted. The mode number $m \in \mathbb{N}_0$ can be defined according to the bunch position and shape in phase space. For $m = 0$ the bunch is matched and no coherent oscillation is present, $m = 1$ stands for dipole oscillations, $m = 2$ for quadrupole oscillations and so on. In case of a dipole oscillation the bunch barycenter oscillates with the *coherent synchrotron frequency* $f_{\mathrm{syn,coh}}$ which is subject of Subsec. 3.2.3. If more than one bunch is present in the accelerator, coupled-bunch oscillations may occur which are distinguished by the mode number n [79, 87]. These are however not considered in this dissertation and bunches are assumed to oscillate in-phase, corresponding to the coupled-bunch mode number $n = 0$.

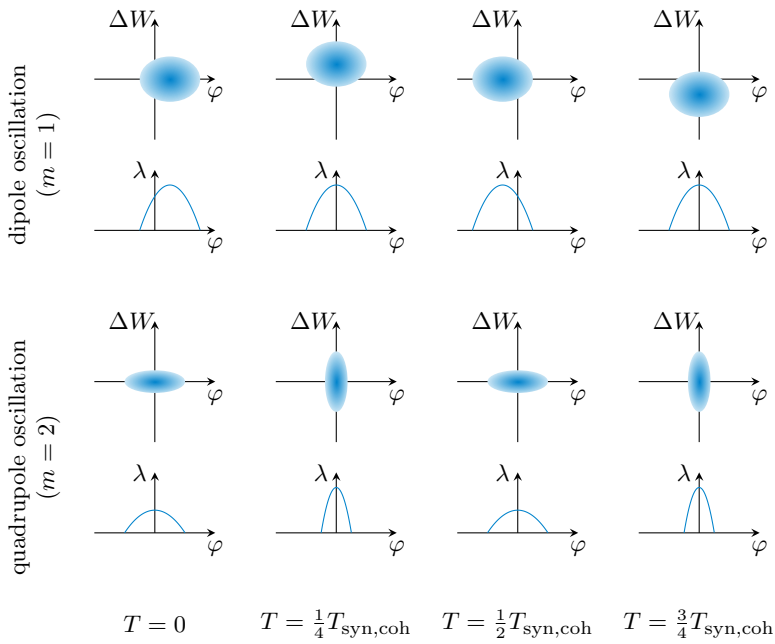

Figure 3.1: Illustration of dipole and quadrupole oscillation in phase space and corresponding line density λ

3.2 Properties of Particle Bunches

In this section important properties of particle bunches are reviewed. Subsec. 3.2.1 introduces *distribution functions* determining the particle density at a certain location in phase space. The area occupied by the bunch in phase space is characterized by the *root mean square emittance* introduced in Subsec. 3.2.2 which will become important for the evaluation of the performance of beam feedback systems. Finally the frequency of coherent dipole oscillations is derived in Subsec. 3.2.3.

3.2.1 Distribution Function

The bunch in phase space is either determined by the location of all single particles (where a bunch can contain a number of particles in the order of 10^7 to 10^{11} or more), or by a distribution function $f(\Delta\varphi, \Delta W, t)$ repre-

senting the particle density at a certain location $(\Delta\varphi, \Delta W)$ in phase space at time t.

The distribution function is usually normalized to

$$\int_{-\infty}^{\infty}\int_{-\infty}^{\infty} f(\Delta\varphi, \Delta W, t)\,\mathrm{d}\Delta\varphi\,\mathrm{d}\Delta W = 1 \quad \forall\, t\,, \tag{3.1}$$

and its contour lines match the trajectories of the particles in phase space, if the bunch is matched. This leads to a distribution function which only depends on the Hamiltonian $\mathcal{H}(\Delta\varphi, \Delta W)$ and not explicitly on the phase space variables themselves. Thus any distribution function $f = f(\mathcal{H})$ describes a matched bunch [22].

Assuming that the energy deviation is Gaussian distributed which is in general the case, this results in the density function

$$f\left(\mathcal{H}(\Delta\varphi, \Delta W)\right) = c_1 \exp\left\{-\frac{\mathcal{H}(\Delta\varphi, \Delta W)}{c_2}\right\}$$

with

$$c_2 = \frac{\omega_{\mathrm{RF}}^2 \eta_{\mathrm{R}} \sigma_{\Delta W}^2}{\beta_{\mathrm{R}}^2 E_{\mathrm{R}}}$$

and $\sigma_{\Delta W}$ being the standard deviation of ΔW. The constant c_1 normalizing the distribution function has to be calculated numerically as well as the resulting line density $\lambda(\Delta\varphi)$. If the distibution function f is not normalized according to Eq. (3.1), the line density λ is the projection of f on the $\Delta\varphi$-axis.

Other common distribution functions are the purely Gaussian (where not only the energy but also the phase deviation are Gaussian distributed), the parabolic, the Hofmann-Pedersen [43] or the uniform distribution as well as a combination of parabolic and Gaussian distribution. These are listed in Tab. 3.1. Note that the so-described bunch is not exactly matched if the distribution functions are not a function $f = f(\mathcal{H})$ of the Hamiltonian. A good approximation for the distribution of a matched bunch is given by the parabolic-Gaussian function where the particle energy is Gaussian distributed and the phase follows a parabolic distribution. The index B denotes the barycenter of the bunch.

Table 3.1: Overview on common distribution functions

Gaussian distribution $f(\Delta\varphi, \Delta W) = \frac{1}{2\pi\sigma_{\Delta\varphi}\sigma_{\Delta W}} \exp\left\{-\frac{(\Delta\varphi-\Delta\varphi_\mathrm{B})^2+(\Delta W-\Delta W_\mathrm{B})^2}{2\sigma^2_{\Delta\varphi}\sigma^2_{\Delta W}}\right\}$ $\lambda(\Delta\varphi) = \frac{1}{\sqrt{2\pi}\sigma_{\Delta\varphi}} \exp\left\{-\frac{(\Delta\varphi-\Delta\varphi_\mathrm{B})^2}{2\sigma^2_{\Delta\varphi}}\right\}$
parabolic distribution $f(\Delta\varphi, \Delta W) = \frac{1}{3\pi\sigma_{\Delta\varphi}\sigma_{\Delta W}} \left(1 - \frac{(\Delta\varphi-\Delta\varphi_\mathrm{B})^2}{6\sigma^2_{\Delta\varphi}} - \frac{(\Delta W-\Delta W_\mathrm{B})^2}{6\sigma^2_{\Delta W}}\right)$ $\lambda(\Delta\varphi) = \frac{2\left(6\sigma^2_{\Delta\varphi}-(\Delta\varphi-\Delta\varphi_\mathrm{B})^2\right)^{3/2}}{27\pi\sigma^4_{\Delta\varphi}}$
parabolic-Gaussian distribution $f(\Delta\varphi, \Delta W) = \frac{3}{20\sqrt{10\pi}\sigma^3_{\Delta\varphi}\sigma_{\Delta W}} \exp\left\{-\frac{(\Delta W-\Delta W_\mathrm{B})^2}{2\sigma^2_{\Delta W}}\right\}$ $\cdot \left(5\sigma^2_{\Delta\varphi} - (\Delta\varphi - \Delta\varphi_B)^2\right)$ $\lambda(\Delta\varphi) = \frac{3}{20\sqrt{5}\sigma^3_{\Delta\varphi}} \left(5\sigma^2_{\Delta\varphi} - (\Delta\varphi - \Delta\varphi_B)^2\right)$
Hofmann-Pedersen distribution $f(\Delta\varphi, \Delta W) = c\sqrt{\mathcal{H}(\Delta\varphi^+,0) - \mathcal{H}(\Delta\varphi, \Delta W)}\,,$ $c = \text{const.}\,, \quad \Delta\varphi^+ = \text{bunch boundary}$ $\lambda(\Delta\varphi) = \frac{1}{u(\Delta\varphi^-,\Delta\varphi^+)}(U(\Delta\varphi) - U(\Delta\varphi^+))$ $u(\Delta\varphi^-,\Delta\varphi^+) = \int_{\Delta\varphi^-}^{\Delta\varphi^+} U(\Delta\varphi) - U(\Delta\varphi^+)\,\mathrm{d}(\Delta\varphi)$ $U(\Delta\varphi) = \int_0^{\Delta\varphi} V(\Delta\tilde{\varphi}) - V_\mathrm{R}\,\mathrm{d}(\Delta\tilde{\varphi})$
uniform distribution

$$f(\Delta\varphi, \Delta W) = \begin{cases} \frac{1}{4\pi\sigma_{\Delta\varphi}\sigma_{\Delta W}}\,, & \left(\frac{\Delta\varphi}{2\sigma_{\Delta\varphi}}\right)^2 + \left(\frac{\Delta W}{2\sigma_{\Delta W}}\right)^2 \leq 1 \\ 0\,, & \text{else} \end{cases}$$

$$\lambda(\Delta\varphi) = \begin{cases} \frac{1}{\pi\sigma_{\Delta\varphi}}\sqrt{1 - \frac{(\Delta\varphi - \Delta\varphi_{\mathrm{B}})^2}{4\sigma_{\Delta\varphi}^2}}\,, & |\Delta\varphi - \Delta\varphi_{\mathrm{B}}| \leq 2\sigma_{\Delta\varphi} \\ 0\,, & \text{else} \end{cases}$$

3.2.2 Longitudinal Root Mean Square Emittance

As will be shown in Sec. 3.3, coherent bunch oscillations may increase the bunch size in phase space. A measure for the region in phase space occupied by a bunch is the root mean square (rms) emittance ϵ. If multiplied by π the emittance equals the area covered by an ellipse which encircles all points in phase space located within the standard deviation around the barycenter [66, 85, 98],

$$\pi\epsilon = \pi\sqrt{\sigma_{\Delta\varphi}^2\sigma_{\Delta W}^2 - \sigma_{\Delta\varphi,\Delta W}^4} \tag{3.2}$$

with the variances $\sigma_{\Delta\varphi}^2$ and $\sigma_{\Delta W}^2$ and the covariance $\sigma_{\Delta\varphi,\Delta W}^2$.

For elliptical distribution functions the emittance is also a measure for the area

$$A_{\mathrm{bunch}} \propto \epsilon$$

occupied by the bunch.

A higher emittance is linked to a lengthening of the bunch and an increase of the maximum energy deviation. This may be undesired for certain beam experiments or applications which is why a high beam quality is characterized by a low rms emittance. In Chap. 5 the emittance is therefore used as a measure for the effectiveness of the beam phase controllers.

3.2.3 Coherent Synchrotron Frequency

An important property of bunch disturbances is the oscillation frequency of the particular coherent motion. It is not only a characteristic for the determination of occurring disturbances, but also necessary for various modeling and controller design approaches [51, 52], [105, 111].

If a small bunch in a single-harmonic bucket is considered, all particles have approximately the same synchrotron frequency $f_{\mathrm{syn},0}$ according to (2.26) which is also the frequency of the dipole oscillation.

This approximation is as already mentioned not possible in case of a dual-harmonic cavity system due to the saddle point in φ_{R}. Therefore in the following other approaches to determine the synchrotron frequency of the dipole oscillation, which will further on be referred to as *coherent synchrotron frequency* $f_{\mathrm{syn,coh}}$, are presented.

According to [15, 43], the net force F acting on a bunch rigidly displaced by a phase $\Delta\varphi_{\mathrm{B}}$ is proportional to the integral of the potential $V(\Delta\varphi)-V_{\mathrm{R}}$ and the line density of the displaced bunch $\lambda(\Delta\varphi - \Delta\varphi_{\mathrm{B}})$. For small displacements this results in the coherent synchrotron frequency

$$f_{\mathrm{syn,coh}}^2 = f_{\mathrm{syn},0}^2 \frac{1}{|u|} \int\limits_{\Delta\varphi^-}^{\Delta\varphi^+} \left(\frac{V(\Delta\varphi) - V_{\mathrm{R}}}{\hat{V}_1} \right)^2 \mathrm{d}(\Delta\varphi) \,,$$

where $\Delta\varphi^-$ ($\Delta\varphi^+$) denotes the left (right) border of the bunch which is assumed to be Hofmann-Pedersen distributed, and again (see the Hofmann-Pedersen distribution in Tab. 3.1)

$$u = \int\limits_{\Delta\varphi^-}^{\Delta\varphi^+} U(\Delta\varphi) - U(\Delta\varphi^+) \,\mathrm{d}(\Delta\varphi) \,.$$

For a stationary bucket in a dual-harmonic RF system with $\Delta\varphi^- = \Delta\varphi^+$, one obtains [15]

$$\left(\frac{f_{\mathrm{syn,coh}}}{f_{\mathrm{syn},0}} \right)^2 = \frac{-\frac{5}{4}\Delta\varphi^+ + \sin(\Delta\varphi^+) + \frac{1}{2}\sin(2\Delta\varphi^+) - \frac{1}{3}\sin(3\Delta\varphi^+) + \frac{1}{16}\sin(4\Delta\varphi^+)}{2\Delta\varphi^+\cos(\Delta\varphi^+) - \frac{1}{2}\Delta\varphi^+\cos(2\Delta\varphi^+) - 2\sin(\Delta\varphi^+) + \frac{1}{4}\sin(2\Delta\varphi^+)} \,. \tag{3.3}$$

Another approach to estimate the coherent synchrotron frequency in a stationary bucket was first introduced in [62] and further discussed in [111]. It is based on the assumption that in a single-harmonic RF regime the coherent synchrotron frequency of a stationary bunch equals the synchrotron frequency of a particle with the maximum phase deviation $\Delta\varphi^+ = 2\sigma_{\Delta\varphi}$.

In the single-harmonic RF regime, the synchrotron frequency given by (2.28) can be expressed in terms of the complete elliptic integral of the first kind, $K(\Delta\varphi)$ yielding

$$f_{\mathrm{syn,sh}}(\Delta\varphi^+) = f_{\mathrm{syn},0}\frac{\pi}{2K(\sin(\Delta\varphi^+/2))}\,,$$
$$f_{\mathrm{syn,coh}} = f_{\mathrm{syn,sh}}(\Delta\varphi^+ = 2\sigma_{\Delta\varphi})\,.$$

For a dual-harmonic cavity system, the synchrotron frequency of a single particle with maximum phase deviation $\Delta\varphi^+$ in a stationary bunch reads

$$f_{\mathrm{syn,dh}}(\Delta\varphi^+) = f_{\mathrm{syn},0}\frac{\pi\sin(\Delta\varphi^+/2)}{\sqrt{2}K\sqrt{\frac{1}{2}\left(1+\sin^2(\Delta\varphi^+/2)\right)}} \tag{3.4}$$

as demonstrated in [61]. The coherent synchrotron frequency in this case is given by [111]

$$f_{\mathrm{syn,coh}} = f_{\mathrm{syn,dh}}\left(\Delta\varphi^+ = 2.19\cdot\sigma_{\Delta\varphi} - 1.05\cdot\frac{\sigma_{\Delta\varphi}^2}{\pi}\right)\,.$$

A third method results from the modeling of coherent bunch oscillations by means of *central moments* of the distribution function which is discussed in detail in Sec. 3.4. Fig. 3.2 shows the presented estimations of the coherent synchrotron frequency compared to simulations with bunches of different length. For each bunch length five different bunches were simulated and the average value is plotted in Fig. 3.2. The values of the synchrotron frequencies obtained for each bunch length differ only little with a variance of less than 6 Hz which is why the variances are not shown in the plot.

3.3 Filamentation and Landau Damping

According to (2.28) the synchrotron frequency of a single particle depends on its maximum phase deviation $\Delta\varphi^+$ resulting in a frequency spread as shown in Fig. 2.12 for the stationary case. In the following it is demonstrated that the coherent motion of a set of oscillators, driven by an external force is damped, if the single oscillators have different resonance frequencies. This phenomenon is called Landau damping and was first described by L. D. Landau in 1946 [60]. For the same reasons also non-vanishing initial conditions like a rigid bunch displacement cease after some time. Additional literature includes for example [22, 42, 61].

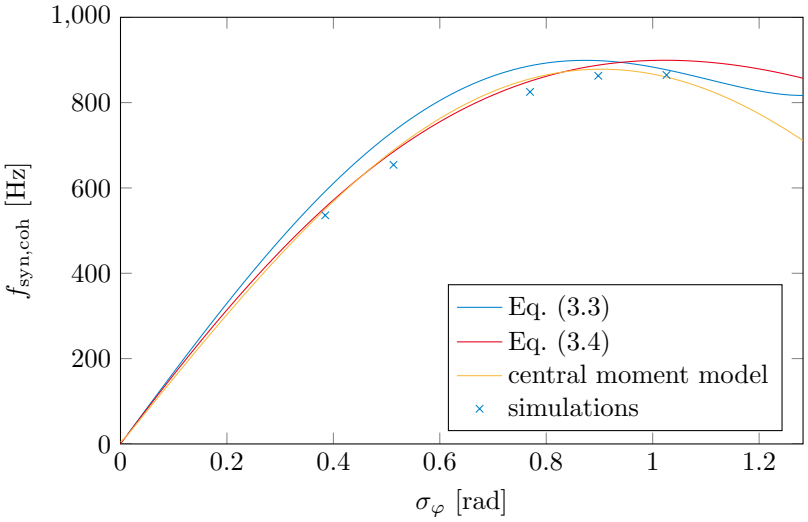

Figure 3.2: Comparison of the different estimation approaches for the coherent synchrotron frequency

Considering a set of undamped oscillators

$$\ddot{x}_j + \omega_{\mathrm{r}j}^2 x_j = u \tag{3.5}$$

with different resonant frequencies $\omega_{\mathrm{r}j}$ and initial conditions $x_j(0) = 0$, $\dot{x}_j(0) = 0$, driven by an external force

$$u(t) = A\cos(\Omega t)\,,$$

the solution of (3.5) is [22]

$$x_j(t > 0) = -\frac{A}{\Omega^2 - \omega_{\mathrm{r}j}^2}(\cos(\Omega t) - \cos(\omega_{\mathrm{r}j} t))\,. \tag{3.6}$$

If the resonant frequencies $\omega_{\mathrm{r}j}$ are distributed according to

$$f(\omega_{\mathrm{r}})\,, \quad \int f(\omega_{\mathrm{r}})\,\mathrm{d}\omega_{\mathrm{r}} = 1\,,$$

the barycenter displacement is given by the superposition

$$x_{\mathrm{B}}(t > 0) = -\int_{-\infty}^{\infty} f(\omega_{\mathrm{r}})\frac{A}{\Omega^2 - \omega_{\mathrm{r}}^2}(\cos(\Omega t) - \cos(\omega_{\mathrm{r}} t))\,\mathrm{d}\omega_{\mathrm{r}}\,. \tag{3.7}$$

Following the procedure in [22, 42], a narrow beam spectrum with center frequency $\omega_{\mathrm{r}0}$ and a driving force close to the spectrum is considered. In this case (3.7) can be simplified to

$$x_{\mathrm{B}}(t) = -\frac{A}{2\omega_{\mathrm{r}0}} \int_{-\infty}^{\infty} f(\omega_{\mathrm{r}}) \frac{1}{\Omega - \omega_{\mathrm{r}}} (\cos(\Omega t) - \cos(\omega_{\mathrm{r}} t)) \, \mathrm{d}\omega_{\mathrm{r}}$$

and a change of variables from ω_{r} to $\nu = \omega_{\mathrm{r}} - \Omega$ yields

$$\begin{aligned} x_{\mathrm{B}}(t) &= \frac{A}{2\omega_{\mathrm{r}0}} \int_{-\infty}^{\infty} f(\nu + \Omega) \frac{1}{\nu} (\cos(\Omega t) - \cos(\Omega t + \nu t)) \, \mathrm{d}\nu \\ &= \frac{A}{2\omega_{\mathrm{r}0}} \left[\cos(\Omega t) \int_{-\infty}^{\infty} f(\nu + \Omega) \frac{1 - \cos(\nu t)}{\nu} \, \mathrm{d}\nu \right. \\ &\qquad \left. + \sin(\Omega t) \int_{-\infty}^{\infty} f(\nu + \Omega) \frac{\sin(\nu t)}{\nu} \, \mathrm{d}\nu \right] . \end{aligned} \tag{3.8}$$

For large t (neglecting transient effects) the two terms in (3.8) can be approximated by

$$\lim_{t \to \infty} \frac{\sin(\nu t)}{\nu} = \pi \delta(\nu) \, , \tag{3.9}$$

$$\lim_{t \to \infty} \frac{1 - \cos(\nu t)}{\nu} = \mathrm{P.V.} \left(\frac{1}{\nu} \right) . \tag{3.10}$$

The limit in (3.9) equals π times the δ-Distribution as the area under $\frac{\sin(\nu t)}{\nu}$ is $\pi \ \forall \ t$ and the function peaks around $\nu = 0$ for $t \to \infty$ with decreasing width. The limit in (3.10) is given by the Cauchy principal value P.V. [22, 67]. Eq. (3.8) therefore reads

$$x_{\mathrm{B}}(t) = \frac{A}{2\omega_{\mathrm{r}0}} \left[\cos(\Omega t) \mathrm{P.V.} \int \frac{f(\omega_{\mathrm{r}})}{\omega_{\mathrm{r}} - \Omega} \, \mathrm{d}\omega_{\mathrm{r}} + \pi f(\Omega) \sin(\Omega t) \right] ,$$

holding for $t > \frac{1}{\Delta\omega_{\mathrm{r}}}$, where $\Delta\omega_{\mathrm{r}}$ denotes the frequency spread of the system. To determine the work which is done on the set of oscillators, the energy of the single oscillators as the square of their amplitude is considered. From (3.6),

$$x_j(t > 0) = -\frac{A}{\Omega^2 - \omega_{\mathrm{r}j}^2} (\cos(\Omega t) - \cos(\omega_{\mathrm{r}j} t))$$

$$\approx -\frac{A}{2\omega_{\mathrm{r}0}(\Omega-\omega_{\mathrm{r}j})}\left[2\sin\left(\frac{\Omega t+\omega_{\mathrm{r}j}t}{2}\right)\sin\left(\frac{\Omega t-\omega_{\mathrm{r}j}t}{2}\right)\right],$$

the slowly changing envelope

$$\tilde{A}(t)=\frac{A}{\omega_{\mathrm{r}0}(\Omega-\omega_{\mathrm{r}j})}\sin\left(\frac{\Omega t-\omega_{\mathrm{r}j}t}{2}\right)$$

and the total energy

$$E(t)=N\int_{-\infty}^{\infty}f(\omega_{\mathrm{r}})\left[\frac{A}{\omega_{\mathrm{r}0}(\Omega-\omega_{\mathrm{r}})}\sin\left(\frac{\Omega t-\omega_{\mathrm{r}}t}{2}\right)\right]^2\mathrm{d}\omega_{\mathrm{r}} \qquad (3.11)$$

$$=\frac{NA^2}{\omega_{\mathrm{r}0}^2}\int_{-\infty}^{\infty}f(\nu+\Omega)\frac{\sin^2(\nu t/2)}{\nu^2}\,\mathrm{d}\nu$$

follow, where N is the total number of oscillators [22]. With the limit

$$\lim_{t\to\infty}\frac{\sin^2(\nu t/2)}{\nu^2}=\frac{\pi t}{2}\delta(\nu)$$

for large t, (3.11) is reduced to

$$E(t)=\frac{NA^2\pi}{2\omega_{\mathrm{r}0}}tf(\Omega)\,.$$

The total energy of the system increases linearly with time, which means that the system absorbs energy from the driving source while the oscillator ensemble response stays within bounds. The energy is stored within particles with a resonance frequency within a narrowing band around the driving frequency Ω. This is the essence of Landau damping. However, Landau damping will cease after a time $t>\frac{1}{\delta\omega_{\mathrm{r}}}$, where $\delta\omega_{\mathrm{r}}$ is the smallest frequency difference which occurs in the set of oscillators, as the number of oscillators is finite. Applied to the bunches of a particle beam, Landau damping might cease earlier when the resonance particles are lost because their amplitudes exceed the bucket limit.

Another kind of disturbance is the rigid displacement of the bunch (dipole oscillation) or an unmatched bunch shape (higher order modes) which were already introduced in Subsec. 3.2.1. The first case can be considered by including the two additional terms

$$x_{\mathrm{B}}(0)\int_{-\infty}^{\infty}f(\omega_{\mathrm{r}})\cos(\omega_{\mathrm{R}}t)\,\mathrm{d}\omega_{\mathrm{r}}\,,$$

$$\dot{x}_\mathrm{B}(0) \int_{-\infty}^{\infty} \frac{f(\omega_\mathrm{r})}{\omega_\mathrm{r}} \sin(\omega_\mathrm{R} t)\, \mathrm{d}\omega_\mathrm{r}$$

in Eq. (3.7) to account for non-vanishing initial conditions [22]. If for example the frequency spread is Gaussian distributed around $\omega_{\mathrm{r}0}$ according to

$$f(\omega_\mathrm{r}) = \frac{1}{\sqrt{2\pi}\sigma_{\omega_\mathrm{r}}} \exp\left\{-\frac{(\omega_\mathrm{r} - \omega_{\mathrm{r}0})^2}{\sigma_{\omega_\mathrm{r}}^2}\right\} ,$$

no external force is present ($A = 0$), and the initial conditions are $x_\mathrm{B}(0) \neq 0$, $\dot{x}_\mathrm{B}(0) = 0$, the barycenter

$$x_\mathrm{B}(t) = \exp\left\{-\frac{1}{2} t^2 \sigma_{\omega_\mathrm{r}}^2\right\} \cos(\omega_{\mathrm{r}0} t)$$

will perform a damped oscillation although the single oscillators are undamped. The resulting center-of-mass displacement x_B of six undamped oscillators with different resonant frequencies is shown in Fig. 3.3. After some time the oscillation amplitude of the barycenter may increase again, i. e. it is not strictly damped. This depends on the frequency spread and the number of oscillators.

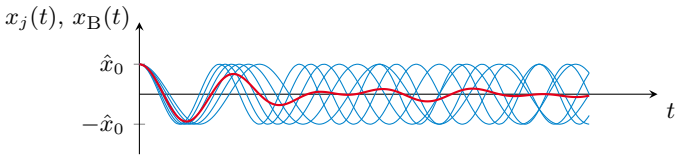

Figure 3.3: Barycenter displacement x_B (red) of a set of oscillators x_j (blue) with different resonance frequencies [42]

This effect is closely related to Landau damping and is accompanied by a *filamentation process* which can also be seen in Fig. 3.3. The sources of Landau damping and damping of rigid bunch oscillation due to filamentation are the same, namely the spread of incoherent frequencies of the single particles. The damping of a rigid bunch oscillation however only depends on the kinematics of the single particles (and thus does not involve any interaction between the particles), which is why it is also called *kinematic decoherence* in literature [76]. Landau damping on the other hand involves a harmonic driving force and a coupling between the particles, e. g. due to coupling impedances (see Chap. 4). Coupling impedances may also affect

kinetic decoherence, but the effect is usually small if the beam is not close to instability. A detailed discussion about the differences and similarities between Landau damping and filamentation due to a rigid displacement can be found e. g. in [76].

Interpreting $x_j(t)$ as the phase $\Delta\varphi$ or local displacement Δz of single particles, the bunch length increases while the particles are redistributed in phase space. Fig. 3.4 shows simulation results of a bunch rigidly displaced by $\varphi_\mathrm{B}(0) = 0.2 \cdot \pi$. The barycenter shown in red comes to rest while the bunch length and maximum energy deviation are increased. The results were obtained with *macro-particle simulations* (see Sec. 3.4) whose parameters are given in Tab. B.1 in the appendix. For the illustration only $N = 2000$ macro-particles and a smaller bunch than listed in Tab. B.1 ($\sigma_\varphi \approx 0.64\,\mathrm{rad}$, $\sigma_{\Delta W} \approx 1.31 \cdot 10^{-19}\,\mathrm{Js}$) were used for sake of a better depiction.

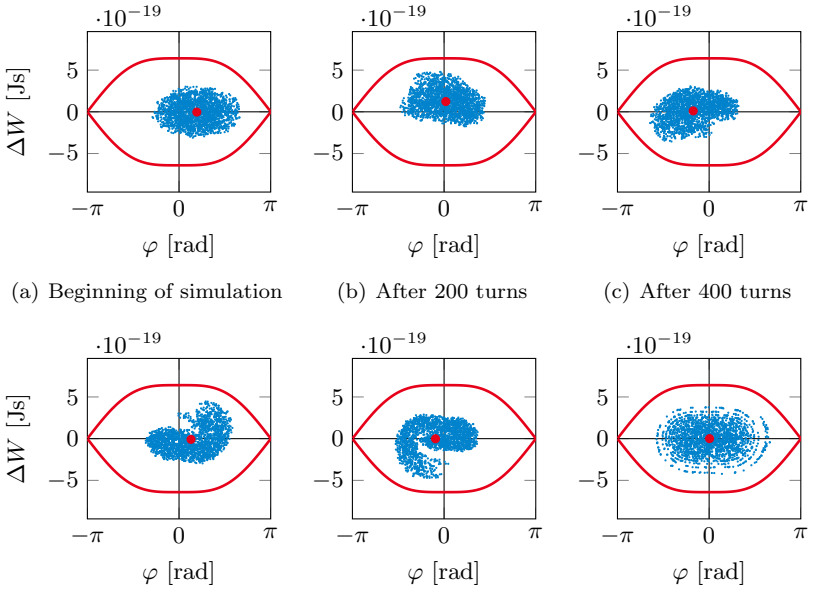

(a) Beginning of simulation (b) After 200 turns (c) After 400 turns

(d) After 800 turns (e) After 1200 turns (f) After 20000 turns

Figure 3.4: Filamentation process of rigidly displaced bunch

3.4 Modeling and Simulation of Coherent Bunch Oscillations

To simulate coherent bunch oscillations, the already mentioned macro-particle simulation [70] is used. For this purpose, the tracking equations (2.6) and (2.13) are implemented for a number of macro-particles, each representing several particles of the bunch. The main advantage of the procedure is that only small numerical issues arise in the calculation of the single-particle trajectories and that its implementation is fast and simple. A major drawback however is the fact that the simulated beam current, if e. g. obtained by the histogram of the particles on the $\Delta\varphi$-axis, is not smooth unless a number of macro-particles in the region of several hundred thousands is used, in which case computation time becomes an issue. A smooth beam current though is necessary for the evaluation of *high intensity effects* like *space-charge* and *wakefields*, see Chap. 4. To overcome this issue, in the simulations presented in this dissertation the beam current is first obtained by allocating interpolating quadratic splines to the particles [13], and second only the first 20 harmonics of the Fourier transformed beam current are used to obtain the voltages resulting from high intensity effects.

To describe the whole bunch with a state space model, central moments for bunched beams in a synchrotron can be used as introduced in [62], where they were successfully applied to single-harmonic buckets. Under certain conditions stated below, central moments fully describe the density function [78] and thus the position and shape of the bunch. Some of the results presented here were already published in [114].

To the distribution $f(x,y)$ the *moment generating function* is defined as

$$F(s_1, s_2,t) = \int_{-\infty}^{\infty}\int_{-\infty}^{\infty} f(x,y,t)\mathrm{e}^{s_1 x+s_2 y}\,\mathrm{d}x\,\mathrm{d}y \tag{3.12}$$

representing a Laplace transform of the distribution. Expanding (3.12) into a series around the origin $(s_1, s_2) = (0,0)$ yields

$$\begin{aligned} F(s_1, s_2,t) &= \int_{-\infty}^{\infty}\int_{-\infty}^{\infty} f(x,y,t)\sum_{n_\mathrm{x}=0}^{\infty}\frac{s_1^{n_\mathrm{x}}x^{n_\mathrm{x}}}{n_\mathrm{x}!}\sum_{n_\mathrm{y}=0}^{\infty}\frac{s_1^{n_\mathrm{y}}y^{n_\mathrm{y}}}{n_\mathrm{y}!}\,\mathrm{d}x\,\mathrm{d}y \\ &= \sum_{n_\mathrm{x}=0}^{\infty}\sum_{n_\mathrm{y}=0}^{\infty}\frac{s_1^{n_\mathrm{x}}}{n_\mathrm{x}!}\frac{s_1^{n_\mathrm{y}}}{n_\mathrm{y}!}\int_{-\infty}^{\infty}\int_{-\infty}^{\infty} x^{n_\mathrm{x}}y^{n_\mathrm{y}}f(x,y,t)\,\mathrm{d}x\,\mathrm{d}y \end{aligned}$$

$$= \sum_{n_\mathrm{x}=0}^{\infty} \sum_{n_\mathrm{y}=0}^{\infty} \frac{s_1^{n_\mathrm{x}}}{n_\mathrm{x}!} \frac{s_1^{n_\mathrm{y}}}{n_\mathrm{y}!} m_{(n_\mathrm{x},n_\mathrm{y})}(t)$$

if the *raw moments*

$$m_{(n_\mathrm{x},n_\mathrm{y})}(t) = \int_{-\infty}^{\infty} \int_{-\infty}^{\infty} x^{n_\mathrm{x}} y^{n_\mathrm{y}} f(x,y,t)\, \mathrm{d}x\, \mathrm{d}y \tag{3.13}$$

are finite and the series converges absolutely near $(s_1, s_2) = (0,0)$. In this case, the derivatives of $F(s_1 = 0, s_2 = 0,t)$ are the raw moments of $f(x,y,t)$ and since $f(x,y,t)$ can be obtained from $F(s_1,s_2,t)$ with a reverse Laplace transform, $f(x,y,t)$ is uniquely determined under the stated conditions if the moments are known [62, 78].

Beside the raw moments $m_{(n_\mathrm{x},n_\mathrm{y})}(t)$ of order $n = n_\mathrm{x} + n_\mathrm{y}$, also *central moments*

$$\mu_{(n_x,n_y)}(t) = \int_{-\infty}^{\infty} \int_{-\infty}^{\infty} (x - m_{(1,0)}(t))^{n_\mathrm{x}} (y - m_{(0,1)}(t))^{n_\mathrm{y}} \cdot f(x,y,t)\, \mathrm{d}x\, \mathrm{d}y \tag{3.14}$$

about the barycenter $(m_{(1,0)}(t),m_{(0,1)}(t))$ with

$$m_{(1,0)}(t) = \int_{-\infty}^{\infty} \int_{-\infty}^{\infty} x \cdot f(x,y,t)\, \mathrm{d}x\, \mathrm{d}y\,,$$

$$m_{(0,1)}(t) = \int_{-\infty}^{\infty} \int_{-\infty}^{\infty} y \cdot f(x,y,t)\, \mathrm{d}x\, \mathrm{d}y\,,$$

can be defined. The central moments on the other hand can be expressed as raw moments (and vice versa) as follows from Eq. (3.13) and (3.14) because

$$\begin{aligned}\mu_{(n_x,n_y)} = &\int_{-\infty}^{\infty} \int_{-\infty}^{\infty} \sum_{k_x=0}^{n_\mathrm{x}} \binom{n_\mathrm{x}}{k_x} x^{n_\mathrm{x}-k_x} (-m_{(1,0)})^{k_x} \\ &\cdot \sum_{k_y=0}^{n_\mathrm{y}} \binom{n_\mathrm{y}}{k_y} y^{n_\mathrm{y}-k_y} (-m_{(0,1)})^{k_y} f(x,y)\, \mathrm{d}x\, \mathrm{d}y \\ = &\sum_{k_x=0}^{n_\mathrm{x}} \sum_{k_y=0}^{n_\mathrm{y}} \binom{n_\mathrm{x}}{k_x} \binom{n_\mathrm{y}}{k_y} m_{(n_\mathrm{x}-k_x,n_\mathrm{y}-k_x)} (-m_{(1,0)})^{k_x} (-m_{(0,1)})^{k_y}\end{aligned}$$

and

$$\begin{aligned} m_{(n_\mathrm{x},n_\mathrm{y})} &= \int_{-\infty}^{\infty}\int_{-\infty}^{\infty} [(x - m_{(1,0)}) + m_{(1,0)}]^{n_\mathrm{x}} \\ &\qquad \cdot [(y - m_{(0,1)}) + m_{(0,1)}]^{n_\mathrm{y}} f(x,y,t)\,\mathrm{d}x\,\mathrm{d}y \\ &= \sum_{k_x=0}^{n_\mathrm{x}} \sum_{k_y=0}^{n_\mathrm{y}} \binom{n_\mathrm{x}}{k_x} \binom{n_\mathrm{y}}{k_y} \mu_{(k_x,k_y)} m_{(1,0)}^{n_\mathrm{x}-k_x} m_{(0,1)}^{n_\mathrm{y}-k_y} , \end{aligned}$$

where the notation of the time dependence has been omitted as will be continued further on. Deriving the equations of motion for the central moments is therefore sufficient to uniquely model the particle bunch. This is simplified if instead of the continuous representation with a particle density function, a discrete representation

$$\begin{aligned} m_{(1,0)} &= \frac{1}{N}\sum_{i=1}^{N} x_i , \\ m_{(0,1)} &= \frac{1}{N}\sum_{i=1}^{N} y_i , \\ \mu_{(n_x,n_y)} &= \frac{1}{N-1}\sum_{i=1}^{N} (x_i - m_{(1,0)})^{n_\mathrm{x}} (y_i - m_{(0,1)})^{n_\mathrm{y}} \end{aligned}$$

is used, where N is the number of particles in the bunch, and x_i and y_i are the coordinates of particle i in phase space.

For $x = \Delta\varphi$ and $y = \Delta W$, the time derivative of the barycenter reads

$$\dot{m}_{(1,0)} = \frac{1}{N}\sum_{i=1}^{N} \Delta\dot{\varphi}_i = \frac{1}{N}\sum_{i=1}^{N} \underbrace{\frac{\omega_\mathrm{RF}^2 \eta_\mathrm{R}}{\beta_\mathrm{R}^2 E_\mathrm{R}}}_{\kappa_1} \Delta W_i = \kappa_1 m_{(0,1)} , \tag{3.15a}$$

$$\begin{aligned} \dot{m}_{(0,1)} &= \frac{1}{N}\sum_{i=1}^{N} \Delta\dot{W}_i \\ &= \frac{1}{N}\sum_{i=1}^{N} \frac{q}{2\pi h}\left(1 + \Delta\hat{V}_\mathrm{u}\right) \\ &\qquad \cdot \Big[\hat{V}_1 \sin(\Delta\varphi_i + \varphi_\mathrm{R} - \Delta\varphi_\mathrm{u}) \end{aligned}$$

$$+\hat{V}_2 \sin(2\Delta\varphi + 2\varphi_\mathrm{R} - 2\Delta\varphi_\mathrm{u} + \psi) - V_\mathrm{R}\Big] \quad (3.15b)$$

of which only (3.15a) can be expressed in terms of other moments because of the sine terms in (3.15b). These have therefore to be replaced by a polynomial, and due to the saddle point in φ_R a Lagrangian polynomial is suitable here instead of e. g. a Taylor approximation. The additional actuating variable ΔV_u used to damp quadrupole oscillations was introduced here to demonstrate in the following, that the dipole and quadrupole mode are decoupled in a linear approximation for a stationary bunch.

Fig. 3.5 shows a Lagrangian polynomial of order eleven for $\varphi_\mathrm{R} = 0$,

$$P(\Delta\varphi) = \left(1 + \Delta\hat{V}_\mathrm{u}\right) \hat{V}_1 \sum_{l=1}^{11} p_l (\Delta\varphi - \Delta\varphi_\mathrm{u})^l \,,$$

which fits very well to the exact voltage

$$\begin{aligned} V(\Delta\varphi) = \left(1 + \Delta\hat{V}_\mathrm{u}\right) & \\ \cdot \Big(\hat{V}_1 \sin(\Delta\varphi + \varphi_\mathrm{R} - \Delta\varphi_\mathrm{u}) & \\ +\hat{V}_2 \sin(2\Delta\varphi + 2\varphi_\mathrm{R} - 2\Delta\varphi_\mathrm{u} + \psi)\Big) \,. & \end{aligned}$$

Both, $\Delta\varphi_\mathrm{u}$ and $\Delta\hat{V}_\mathrm{u}$ were set to zero in Fig. 3.5. The parameters p_l are given in Tab. C.1 in the appendix.

With the polynomial approximation, Eq. (3.15b) reads

$$\begin{aligned} \dot{m}_{(0,1)} &\approx \frac{1}{N} \sum_{i=1}^{N} \underbrace{\frac{q\hat{V}_1}{2\pi h}}_{\kappa_2} \sum_{l=1}^{11} \left(1 + \Delta\hat{V}_\mathrm{u}\right) p_l (\Delta\varphi_i - \Delta\varphi_\mathrm{u})^l \\ &\approx \kappa_2 \left(1 + \Delta\hat{V}_\mathrm{u}\right) \sum_{l=1}^{11} p_l \sum_{k_\mathrm{p}=0}^{l} \binom{l}{k_\mathrm{p}} m_{(l-k_\mathrm{p},0)} (-\Delta\varphi_\mathrm{u})^{k_\mathrm{p}} \\ &= \kappa_2 \left(1 + \Delta\hat{V}_\mathrm{u}\right) \\ &\quad \cdot \sum_{l=1}^{11} p_l \sum_{k_\mathrm{p}=0}^{l} \binom{l}{k_\mathrm{p}} \sum_{k_x=0}^{l-k_\mathrm{p}} \binom{l-k_\mathrm{p}}{k_x} \mu_{(l-k_\mathrm{p},0)} m_{(1,0)}^{l-k_\mathrm{p}} (-\Delta\varphi_\mathrm{u})^{k_\mathrm{p}} \end{aligned} \quad (3.16)$$

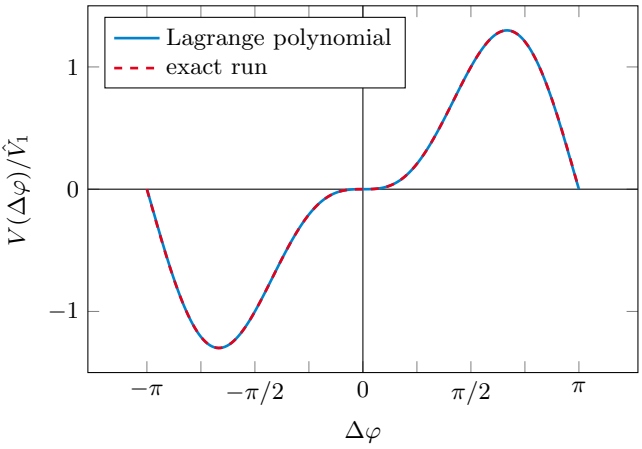

Figure 3.5: Comparison of dual-harmonic voltage and 11th order Lagrangian polynomial for $\varphi_\mathrm{R} = 0$

where the approximation

$$m_{(n_\mathrm{x},n_\mathrm{y})} = \frac{1}{N-1}\sum_{i=1}^{N} x_i^{n_\mathrm{x}} y_i^{n_\mathrm{y}} \approx \frac{1}{N}\sum_{i=1}^{N} x_i^{n_\mathrm{x}} y_i^{n_\mathrm{y}}\ ,\ n_\mathrm{x}+n_\mathrm{y}>1$$

for large N was used. Eq. (3.16) depends on central moments of maximum order $n_\mathrm{x} = 11$. Deriving the time derivative of the second order moments ($n = n_\mathrm{x} + n_\mathrm{y} = 2$) yields equations of motion which depend on moments of maximum order $n = 12$, etc. The modeling scheme therefore yields a model of infinite order which can be reduced by assuming a fixed bunch form and distribution function whereby higher order moments can be expressed in terms of lower order moments [62]. A matched bunch has e. g. a distribution function $f(\mathcal{H}(\Delta\varphi,\Delta W)) = c_1 \exp\left\{-\frac{\mathcal{H}(\Delta\varphi,\Delta W)}{c_2}\right\}$ as stated in Sec. 3.2.1. The integral over $f(\mathcal{H}(\Delta\varphi,\Delta W))$ on the phase space plane is however not analytically solvable which makes it impossible to find analytical expressions for higher order moments. Instead, the parabolic-Gaussian distribution is used as an approximation for a matched bunch. The resulting time derivatives of the first and second order moments are listed in App. C.2. Fig. 3.6 shows the simulation results for the model with the stated approximations. For comparison also the evolution of the central moments obtained by a macro-particle simulation is shown.

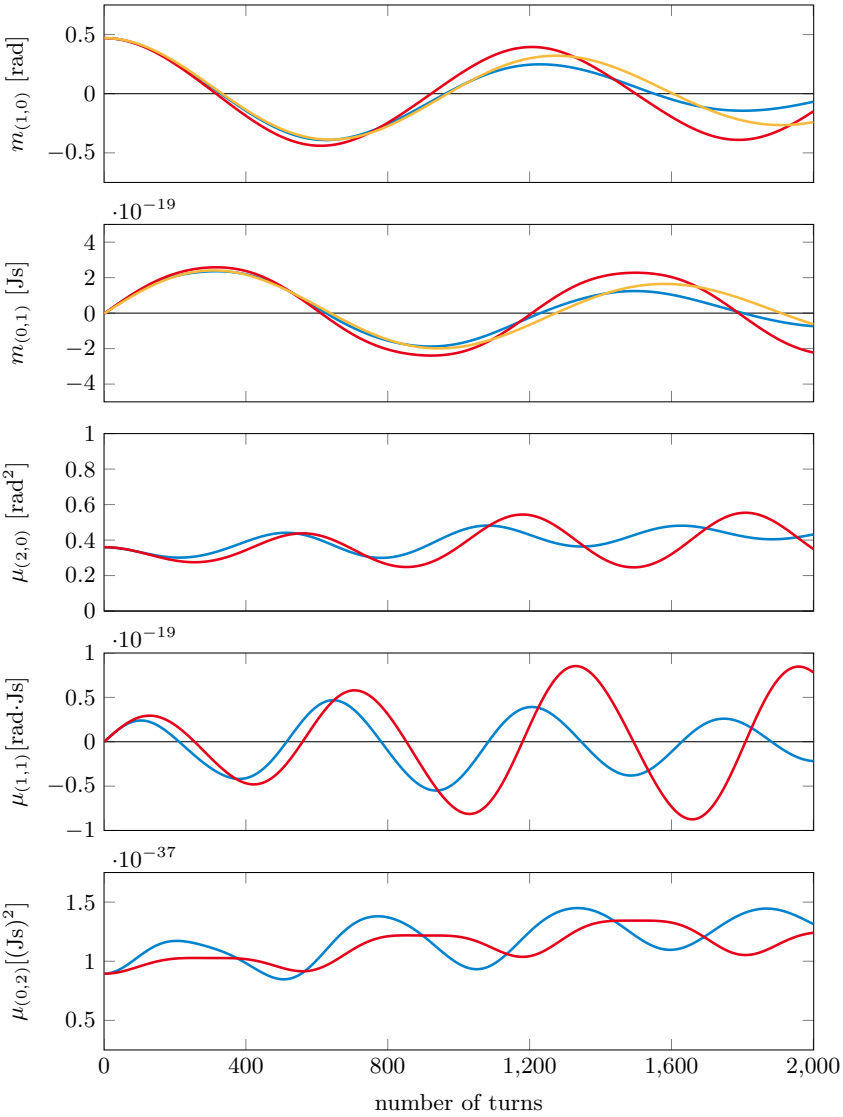

Figure 3.6: Simulation results of a macro-particle simulation (blue), the nonlinear central moments model (Eq. (C.1), red) and the linearized model of dipole oscillation (Eq. (3.18), orange)

The macro-particles were distributed as an originally matched bunch which was shifted by $m_{(1,0)}(t=0) = 0.15\pi$.

The central moments model reproduces the coherent synchrotron frequency with only small deviations, but does not reflect Landau damping. The moments of second order are modeled less accurately, as expected, because they depend stronger than the first order moments on higher order moments which were set to zero due to the assumption of a parabolic-Gaussian distributed bunch.

Linearizing the model around a working point

$$\begin{aligned} &\bar{m}_{(1,0)} = 0\,, \quad \bar{m}_{(0,1)} = 0\,, \\ &\bar{\mu}_{(2,0)} \neq 0\,, \quad \bar{\mu}_{(1,1)} = 0\,, \quad \bar{\mu}_{(0,2)} \neq 0 \end{aligned}$$

yields

$$\begin{bmatrix} \Delta\dot{m}_{(1,0)} \\ \Delta\dot{m}_{(0,1)} \\ \Delta\dot{\mu}_{(2,0)} \\ \Delta\dot{\mu}_{(1,1)} \\ \Delta\dot{\mu}_{(0,2)} \end{bmatrix} = \begin{bmatrix} 0 & \kappa_1 & 0 & 0 & 0 \\ \kappa_2 a_1 & 0 & 0 & 0 & 0 \\ 0 & 0 & 0 & 2\kappa_1 & 0 \\ 0 & 0 & \kappa_2 a_2 & 0 & \kappa_1 \\ 0 & 0 & 0 & 2\kappa_2 p_1 & 0 \end{bmatrix} \begin{bmatrix} \Delta m_{(1,0)} \\ \Delta m_{(0,1)} \\ \Delta\mu_{(2,0)} \\ \Delta\mu_{(1,1)} \\ \Delta\mu_{(0,2)} \end{bmatrix} + \begin{bmatrix} 0 & 0 \\ \kappa_2 b_1 & 0 \\ 0 & 0 \\ 0 & \kappa_2 b_2 \\ 0 & 0 \end{bmatrix} \begin{bmatrix} \Delta\varphi_\mathrm{u} \\ \Delta\hat{V}_\mathrm{u} \end{bmatrix} \tag{3.17}$$

with

$$\begin{aligned} a_1 &= p_1 + 3p_3\bar{\mu}_{(2,0)} + \frac{75}{7}p_5\bar{\mu}^2_{(2,0)} \\ &\quad + \frac{125}{3}p_7\bar{\mu}^3_{(2,0)} + \frac{1875}{11}p_9\bar{\mu}^4_{(2,0)} + \frac{9375}{13}p_{11}\bar{\mu}^5_{(2,0)}\,, \\ a_2 &= p_1 + \frac{30}{7}p_3\bar{\mu}_{(2,0)} + \frac{125}{7}p_5\bar{\mu}^2_{(2,0)} \\ &\quad + \frac{2500}{33}p_7\bar{\mu}^3_{(2,0)} + \frac{46875}{143}p_9\bar{\mu}^4_{(2,0)} + \frac{18750}{13}p_{11}\bar{\mu}^5_{(2,0)}\,, \\ b_1 &= -a_1\,, \\ b_2 &= p_1\bar{\mu}_{(2,0)} + \frac{15}{7}p_3\bar{\mu}^2_{(2,0)} + \frac{125}{21}p_5\bar{\mu}^3_{(2,0)} \\ &\quad + \frac{625}{33}p_7\bar{\mu}^4_{(2,0)} + \frac{9375}{143}p_9\bar{\mu}^5_{(2,0)} + \frac{3125}{13}p_{11}\bar{\mu}^6_{(2,0)}\,, \end{aligned}$$

consisting of two decoupled systems, one describing the dipole and one describing the quadrupole oscillation.

So far a bunch distribution with elliptical contour lines was assumed and the fact that the bunch shape changes was neglected when expressing higher order moments in terms of first and second order moments. The model thus only represents dipole and quadrupole oscillations. In order to also model higher oscillation modes, a more sophisticated bunch distribution function has to be assumed. This is discussed in detail in [62] for a single-harmonic cavity system, but as the dissertation at hand focuses on the damping of dipole oscillations in a dual-harmonic cavity setting, the modeling of higher modes is not necessary in this context. In fact, for the controller design the linearized model proves to be sufficient, eventually extended with an additional damping term to account for filamentation effects.

It is again stressed that the model derived here is only valid for a stationary bunch, i. e. if no acceleration is present and $V_\mathrm{R} = 0$. For $V_\mathrm{R} \neq 0$ the resulting voltage has a saddle point at $\varphi_\mathrm{R} \neq 0$ and thus a different shape. In this case not only the parameters p_l change, but also the distribution function of a matched bunch has no longer contour lines which resemble ellipses. Depending on the value of V_R eventually a more complex distribution function has to be assumed in order to limit the order of the model.

The linearized model (3.17) of the first and second order central moments consists of two decoupled systems. The one representing dipole oscillations in a stationary bucket reads

$$\begin{bmatrix} \Delta\dot{m}_{(1,0)} \\ \Delta\dot{m}_{(0,1)} \end{bmatrix} = \begin{bmatrix} 0 & \kappa_1 \\ \kappa_2 a_1 & 0 \end{bmatrix} \begin{bmatrix} \Delta m_{(1,0)} \\ \Delta m_{(0,1)} \end{bmatrix} + \begin{bmatrix} 0 \\ -\kappa_2 a_1 \end{bmatrix} \Delta\varphi_\mathrm{u} \,.$$

Below transition, $\kappa_1 < 0$ and $\kappa_2 a_1 > 0$ hold, while above transition the signs are switched. This represents an undamped harmonic oscillator which can be extended by a linear damping term d_coh and expressed in terms of the coherent synchrotron frequency according to

$$\begin{bmatrix} \Delta\dot{m}_{(1,0)} \\ \Delta\dot{m}_{(0,1)} \end{bmatrix} = \begin{bmatrix} 0 & \kappa_1 \\ -\frac{\omega_{\mathrm{syn,coh}}^2}{\kappa_1} & -2d_\mathrm{coh} \end{bmatrix} \begin{bmatrix} \Delta m_{(1,0)} \\ \Delta m_{(0,1)} \end{bmatrix} + \begin{bmatrix} 0 \\ \frac{\omega_{\mathrm{syn,coh}}^2}{\kappa_1} \end{bmatrix} \Delta\varphi_\mathrm{u} \,, \quad (3.18)$$

resulting in the well-known equation of motion of a damped harmonic oscillator

$$\Delta\ddot{m}_{(1,0)} + 2d_\mathrm{coh}\Delta\dot{m}_{(1,0)} + \omega_{\mathrm{syn,coh}}^2 \Delta m_{(1,0)} = \omega_{\mathrm{syn,coh}}^2 \Delta\varphi_\mathrm{u} \,.$$

Note that this also establishes a third method to obtain the coherent synchrotron frequency in addition to the methods discussed in section 3.2.3.

Eq. (3.18) offers the possibility of an easy controller design which however has to be robust against model uncertainties due to the linearization, and the fact that the coherent synchrotron frequency depends on the bunch length which eventually has to be estimated.

3.5 Discussion

In this dissertation, macro-particle simulations are performed, combined with a spline interpolation to obtain a smoother beam current. Furthermore, only the first 20 harmonics of the beam current are used to calculate the voltages resulting from high intensity effects (cf. Chap. 4).

For modeling purposes, the central moments modeling scheme introduced in [62] for bunched beams in a synchrotron with a single-harmonic cavity system is also transferable to the dual-harmonic case. If a distribution function with (fixed) elliptic contour lines is assumed, only the first and second oscillation modes can be covered by the model. This is however sufficient for the goals of this dissertation which is only concerned with damping of the rigid dipole mode.

The central moments model can be linearized around a working point yielding a harmonic oscillator. This simplified model will be used in Chap. 5 for the controller design.

4 High Intensity Effects

So far only external forces on the particles supplied by the cavities and the magnets were considered. Depending on the beam current, however, also self forces are present, mainly space charge, wall impedance and resonator effects like beam loading in the cavities.

Space charge effects are determined by the repulsing force the charged particles exert on each other. They are strongest at low energies and decrease for highly relativistic beams [22, 88]. Space charge has a defocusing effect on the bunch below transition energy and focuses the bunch above transition energy.

In cavity-like surroundings the particles induce fields acting back on a succeeding bunch or the same one in a later turn. The field strength in these resonators depends on the beam current and the resonance frequency of the machine parts. The driven frequency also determines whether the wall impedances lead to instabilities by driving coherent bunch oscillations or whether they provide additional damping [87]. In addition the vacuum pipe has only a finite conductivity. The bunch induces so called *mirror currents* in the wall which are affected by the wall resistance. The mirror currents on the other hand act back on the beam.

The electrical fields originating e. g. from space charge can either be expressed in the time domain where they depend on the derivative of the particle line density respectively the beam current [1] [15, 22, 87, 88]. Alternatively fields are often considered in the frequency domain by multiplying the transformed beam current and a complex longitudinal coupling impedance [6, 8, 22, 101]. The latter method is appealing because the coupling impedance describes the physical behavior of the surroundings in an easy fashion. It is therefore possible to add the impedances of different machine parts like the cavities or the resistive walls as well as the space charge impedance [8]. Transient effects are however neglected. In this chapter, the impedances of longitudinal space charge, broad-band- and narrow-band-resonators and resistive walls are considered and differences

[1] This is only valid for a "smooth" beam current, i. e. only if higher frequency components of its spectrum have negligibly small amplitudes.

in literature especially in the treatment of space charge and resistive walls are discussed.

The chapter is structured as follows: Sec. 4.1 considers space charge effects, followed by the treatment of resistive wall and resonator impedances in Sec. 4.2. The chapter ends with a brief discussion about stability issues in Sec. 4.3.

4.1 Space Charge Effects

For the derivation of the space charge impedance the bunch in the beam pipe is usually assumed to perform no oscillations in transverse direction, i. e. it is located on the reference orbit as depicted in Fig. 4.1 [76, 87]. Furthermore, the bunches are assumed to be long and smooth in the sense that the distance over which the longitudinal distribution changes perceptibly is long [22]. The round and homogenous beam has a cross section with radius a which may be a function of the longitudinal coordinate z but not of the azimuthal θ, while the constant cylindrical beam pipe radius is denoted by b. Furthermore the beam is rigid and its longitudinal extent is much bigger than the transverse one.

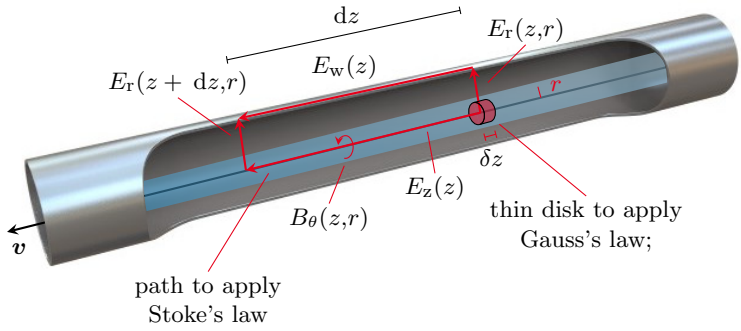

Figure 4.1: Electrical fields induced by the beam

The radial electric field component $E_r(z,r)$ at the longitudinal location z and the transverse distance r from the center of the pipe is given by Gauss's law, applied to a thin disk with radius r and thickness δz perpendicular to the longitudinal axis. The electric flux for a disk of radius $r > a$ is given

by

$$\Phi_{el} = \iint\limits_A \boldsymbol{E}\,\mathrm{d}\boldsymbol{A} = E_\mathrm{r}(z,r,t)\cdot 2\pi r\delta z = \frac{q\lambda(z,t)\delta z}{\epsilon_0}\,,$$

where $\lambda(z,t) = \lambda(z-\beta_\mathrm{R}ct)$ is the longitudinal line density of the rigid beam, normalized to

$$\int \lambda(z,t)\,\mathrm{d}z = N$$

with N being the total number of particles in one bunch. For $r \leq a$, the electric flux is given by

$$\Phi_{el} = E_\mathrm{r}(z,r,t)\cdot 2\pi r\delta z = \frac{q\lambda(z,t)\delta z}{\epsilon_0}\frac{\pi r^2}{\pi a^2}\,,$$

assuming a homogenous cross section. The radial electrical field therefore reads

$$E_\mathrm{r}(z,r,t) = \begin{cases} \frac{q\lambda(z,t)}{2\pi\epsilon_0}\frac{r}{a^2} & r \leq a\,, \\ \frac{q\lambda(z,t)}{2\pi\epsilon_0}\frac{1}{r} & r > a\,. \end{cases}$$

The longitudinal and the radial magnetic fields vanish, while the azimuthal magnetic field is given by Ampère's circuital law,

$$\oint\limits_C \boldsymbol{B}\,\mathrm{d}\boldsymbol{l} = \iint\limits_A \mu_0\boldsymbol{J}\,\mathrm{d}\boldsymbol{A} \tag{4.1}$$

where $\boldsymbol{J}$ is the current density passing through the area A enclosed by the curve C, resulting in

$$B_\theta(z,r,t) = \begin{cases} \frac{\mu_0 q\lambda(z,t)\beta_\mathrm{R}c}{2\pi}\frac{r}{a^2} & r \leq a\,, \\ \frac{\mu_0 q\lambda(z,t)\beta_\mathrm{R}c}{2\pi}\frac{1}{r} & r > a\,. \end{cases}$$

Note that in Eq. (4.1) the displacement current induced by $\frac{\partial E_z}{\partial t}$ was neglected. This is valid under the assumption that the displacement current is small compared to the current induced by the particle beam and holds for the smooth and long beam assumed for the derivation. Applying now Stoke's law

$$\oint\limits_C \boldsymbol{E}\,\mathrm{d}\boldsymbol{l} = -\frac{\mathrm{d}}{\mathrm{d}t}\int\limits_S \boldsymbol{B}\,\mathrm{d}\boldsymbol{S}$$

to the electrical fields along the path shown in Fig. 4.1 with small $\mathrm{d}z$ yields

$$E_\mathrm{z}(z,t)\,\mathrm{d}z + \int_0^b E_\mathrm{r}(z+\mathrm{d}z,r,t)\,\mathrm{d}r - E_\mathrm{w}(z,t)\,\mathrm{d}z + \int_b^0 E_\mathrm{r}(z,r,t)\,\mathrm{d}r = -\frac{\partial}{\partial t}\int_0^b B_\theta(z,r,t)\,\mathrm{d}r\cdot\,\mathrm{d}z\,.$$

The left side is simplified by assuming $E_\mathrm{r}(z+\mathrm{d}z,r,t) \approx E_\mathrm{r}(z,r,t) + \frac{\partial E_\mathrm{r}}{\partial z}\big|_z\,\mathrm{d}z$, resulting in

$$\begin{aligned} E_\mathrm{z}(z,t)\,\mathrm{d}z + \frac{q}{4\pi\epsilon_0}\frac{\partial\lambda(z,t)}{\partial z}\left(1+2\ln\left(\frac{b}{a}\right)\right)\mathrm{d}z - E_\mathrm{w}(z,t)\,\mathrm{d}z \\ = \frac{\mu_0 q\beta_\mathrm{R}^2 c^2}{4\pi}\frac{\partial\lambda(z,t)}{\partial z}\left(1+2\ln\left(\frac{b}{a}\right)\right)\mathrm{d}z \\ \Rightarrow E_\mathrm{z}(z,t) - E_\mathrm{w}(z,t) = -\frac{qg_0}{4\pi\epsilon_0}(1-\beta_\mathrm{R}^2)\frac{\partial\lambda(z,t)}{\partial z} \\ \Rightarrow E_\mathrm{z}(z,t) = -\frac{qg_0}{4\pi\epsilon_0\gamma_\mathrm{R}^2}\frac{\partial\lambda(z,t)}{\partial z} + E_\mathrm{w}(z,t)\,, \end{aligned} \tag{4.2}$$

for the longitudinal space charge field on the z-axis. Here, $\frac{\partial\lambda(z-\beta_\mathrm{R}ct)}{\partial t} = -\beta_\mathrm{R}c\frac{\partial\lambda(z-\beta_\mathrm{R}ct)}{\partial z}$ was used and $g_0 = 1+2\ln\left(\frac{b}{a}\right)$ is the *geometry factor*.

The first term of the right hand side of Eq. (4.2) corresponds to the space charge effect. It induces an additional voltage

$$V_\mathrm{sc}(\Delta z) = (E_\mathrm{z}(\Delta z) - E_\mathrm{w}(\Delta z))\cdot 2\pi R$$

per turn in the synchrotron, acting on the beam at location $\Delta z = z - z_\mathrm{R}$. Assuming a uniformly distributed coasting beam with small fluctuations [61],

$$\lambda(z,t) = \lambda_0 + \lambda_n e^{jn(\beta_\mathrm{R}ct-z)/R}$$

with the harmonic $n = \frac{\omega}{\omega_\mathrm{R}}$ and the corresponding beam current $I_n = q\beta_\mathrm{R}c\lambda_n$, the space charge voltage can be expressed as [61, 98]

$$\begin{aligned} V_\mathrm{sc} &= j\frac{2\pi q g_0 n R}{4\pi\epsilon_0\gamma_\mathrm{R}^2 R}\lambda_n e^{jn(\beta_\mathrm{R}ct-z)/R} = j\frac{g_0 n}{2\beta_\mathrm{R}\gamma_\mathrm{R}^2\epsilon_0 c}q\beta_\mathrm{R}c\lambda_n e^{jn(\beta_\mathrm{R}ct-z)/R} \\ &= j\frac{n g_0 Z_0}{2\beta_\mathrm{R}\gamma_\mathrm{R}^2} I_n e^{jn(\beta_\mathrm{R}ct-z)/R} = -Z_\mathrm{sc} I_n e^{jn(\beta_\mathrm{R}ct-z)/R} \end{aligned} \tag{4.3}$$

with the *space charge impedance* [2]

$$Z_{\mathrm{sc}}(n) = -j\frac{ng_0 Z_0}{2\beta_{\mathrm{R}}\gamma_{\mathrm{R}}^2} \tag{4.4}$$

and the so-called *free space impedance* $Z_0 = \frac{1}{\epsilon_0 c} \approx 376.7\,\Omega$. The minus sign in the definition of the space charge impedance in Eq. (4.3) indicates that the voltage is understood as a voltage drop per unit current [61].

Eq. (4.4) gives the space charge impedance if the electric field only on the z-axis is considered, without averaging over the electrical field at different radii $r < a$. There exist various extensions and alternations to Eq. (4.4), yielding alternative geometry factors g. The expressions found in literature usually read $g = \alpha + 2\ln(b/a)$, where $\alpha \in [0,1]$, cf. [97], but are also extended sometimes to be frequency dependent.

Al-katheeb et al. [6] obtained e. g. a formula for the space charge impedance by averaging over a uniform transverse beam distribution. They suggest to use the geometry factor

$$g = \left(\frac{1}{2} + 2\ln\left(\frac{b}{a}\right)\right)\frac{1}{1+\left(\frac{n}{n_{\mathrm{c}}}\right)^2},$$

decreasing strongly at the cutoff frequency $\omega_{\mathrm{c}} = n_{\mathrm{c}}\omega_{\mathrm{R}}$, which is used in the simulations carried out in this dissertation. A similar expression is presented e. g. in [45].

Wang et al. [97] obtain the geometry factor

$$g = 2\ln\left(\frac{b}{a}\right)$$

as an average value for changing beam diameters in an experimental setting.

According to [55] a beam with a constant transverse density but with an elliptical cross section of major/minor semi-axes a_1 and a_2 in a pipe with elliptical cross section of major/minor semi-axes b_1 and b_2 features an on-axis geometry factor

$$g = 2\ln\left(\frac{b_1+b_2}{a_1+a_2}\right) + \frac{2b_1b_2}{b_1^2+b_2^2}.$$

[2] The sign of Z_{sc} is not consistent in literature and depends on the definition of the beam perturbation, cf. [22, 76].

All mentioned references have in common that the pipe and the beam are considered to have a certain (usually) constant geometry. Furthermore, any analytical derivation of beam impedances is subject to various assumptions and averaging. In the context of controller design, space charge effects as well as wall impedances are therefore considered to be disturbances which are not explicitly considered in the controller design process. Nevertheless, the controllers have to be robust enough to remain stable under any occurring disturbance. The extensive treatment of space charge and wall impedance effects is not within the scope of this dissertation, but instead a rough model of high-intensity effects is considered in the beam simulations as an example of possible disturbances and to demonstrate robustness of the controllers.

4.2 Wall Impedances and Resonators

In the derivation of Eq. (4.4) from Eq. (4.2), the electric field in the vacuum pipe was neglected, assuming a perfectly conducting material. Due to a finite conductivity however, fields emitted by the beam can penetrate the wall and cause the beam to lose energy. Furthermore, several components of the synchrotron act as resonators, e. g. the cavities, kicker magnets or changing cross sections of the beam pipe. When the beam passes these resonators, electromagnetic fields are induced which act back on the inducing bunch (possibly in later turns) or on successive bunches. This effect can again be treated as impedances Z_{rw} of a resistive wall and Z_{res} of a resonant component resulting in induced and total voltage [8]

$$\begin{aligned} V_{\mathrm{ind}} &= -I \left(Z_{\mathrm{sc}} + Z_{\mathrm{rw}} + \sum Z_{\mathrm{res}} \right) , \\ V_{\mathrm{tot}} &= V_{\mathrm{RF}} + V_{\mathrm{ind}} . \end{aligned} \tag{4.5}$$

As well as for space-charge effects, also for wall impedances several expressions can be found in literature depending on which effects are taken into account, e. g. whether the beam is considered to be non-relativistic or ultra-relativistic (i. e. $\gamma \gg 1$). This section, like the previous one, attempts to give some examples of different approaches, keeping in mind that wall impedances are also disturbances from a control engineering point of view. They are therefore not considered explicitly in the controller design process, but again the controllers have to be robust against any occurring disturbances.

In literature usually the expression

$$\frac{Z_{\mathrm{rw}}(n)}{n} = (1 + j \cdot \mathrm{sgn}(n)) \frac{Z_0 \beta_{\mathrm{R}} \delta_{\mathrm{s}}(\omega_{\mathrm{R}})}{2\sqrt{|n|b}} \tag{4.6}$$

for the resistive wall impedance of a cylindrical pipe can be found which holds for an ultra-relativistic beam [59, 61]. It depends on the *skin depth* $\delta_{\mathrm{s}}(\omega) = \sqrt{\frac{2}{\mu_0 \sigma_{\mathrm{w}} \omega}}$ with the conductivity σ_{w} at revolution frequency with the approximation $\mu_r \approx 1$ [3]. The real part is due to the electric, and the imaginary part due to the magnetic field acting on the beam.

The authors of [6] suggest the expression

$$\frac{Z_{\mathrm{rw}}(n)}{n} = (1 + j \cdot \mathrm{sgn}(n)) \frac{Z_0 \beta_{\mathrm{R}} \delta_{\mathrm{s}}(\omega_{\mathrm{R}})}{2\sqrt{|n|b}} \frac{4 I_1^2(\sigma a)}{\sigma^2 a^2 I_0^2(\sigma a)} \tag{4.7}$$

to describe the resistive wall also for lower beam energies which is used in the simulations presented here. Here, $\sigma = \frac{\omega}{\beta_{\mathrm{R}} c \gamma_{\mathrm{R}}}$ [4] was introduced and I_ν, $\nu \in \{0,1\}$ is the modified Bessel function of first kind. For ultra-relativistic beams $\sigma \to 0$ holds, and Eq. (4.7) reduces to (4.6).

Cavity-like objects in the ring like the accelerating cavities, but also e. g. kicker magnets are resonators which act back on the beam via a coupling impedance. In addition, also changes in the geometry or the cross section of the vacuum chamber act as resonators. Modeling the structure as a simple RLC-circuit yields the resonator impedance [8, 14, 61, 76]

$$Z_{\mathrm{res}}(\omega) = \frac{R_{\mathrm{s}}}{1 + jQ\left(\frac{\omega}{\omega_{\mathrm{res}}} - \frac{\omega_{\mathrm{res}}}{\omega}\right)},$$

where the shunt resistance R_{s}, the quality factor Q, and the resonance frequency ω_{res} depend on the machine part under consideration. For the cavities they also depend on the voltage amplitude and radio frequency [38]. Values for the broadband resonators due to discontinuities in the vacuum pipe can be found e. g. in [8].

The cavity impedance is linked to *beam loading* which describes the perturbation of the cavity voltage by the beam. While all voltages induced by high intensity effects are added to the RF voltage (cf. Eq. (4.5)), no matter at which location they occur, the fields induced by beam loading

[3] The vacuum pipe is usually non-magnetic [103].

[4] Not to be confused with the conductivity σ_{w}.

are located in the cavity gap. They may therefore be measured and counteracted by a possibly existing inner feedback loop for the cavity phase and amplitude (cf. [38] for the cavity feedback of SIS18). However, beam loading may also disturb the inner control loops by de-tuning the cavities. Nevertheless, as the inner control loops are not within the scope of this dissertation, they are not considered in the simulations.

The resonator induced voltages acting on the beam evaluated in one iteration step in the simulations are used in the subsequent one as initial values.

Fields induced by a bunch interacting with its environment are not necessarily completely decayed when a following bunch or the same one in a later turn arrives at the location under consideration. This gives rise to coupled-bunch oscillations (cf. Sec. 3.1) which are not within the scope of this dissertation. Instead the bunches are assumed to oscillate coherently, which was also the case in the beam experiments presented in Chap. 6. Wall impedances are therefore considered in simulations as if there was only one bunch in the synchrotron within a bucket of length L_R/h but with a revolution frequency of $h\omega_\mathrm{R}$, similar to [56].

4.3 Discussion

A lot of research is concerned with the stability issues in synchrotrons caused by space charge and wall impedances. In a coasting beam, space charge can cause self-bunching if the beam energy is above transition. In this case, any occurring humps are growing due to the focusing effect of the space charge and the coasting beam is unstable. Below transition, however, space charge has a defocusing effect and humps in a coasting beam vanish after some time. Thus the beam is stable. A bunched beam is also focused/defocused above/below transition. In addition, the altered total voltage $V_\mathrm{tot} = V_\mathrm{RF} + V_\mathrm{ind}$ leads to a change of the incoherent synchrotron frequency spectrum. The author of [76] states, that also a coherent synchrotron frequency shift of the dipole oscillation occurs under the condition that there is an incoherent frequency spread and the beam intensity is not weak. This is usually neglected in literature and it is assumed that the coherent synchrotron frequency of the dipole oscillation does not shift, resulting in a loss of coherent damping if the incoherent synchrotron frequency spectrum is shifted away from the coherent synchrotron frequency.

Resistive wall impedances lead to an energy loss of the beam. This may drive dipole oscillations as the bunches get out of synchronization with the

RF cavity voltage.

However, the detailed investigation of stability issues is beyond the scope of this dissertation. Deviations of the total voltage from the ideal RF voltage due to high intensity effects are treated as unknown disturbances which drive instabilities and/or change model parameters like the damping rate of the dipole oscillation due to filamentation. They are therefore included in the simulations but not in the modeling process discussed in Sec. 3.4. The simulated beam intensities are furthermore comparatively low and bunch oscillations are instead introduced artificially by a phase kick applied to the bunches. This is done first to investigate the controller results by means of a pre-defined and known disturbance, and second to enable comparison to the beam experiments presented in Chap. 6 which were also performed with low intensities (cf. Tab. B.4 and Tab. B.5).

5 Controller Design

In Chap. 3 coherent bunch oscillations were described which can be driven by several sources. Although coherent effects provide a natural damping (cf. Sec. 3.3), recurring disturbances such as high intensity effects may exceed damping effects, leading to particle loss. Furthermore, the beam emittance is blown up, decreasing the beam quality. If the bunch becomes too long due to filamentation, particles may also leave the bucket during the acceleration cycle as the bucket length decreases, although the bucket area is usually kept constant by adjusting the voltage amplitudes (cf. Subsec. 2.3.1).

Therefore feedback systems are used to provide additional damping of the various bunch oscillations of which the most common one is the dipole mode. Usually the accelerating cavities are used to damp bunch oscillations where the phase of the voltage acts as an actuating variable that damps oscillations of odd mode (dipole, sextupole, etc.), and the voltage amplitude can be used to damp oscillations of even mode (quadrupole, octupole, etc.) [63]. Alternatively, separate kicker cavities can be installed to provide an energy change to the particles of the bunches which can also damp dipole oscillations [34]. This energy change only serves the purpose of beam stabilization and is not to be confused with a change of the reference beam energy E_R.

The dissertation at hand only treats damping of dipole oscillations which is accomplished by shifting the total cavity voltage in phase, maintaining its shape. Neither the phase shift between the first and second harmonic cavity nor their amplitudes are changed by the presented phase feedback systems.

After an overview on previous developments in Sec. 5.1, the feedback loop used in SIS18 is depicted in Sec. 5.2. Currently, a *finite impulse response (FIR)* filter is used for SIS18 operating in single-harmonic cavity mode [52], which can be transferred to the dual-harmonic mode as presented in Sec. 5.3 along with possible alternative filter structures. Using the model of a harmonic oscillator as derived in Sec. 3.4, also an output feedback controller can be designed which is discussed in Sec. 5.4. The output feedback results in an FIR filter with a short filter length which

in contrast to the filters presented in Sec. 5.3 is obtained by pole placement for the closed-loop system. By means of linear matrix inequalities (LMIs) the controller can be optimized for robustness against parameter uncertainties. As a simple model for the dipole oscillation is known, also a state feedback along with an observer can be designed as demonstrated in Sec. 5.5. The controller and observer are again optimized concerning robustness against parameter uncertainties. Simulation results including high intensity effects as discussed in Chap. 4 are presented for the different controller designs. The chapter ends with a discussion in Sec. 5.6.

5.1 Previous Developments

This section intends to give a brief overview on previous developments of phase feedback loops, but rather by presenting selected publications giving an idea of the different approaches instead of delivering an exhaustive summary of literature. Two main approaches can be distinguished concerning the feedback design process:

1. Impedance-based: Feeding back the filtered beam signal to the RF-signal driving the cavities changes their impedance. This is used to damp sidebands of the beam spectrum.

2. Model-based: The phase and/or magnitude of the first harmonic of the beam signal is determined and fed back to change the phase and/or amplitude of the cavity voltage.

Both approaches result in a phase shift of the cavity voltage to damp dipole oscillation.

In the seventies of the 20th century, Kriegbaum, Pedersen and Sacherer already presented an active damping system for the CERN PS Booster in [57, 80]. It feeds back the filtered signal from a longitudinal pick-up unit to the RF-signal driving the cavity in order to change the cavity impedance.

A very fundamental disquisition on the damping of dipole and quadrupole oscillations is given by Boussard in [16], decomposing the problem of damping the dipole oscillation into two parts, namely a phase loop to suppress oscillations and a radial loop to correct the radial beam position. This corresponds to a state feedback as the radius is related to a frequency or energy deviation of the beam. He also states that damping of dipole oscillations is achieved by shifting the phase deviation signal by 90° which can be accomplished e. g. by a differentiator (which is according to [16] limited in its gain due to noise and a possible coupling with

quadrupole modes if the beam signal is not filtered) or by an integrator (which is also limited in its gain to obtain closed loop stability and does not reject static offsets).

Based on [16], phase and radial feedback loops for the Brookhaven AGS Booster were analyzed by Zhang and Weng in [100] by means of a linearized beam model, using P- and I-elements for the control laws. The work only considers analytic calculations and simulations, but no measurement results are presented. These are however given in [19] by Brennan using a PID-structure in the phase loop. A similar approach is realized for the Brookhaven RHIC in terms of a state-variable feedback [20].

Tan and Steimel [93] presented a bunch by bunch damping system for the Tevatron [1] at Fermilab consisting of a notch filter to suppress the revolution harmonics of the beam signal and to differentiate the synchrotron sidebands around revolution harmonics. Depending on the derivatives, a phase kick was applied to the cavities.

Kuo et al. [58] describe a feedback consisting of finite impulse response (FIR) bandpass filters for bunch-by-bunch feedback by means of a longitudinal kicker in the Taiwan Light Source [2].

At GSI currently the phase difference between the beam signal, obtained by a *fast current transformer* (FCT) or a *beam position monitor* (BPM) [40, 50], and the RF signal driving the cavities is fed back via an FIR filter. The filter output serves as a frequency change $\Delta\omega_{\mathrm{gap}}$ in the cavities resulting in a phase shift $\Delta\varphi_{\mathrm{u}} = \int \Delta\omega_{\mathrm{gap}}\,\mathrm{d}t$ of the gap voltage [52]. The filter has the advantage that it suppresses unavoidable measurement offsets due to its multi-passband characteristic.

The results presented in the mentioned literature are not necessarily comparable to the results in this dissertation in the sense that they are obtained for different synchrotrons with in general different conditions, requirements and sometimes available sensors. None of the literature is however concerned with the damping of dipole oscillations in a dual-harmonic cavity setting in bunch lengthening mode. In addition, the modeling approach used here is usually replaced by a one-particle model. An exception is e. g. [62].

5.2 Control Loop

The principal scheme of the phase feedback system is depicted in Fig. 5.1.

[1] The Tevatron was shut down on September 29th, 2011 [2].
[2] No heavy-ion synchrotron, but an electron synchrotron.

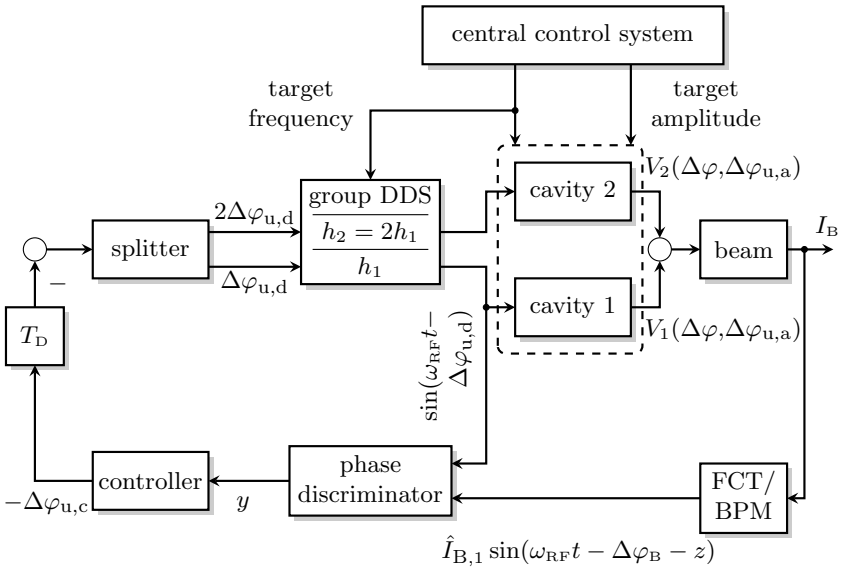

Figure 5.1: Principal scheme of the beam phase control loop for dual-harmonic cavity mode at GSI

The bunches are monitored either by a fast current transformer (FCT) or a beam position monitor (BPM). Both provide a measurement of the beam current $I_B(t)$. This signal is compared to a reference signal, usually the signal supplied by the first-harmonic group *direct digital synthesizer* (DDS), indicated by h_1 in Fig. 5.1. The group DDS of each cavity acts as a reference for the cavity *Digital Signal Processor* (DSP) which regulates the internal cavity DDS. The internal cavity DDS on the other hand drives the cavity voltage. Both components, the cavity DSP and the cavity DDS are not shown in the block diagram.

A phase discriminator determines the phase shift between the signals, yielding the measured output

$$y = \Delta\varphi_B - \Delta\varphi_{u,d} + z\,, \tag{5.1}$$

referring the bunch barycenter phase to the desired actuating variable $\Delta\varphi_{u,d}$. A measurement offset z may occur. For sake of simplicity, Fig. 5.1 shows only the first harmonic of the beam signal with amplitude $\hat{I}_{B,1}$ as the output of the FCT which in reality also delivers the higher harmonic

components. Therefore an analog preprocessing takes place in the phase discriminator which is not shown here [47].

As illustrated in Fig. 5.2, there is always a quasi-constant offset z between the signal from the BPM and the signal from the DDS for which there are several reasons. First, a matched bunch features a current signal with a phase shift of 90° compared to the first harmonic. Second, the BPM and the cavities necessarily have different mounting positions, and third, there are possible differences in cable lengths.

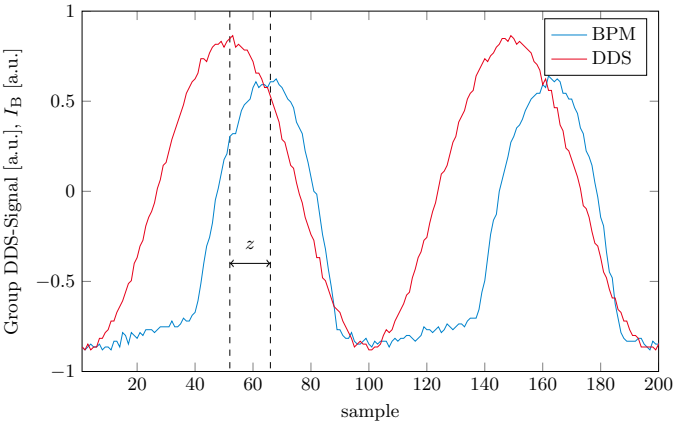

Figure 5.2: Beam current of a matched bunch as measured by a BPM, compared to the DDS signal driving the first cavity with offset z

The bunch center should be located in the rising edge of the DDS signal yielding the 90° phase shift, if both signals are considered as sinusoidal. Due to unbalanced cable lengths in the measurement and the distance of the BPM to the respective cavity, the bunches are shifted further. This offset has to be taken into account during the controller design process and will be addressed in different ways by the approaches presented in the following.

All controller designs presented in this dissertation have in common that they rely on the knowledge of the coherent synchrotron frequency $f_{\mathrm{syn,coh}}$. In Subsec. 3.2.3 different possibilities have been presented to estimate $f_{\mathrm{syn,coh}}$ for a stationary bucket, but also during acceleration the coherent synchrotron frequency could be estimated by simply adapting the respective expressions. In this case the controller has a variable-structure design. The dissertation at hand however focuses on stationary buckets.

The controller computes the actuating variable $-\Delta\varphi_{\mathrm{u,c}}$ which is delayed by a time T_{D} due to cable lengths and total computation time. After the negative feedback (obeying control engineering convention) the value of the delayed actuating variable $\Delta\varphi_{\mathrm{u,d}}(k) = -\Delta\varphi_{\mathrm{u,c}}(k - k_{\mathrm{D}})$ is doubled by a splitter [102] which provides the respective desired phase shifts for the group DDS rack driving the single- and dual-harmonic cavity. Amplitude and frequency of the cavities are provided by the central control system. As the cavities themselves also represent dynamic systems, the actual actuating variable $\Delta\varphi_{\mathrm{u,a}}$ may differ from the desired value. This is however neglected in the the controller design process as the dynamics of the cavities are much faster than the dipole oscillation. At GSI the controller is currently implemented on a digital signal processor (DSP).

5.3 Finite Impulse Response (FIR) Filter

This section introduces the currently used feedback system for the single-harmonic cavity mode which uses an FIR filter in the feedback loop. Furthermore its extension toward the dual-harmonic mode is presented along with alternative filter settings. Some of the results were already published in [107].

An FIR filter of length $N + 1$ has the unit sample response

$$h(n) = \sum_{i=0}^{N} a_i y(n - i)$$

where the coefficients a_i are the so-called *tap weights* of the filter. FIR filters, when compared to *infinite impulse response (IIR)* filters, have the advantage that they can have precise linear phase [89]. The filter in the beam phase feedback has to provide a phase shift of 180° at the passing frequency $f_{\mathrm{pass}} = f_{\mathrm{syn,coh}}$ with the chosen sign of the actuating phase shift in the total voltage

$$V(\Delta\varphi,\Delta\varphi_{\mathrm{u,a}}) = \hat{V}_1 \sin(\varphi_{\mathrm{R}}+\Delta\varphi-\Delta\varphi_{\mathrm{u,a}})+\hat{V}_2 \sin(2(\varphi_{\mathrm{R}}+\Delta\varphi-\Delta\varphi_{\mathrm{u,a}})+\psi),$$

the negative feedback and the integrator for the feedback system to result in total a phase shift of −90° and to provide damping to the beam [3], if $T_{\mathrm{D}} = 0$ and $\Delta\varphi_{\mathrm{u,a}} = \Delta\varphi_{\mathrm{u,d}}$, i. e. if the dynamics of the cavities are

[3] Note that the phase response of a transfer function $H(e^{j\omega T})$ is not consistently defined in the literature. While e. g. [31] defines the phase response $\phi(\omega) =$

negligible. For a linear phase response, it is in general possible to obtain the desired phase shift by adjusting the passing frequency.

The currently used feedback system for the single-harmonic cavity mode consists of a phase discriminator which supplies the output signal $y = \Delta\varphi_{\mathrm{B}} - \Delta\varphi_{\mathrm{u,d}} + z$ and an FIR filter [52] as shown in Fig. 5.1, but without the splitter. Unlike the general controller block in Fig. 5.1 however, the FIR filter in single-harmonic mode does not compute a desired phase shift, but a desired frequency deviation $\Delta\omega_{\mathrm{RF,d}}$. In this case the DDS thus accept a frequency change instead of a phase shift. This was changed in order to implement beam phase control for the dual-harmonic mode, cf. Chap. 6 and [108, 110, 113], and an integrator was added in the feedback.

The filter needs to suppress the measurement offset z and all even multiples of the coherent synchrotron frequency $f_{\mathrm{syn,coh}}$. Even multiples of $f_{\mathrm{syn,coh}}$ correspond to coherent oscillation modes which are damped by changing the voltage magnitude and not its phase. A feedback which also passes even multiples may thus create an unwanted coupling between the different coherent modes.

5.3.1 Currently used Filter Setting

The currently used filter [4] has the discrete transfer function

$$H_{\mathrm{F,current}}(z) = K\left(-1 + 2z^{-\mathrm{int}(1/(2T_{\mathrm{s}}f_{\mathrm{pass}}))} - z^{-\mathrm{int}(1/(T_{\mathrm{s}}f_{\mathrm{pass}}))}\right) \tag{5.2}$$

with a gain K, center frequency of the first passband f_{pass} and sampling period T_{s}, representing a multi-passband with equal heights as depicted in Fig. 5.3. The delays $1/(2T_{\mathrm{s}}f_{\mathrm{pass}})$ and $1/(T_{\mathrm{s}}f_{\mathrm{pass}})$ are rounded toward the nearest integer, denoted by $\mathrm{int}(\cdot)$.

In principle any passband filter fulfilling the requirements given above is suitable to damp coherent dipole oscillations. However, two issues may render certain filters more or less effective. First, the additional time delay T_{D} (cf. Fig. 5.1) introduces an additional phase shift which can be compensated by changing the phase shift provided by the filter. As $H_{\mathrm{F,current}}$ does not provide an additional degree of freedom to change only

$\arctan\left(\frac{\Im(H(e^{j\omega T}))}{\Re(H(e^{j\omega T}))}\right)$, which is also used in the dissertation at hand, e. g. [89] defines $\phi(\omega) = -\arctan\left(\frac{\Im(H(e^{j\omega T}))}{\Re(H(e^{j\omega T}))}\right)$.

[4] This filter setting is further on denoted as the currently used filter, keeping in mind that it is so far only used in single-harmonic cavity mode. The extension toward dual-harmonic cavity mode is a contribution of this dissertation.

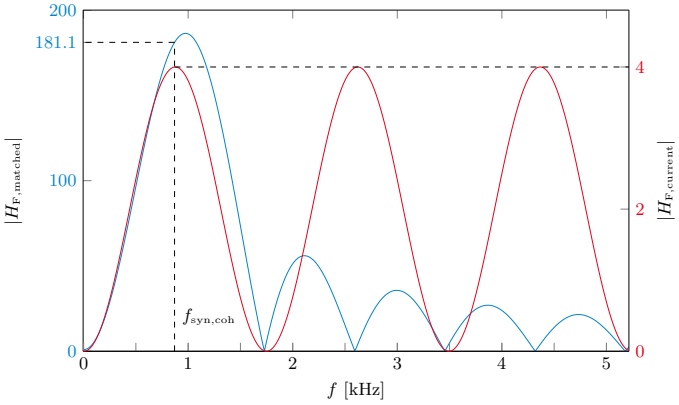

Figure 5.3: Frequency response of the currently used filter and the matched filter at $f_{\mathrm{pass}} = f_{\mathrm{syn,coh}} \approx 870\,\mathrm{Hz}$ for $K = 1$

its phase response, this can only be accomplished by altering the center frequency of the first passband. Second, the feedback loop is only closed by the DSP computing the controller output if a sufficient number of phase measurements matching the length of the filter has been conducted. If for any reason a measurement fails, the control loop is opened until a valid filter output is available again. Although this issue does not necessarily occur often, a shorter filter length may be of benefit. This is in conflict with the requirement that the filter does not pass even multiples of the coherent synchrotron frequency as a narrow passband requires a longer filter if realized as an FIR filter [82].

5.3.2 Alternative Filter Setting

As an alternative filter setting, a *matched filter* was proposed in [21] and [107]. Matched filters are known e. g. from radar applications and are designed to optimize the signal-to-noise ratio (SNR) [35, 64]. Assuming an input signal $s_{\mathrm{i}}(t)$ which is superimposed by white noise $n_{\mathrm{i}}(t)$ with a two-sided power spectral density of $\frac{N_0}{2}$, the filter output is $y(t) = s_{\mathrm{o}}(t) + n_{\mathrm{o}}(t)$. The aim of the matched filter design is to find a filter $h_{\mathrm{F}}(t)$ (or $H_{\mathrm{F}}(\omega)$ in the frequency domain) which maximizes the signal-to-noise ratio [64, 71]

$$SNR(T) = \frac{|s_{\mathrm{o}}(T)|^2}{\overline{n_{\mathrm{o}}^2}}$$

at sampling time instant T, where

$$\overline{n_\mathrm{o}^2} = \frac{N_0}{4\pi} \int\limits_{-\infty}^{\infty} |H(\omega)|^2 \, \mathrm{d}\omega \tag{5.3}$$

is the mean-squared value of the output noise. The output signal at time T is derived by the inverse Fourier transform

$$s_\mathrm{o}(T) = \frac{1}{2\pi} \int\limits_{-\infty}^{\infty} H(\omega) S_\mathrm{i}(\omega) e^{j\omega T} \, \mathrm{d}\omega \tag{5.4}$$

with the Fourier transform $S_\mathrm{i}(\omega)$ of the input signal $s_\mathrm{i}(t)$. With (5.3) and (5.4), the signal-to-noise ratio reads

$$\begin{aligned} SNR(T) &= \frac{\left| \int_{-\infty}^{\infty} H(\omega) S_\mathrm{i}(\omega) e^{j\omega T} \, \mathrm{d}\omega \right|^2}{N_0 \pi \int_{-\infty}^{\infty} |H(\omega)|^2 \, \mathrm{d}\omega} \\ &\leq \frac{\int_{-\infty}^{\infty} |H(\omega)|^2 \, \mathrm{d}\omega \int_{-\infty}^{\infty} |S_\mathrm{i}(\omega)|^2 \, \mathrm{d}\omega}{N_0 \pi \int_{-\infty}^{\infty} |H(\omega)|^2 \, \mathrm{d}\omega} = \frac{1}{N_0 \pi} \int\limits_{-\infty}^{\infty} |S_\mathrm{i}(\omega)|^2 \, \mathrm{d}\omega \end{aligned}$$

applying the Cauchy-Schwarz inequality. Equality only holds if

$$h_\mathrm{F}(t) = K \bar{s}_\mathrm{i}(T - t) \, ,$$

i. e. if the impulse response of the filter is the delayed mirror image of the complex conjugate of the expected signal, possibly with an additional gain K. As the signal in this case is the beam barycenter phase of the coherent dipole oscillation, modeled with a harmonic oscillator, the impulse response of the filter is a cosine function

$$h_\mathrm{F}(t) = K \cos(2\pi f_\mathrm{pass} t + \vartheta(t))$$

in the continuous, respectively

$$h_\mathrm{F}(k) = K \cos(2\pi f_\mathrm{pass} k T_\mathrm{s} + \vartheta(k))$$

in the discrete domain. By the phase shift ϑ the phase of the filter at passing frequency f_pass can be adjusted. The frequency response of the matched filter is also depicted in Fig. 5.3. The corresponding cosine shaped

impulse response covers one period, i. e. the last nonzero tap weight is $N = \text{int}\left\{l \cdot \frac{f_\text{s}}{f_\text{syn,coh}}\right\}$ with $l = 1$. Adjustments of the filter length can easily be accomplished by changing l where a longer filter results in a sharper passband while a shorter filter results in a faster feedback response after the beginning of the measurement. This may be of benefit if the measurement is regularly interrupted.

FIR filters are phase linear, i. e. $\arg(H_\text{F}(\omega)) = \alpha \cdot \omega$, if they have a symmetric or antisymmetric impulse response, which is the case for the presented filters, provided that the impulse response of the matched filter is chosen accordingly. This should be kept in mind when choosing l, as the filter has to provide the desired phase shift of 180°, eventually adjusted by ϑ to counteract time delays in the feedback loop.

Note that the gain of the matched filter at a certain frequency differs a lot from the gain obtained with the currently used filter setting, which is why the corresponding gain K has to be adjusted accordingly. Both filters suppress the frequency $f = 2f_\text{pass} = 2f_\text{syn,coh} \approx 1740\,\text{Hz}$.

In principle also a simple bandpass filter can be used with the center frequency close to the coherent synchrotron frequency and suppression of $2 \cdot f_\text{syn,coh}$ as long as the filter provides the correct phase shift at $f = f_\text{syn,coh}$. The phase shift at the coherent synchrotron frequency depends however on the chosen filter parameters like the filter order, the stopband and passband frequencies and the filter type. When using a bandpass filter, obtaining the correct phase shift and compensation of possible delays in the feedback loop may be subject to trial and error. The phase shift of the matched filter, however, can easily be adjusted by simply changing ϑ. It is thus for the task at hand more intuitive to design than the common bandpass filter.

Fig. 5.4 shows the evolution of the bunch barycenter and the beam emittance according to Eq. (3.2) for an open loop beam, the currently used FIR filter in case of a dual-harmonic cavity operation, the matched filter of length $N = \text{int}\left\{\frac{f_\text{sample}}{f_\text{syn,coh}}\right\}$ and the matched filter of length $N = \text{int}\left\{0.5 \cdot \frac{f_\text{sample}}{f_\text{syn,coh}}\right\}$. Tab. 5.1 lists the chosen parameters of the filters where the gain is normalized to the coherent synchrotron frequency and the sampling time $T_\text{s} = 3.22\,\mu\text{s}$ of the DSP [5]. For parameters of the currently used filter setting see also Chap. 6.

The currently used filter and the matched filter of length $N =$

[5] Normalizing the gain yields similar filter parameters for different coherent synchrotron frequencies, cf. Chap. 6.

$\text{int}\left\{\frac{f_\text{sample}}{f_\text{syn,coh}}\right\}$ start to damp the dipole oscillation after approximately 750 turns corresponding to the length of the filter. Using a matched filter of half length $\left(N = \text{int}\left\{0.5 \cdot \frac{f_\text{sample}}{f_\text{syn,coh}}\right\}\right)$ results in a faster feedback response which is able to keep the emittance lower than the longer filters. This is however only valid, if the phase was not measured before the disturbance occurred or if the measurement was recently interrupted. Otherwise the filters respond immediately. The shorter filter has however a broader passband than the longer ones which may be undesired if the second harmonic of the coherent synchrotron frequency is to be suppressed [107]. On the other hand, the broader passband may be of benefit if the coherent synchrotron frequency is only roughly known.

Table 5.1: Exemplary parameter settings for presented FIR filters

currently used filter	$K/(\omega_\text{syn,coh} \cdot T_\text{s}) = -0.071$ $\frac{f_\text{pass}}{f_\text{syn,coh}} = 1.1$
matched filter $l = 1$	$K/(\omega_\text{syn,coh} \cdot T_\text{s}) = -0.46 \cdot 10^{-3}$ $\frac{f_\text{pass}}{f_\text{syn,coh}} = 1$ $\vartheta = 1.1\pi$
matched filter $l = 0.5$	$K/(\omega_\text{syn,coh} \cdot T_\text{s}) = -2.28 \cdot 10^{-3}$ $\frac{f_\text{pass}}{f_\text{syn,coh}} = 1$ $\vartheta = 1.06\pi$

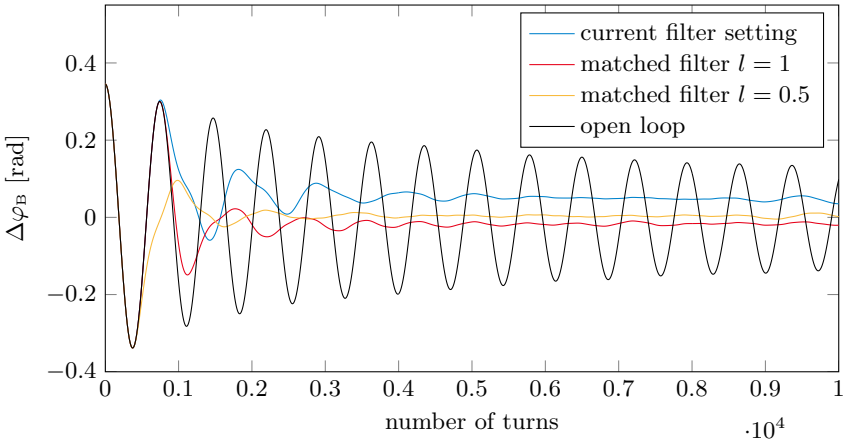

(a) Evolution of bunch barycenter phase in open and closed loop case

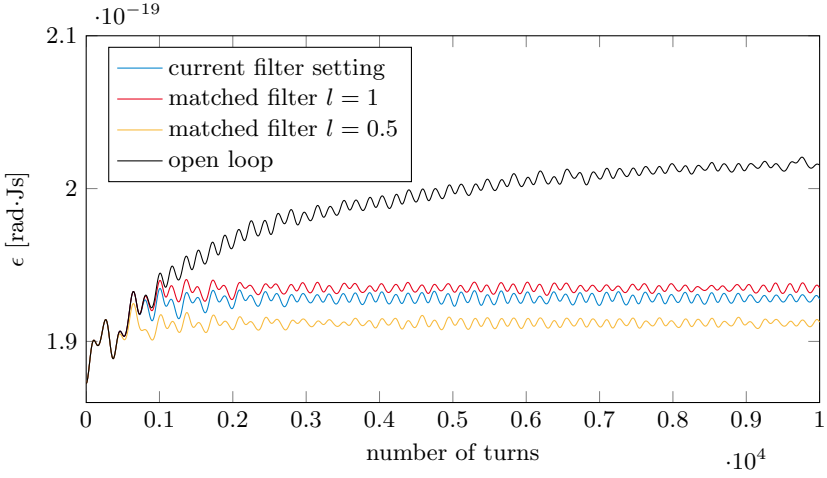

(b) Evolution of bunch emittance in open and closed loop case

Figure 5.4: Simulation results of FIR filters

5.4 Output Feedback

In this section an output feedback resulting in an FIR filter is designed by "classical" control engineering means like pole placement, while the FIR filters presented in Sec. 5.3 were designed with regard to the center frequency of their first passband and the provided phase shift. The integrator which was used in the previous section was introduced to provide the correct phase shift for damping of the bunch oscillations. If the eigenvalues of the closed control loop are chosen appropriately to achieve a damping effect, no integrator is needed which is why it is not considered in this section. It will however become evident that the present constraints the controller is subject to, namely the provision of only the phase deviation of the bunch barycenter and not its energy deviation, restricts the pole placement considerably. Therefore, the desired poles are in general not met accurately. A more exact solution by means of a state feedback in combination with an observer is presented afterward in Sec. 5.5.

The controller feeds back the output vector

$$\boldsymbol{y}(k) = \begin{bmatrix} y(k) & y(k-1) & \dots & y(k-N) \end{bmatrix}^T \in \mathbb{R}^{N+1}$$

consisting of the current measurement and N previous ones, obtaining the control law

$$\Delta\varphi_{\mathrm{u}}(k) = -\boldsymbol{k}^T \boldsymbol{y}(k) \,.$$

Note that no distinction was made between the desired and the actual control variable $\Delta\varphi_{\mathrm{u,d}}$ and $\Delta\varphi_{\mathrm{u,a}}$, neglecting possible time delays in the feedback and the cavity dynamics. This will be continued further on for the controller designs, but time delays and cavity dynamics are still considered in the simulations. For $N = 0$, i. e. if only the current measurement is used, the output feedback reduces to a proportional controller. Damping of dipole oscillations is not possible with a pure proportional control which only provides a phase shift of either 0° or 180°. The required phase shift could only be obtained if an integrator or a differentiator is added. In the first case, however, measurement offset suppression is impossible while the differentiator would highly amplify measurement noise as already mentioned in Sec. 5.1. Using the offset afflicted measurement output

$$y(k) = \Delta\varphi_{\mathrm{B}}(k) - \Delta\varphi_{\mathrm{u}}(k) + z(k)$$

given in Eq. (5.1), where the phase of the bunch barycenter is computed

relative to the actuating variable renders the control law

$$\Delta\varphi_{\mathrm{u}}(k) = -\boldsymbol{k}^T \begin{bmatrix} \Delta\varphi_{\mathrm{B}}(k) - \Delta\varphi_{\mathrm{u}}(k) + z(k) \\ \Delta\varphi_{\mathrm{B}}(k-1) - \Delta\varphi_{\mathrm{u}}(k-1) + z(k) \\ \vdots \\ \Delta\varphi_{\mathrm{B}}(k-N) - \Delta\varphi_{\mathrm{u}}(k-N) + z(k) \end{bmatrix}$$

implicit. There are several ways to deal with this issue of which the following are considered here:

1. Formulating the beam dynamics as a *descriptor system* for which an output feedback can be designed as demonstrated in [72].

2. Adding an additional time delay in the feedthrough loop which can be interpreted as a measurement time delay from the group DDS to the phase discriminator. In this case, the additional state $x_3(k+1) = \Delta\varphi_{\mathrm{u}}(k)$ can be introduced and the control law becomes

$$\Delta\varphi_{\mathrm{u}}(k) = -\boldsymbol{k}^T \begin{bmatrix} \Delta\varphi_{\mathrm{B}}(k-1) - x_3(k) + z(k) \\ \Delta\varphi_{\mathrm{B}}(k-2) - x_3(k-1) + z(k) \\ \vdots \\ \Delta\varphi_{\mathrm{B}}(k-N-1) - x_3(k-N) + z(k) \end{bmatrix} . \quad (5.5)$$

   Note that also $\Delta\varphi_{\mathrm{B}}$ was shifted further in Eq. (5.5).

3. Using an additional DDS running with the first-harmonic cavity frequency (harmonic number $h = 4$) which is not affected by the actuating variable. If the phase of the bunch barycenter is obtained relative to the freely running DDS, no feedthrough is present. There may however still occur an additional measurement offset z.

In all cases suppression of the constant measurement offset z is realized if

$$\boldsymbol{k}^T \boldsymbol{o} = 0 \,, \quad (5.6)$$

where $\boldsymbol{o} = \begin{bmatrix} 1 & \dots & 1 \end{bmatrix}^T$ is a vector of respective length which contains only ones.

To design the output feedback, the *Direct Approach* as introduced by U. Konigorski [29, 53, 54] is used in the following. The derivation closely sticks to [29] and [53] for state space systems and to [72] for the descriptor system, where the procedure is described for time continuous systems.

The approach is however noted here in the discrete time domain. The Direct Approach for an output feedback tries to meet a set of n desired eigenvalues $\lambda_{\mathrm{d},i}$ in the best possible way.

For an introductory explanation of the Direct Approach, consider a time discrete system

$$\begin{aligned} \boldsymbol{x}(k+1) &= \boldsymbol{A}\boldsymbol{x}(k) + \boldsymbol{B}\boldsymbol{u}(k)\,, \\ \boldsymbol{y}(k) &= \boldsymbol{C}\boldsymbol{x}(k)\,, \end{aligned}$$

with $\boldsymbol{A} \in \mathbb{R}^{n\times n}$, $\boldsymbol{B} \in \mathbb{R}^{n\times p}$, $\boldsymbol{C} \in \mathbb{R}^{q\times n}$. Then a given output feedback $\boldsymbol{K}$ shifts the eigenvalues of the closed-loop system to λ_i given by the equation

$$\det\left[\lambda_i \boldsymbol{I}_\mathrm{n} - \boldsymbol{A} + \boldsymbol{B}\boldsymbol{K}\boldsymbol{C}\right] = 0\,.$$

If there exists a $\boldsymbol{K}$ which yields

$$\det\left[\lambda_{\mathrm{d},i} \boldsymbol{I}_\mathrm{n} - \boldsymbol{A} + \boldsymbol{B}\boldsymbol{K}\boldsymbol{C}\right] = 0\,, \tag{5.7}$$

the resulting eigenvalues match the desired eigenvalues exactly. This will however in general not be possible due to the structural restrictions of the feedback

$$\boldsymbol{u} = -\boldsymbol{K}\boldsymbol{C}\boldsymbol{x}$$

unless $\boldsymbol{C} = \boldsymbol{I}_\mathrm{n}$, i. e. if the output feedback turns into a state feedback.

The Direct Approach therefore tries to minimize the deviation of the resulting eigenvalues from their desired location by minimizing a cost function J, yielding the controller gain

$$\boldsymbol{K} = \arg\min_{\boldsymbol{K}} J = \arg\min_{\boldsymbol{K}} \frac{1}{2}\sum_{i=1}^{n} w_{1,i} \left|\det\left[\lambda_{\mathrm{d},i} \boldsymbol{I}_\mathrm{n} - \boldsymbol{A} + \boldsymbol{B}\boldsymbol{K}\boldsymbol{C}\right]\right|^2$$

with weights $w_{1,i} \geq 0$.

For multiple input systems Eq. (5.7) is furthermore nonlinear and only a numerical solution can be expected. As the computational effort to calculate determinants of matrices with n rows grows with n^3, it is first decreased by applying

Theorem 1. *[29] For arbitrary matrices $\boldsymbol{X} \in \mathbb{C}^{n,p}$ and $\boldsymbol{Y} \in \mathbb{C}^{p,n}$*

$$det\left[\boldsymbol{I}_n + \boldsymbol{X}\boldsymbol{Y}\right] = det\left[\boldsymbol{I}_p + \boldsymbol{Y}\boldsymbol{X}\right]\,. \tag{5.8}$$

Eq. (5.7) is rewritten in the form

$$\det\left[\left(\lambda_{\mathrm{d},i} \boldsymbol{I}_\mathrm{n} - \boldsymbol{A}\right)\left(\boldsymbol{I}_\mathrm{n} + \left(\lambda_{\mathrm{d},i} \boldsymbol{I}_\mathrm{n} - \boldsymbol{A}\right)^{-1}\boldsymbol{B}\boldsymbol{K}\boldsymbol{C}\right)\right] = 0$$

$$\Leftrightarrow \det\left[\lambda_{\mathrm{d},i}\boldsymbol{I}_\mathrm{n} - \boldsymbol{A}\right] \cdot \det\left[\boldsymbol{I}_\mathrm{n} + (\lambda_{\mathrm{d},i}\boldsymbol{I}_\mathrm{n} - \boldsymbol{A})^{-1}\boldsymbol{B}\boldsymbol{K}\boldsymbol{C}\right] = 0\,. \quad (5.9)$$

The inverse of $\lambda_{\mathrm{d},i}\boldsymbol{I}_\mathrm{n} - \boldsymbol{A}$ only exists if $\det\left[\lambda_{\mathrm{d},i}\boldsymbol{I}_\mathrm{n} - \boldsymbol{A}\right] \neq 0$. Therefore none of the desired eigenvalues $\lambda_{\mathrm{d},i}$ can equal one of the eigenvalues of the open loop system, and furthermore the desired eigenvalues need to be unique [53]. These restrictions can however be overcome easily as will be shown later. From Eq. (5.8) and (5.9)

$$\begin{aligned} &\det\left[\boldsymbol{I}_\mathrm{n} + (\lambda_{\mathrm{d},i}\boldsymbol{I}_\mathrm{n} - \boldsymbol{A})^{-1}\boldsymbol{B}\boldsymbol{K}\boldsymbol{C}\right] = 0 \\ \Leftrightarrow\ &\det\left[\boldsymbol{I}_\mathrm{p} + \boldsymbol{K}\boldsymbol{C}(\lambda_{\mathrm{d},i}\boldsymbol{I}_\mathrm{n} - \boldsymbol{A})^{-1}\boldsymbol{B}\right] = 0 \\ \Leftrightarrow\ &\det\left[\boldsymbol{I}_\mathrm{p} + \boldsymbol{K}\boldsymbol{G}(\lambda_{\mathrm{d},i})\right] = 0 \end{aligned} \quad (5.10)$$

with the *transfer matrix* $\boldsymbol{G}(z) = \boldsymbol{C}(z\boldsymbol{I}_\mathrm{n} - \boldsymbol{A})^{-1}\boldsymbol{B}$ follows. For a single input system ($p = 1$), $\boldsymbol{I}_\mathrm{p}$ reduces to a scalar and the transfer matrix is reduced to a transfer vector $\boldsymbol{g}(z)$. Eq. (5.10) is now linear in $\boldsymbol{k}$,

$$1 + \boldsymbol{k}^T\boldsymbol{g}(\lambda_{\mathrm{d},i}) = 0\,, \quad i = 1\,, \ldots\,, n\,, \quad (5.11)$$

and can be solved analytically. However, as (5.11) yields n equations for the $q < n$ elements of $\boldsymbol{k}$, no exact solution can be expected and $\boldsymbol{k}$ is again obtained by minimizing the quality criterion

$$J = \frac{1}{2}\sum_{i=1}^{n} w_{1,i}\left|1 + \boldsymbol{k}^T\boldsymbol{g}(\lambda_{\mathrm{d},i})\right|^2\,, \quad w_{1,i} \in \mathbb{R}\,.$$

As the controller has to suppress the measurement offset, the sum of all elements of $\boldsymbol{k}$ has to equal zero and Eq. (5.6) must be fulfilled. This is accounted for by expanding the quality criterion to

$$J = \frac{1}{2}\sum_{i=1}^{n} w_{1,i}\left|1 + \boldsymbol{k}^T\boldsymbol{g}(\lambda_{\mathrm{d},i})\right|^2 + \frac{1}{2}w_2\left(\boldsymbol{k}^T\boldsymbol{o}\right)^2\,, \quad w_2 \in \mathbb{R}\,.$$

Although minimizing J will in general not result in the exact equality $\boldsymbol{k}^T\boldsymbol{o} = 0$, the sum over the controller gain elements is still minimized. Any remaining deviations can be dealt with by defining

$$\boldsymbol{k} := \boldsymbol{k} - \frac{\boldsymbol{k}^T\boldsymbol{o}}{\dim(\boldsymbol{k})} \cdot \boldsymbol{o}$$

where dim denotes the dimension of the vector $\boldsymbol{k}$, i. e. the number of its elements. If $|\boldsymbol{k}^T\boldsymbol{o}|$ is small enough the induced changes of the eigenvalue

configuration is negligible. It also showed to be useful to limit the values of $\boldsymbol{k}^T$ by expanding J to

$$J = \frac{1}{2}\sum_{i=1}^{n} w_{1,i}\left|1+\boldsymbol{k}^T\boldsymbol{g}(\lambda_{\mathrm{d},i})\right|^2 + \frac{1}{2}w_2\left(\boldsymbol{k}^T\boldsymbol{o}\right)^2 + \frac{1}{2}w_3\boldsymbol{k}^T\boldsymbol{k}\,, \quad w_3 \in \mathbb{R}\,.$$

With $\bar{\boldsymbol{g}}(\lambda_{\mathrm{d},i})$ denoting the complex conjugate of $\boldsymbol{g}(\lambda_{\mathrm{d},i})$, the absolute value of the first term can be expanded and J reads

$$J = \frac{1}{2}\sum_{i=1}^{n} w_{1,i}\left(1+\boldsymbol{k}^T\boldsymbol{g}(\lambda_{\mathrm{d},i})\right)\left(1+\boldsymbol{k}^T\bar{\boldsymbol{g}}(\lambda_{\mathrm{d},i})\right) + \frac{1}{2}w_2\left(\boldsymbol{k}^T\boldsymbol{o}\right)^2 + \frac{1}{2}w_3\boldsymbol{k}^T\boldsymbol{k}.$$

To minimize J, its derivative

$$\frac{\partial J}{\partial \boldsymbol{k}} = \begin{bmatrix} \frac{\partial J}{\partial k_1} \\ \vdots \\ \frac{\partial J}{\partial k_q} \end{bmatrix}\,, \tag{5.12a}$$

$$\begin{aligned}\frac{\partial J}{\partial k_\mu} &= \sum_{i=1}^{n} w_{1,i}\frac{\partial\left(1+\boldsymbol{k}^T\boldsymbol{g}(\lambda_{\mathrm{d},i})\right)}{\partial k_\mu}\left(1+\boldsymbol{k}^T\bar{\boldsymbol{g}}(\lambda_{\mathrm{d},i})\right) + w_2\boldsymbol{k}^T\boldsymbol{o} + w_3 k_\mu \\ &= \sum_{i=1}^{n} w_{1,i}\begin{bmatrix}0 & \dots & 1 & \dots & 0\end{bmatrix}\boldsymbol{g}(\lambda_{\mathrm{d},i})\left(1+\bar{\boldsymbol{g}}(\lambda_{\mathrm{d},i})^T\boldsymbol{k}\right) + w_2\boldsymbol{o}^T\boldsymbol{k} \\ &\quad + w_3 k_\mu\,, \quad \mu = 1,\,\dots,\,q\end{aligned} \tag{5.12b}$$

with respect to $\boldsymbol{k}$ is considered, where the '1' is located at position μ (cf. e. g. [29]). Eq. (5.12b) holds because $\boldsymbol{g}(\lambda_{\mathrm{d},i}) = \bar{\boldsymbol{g}}(\lambda_{\mathrm{d},j})$ for $\lambda_{\mathrm{d},i} = \bar{\lambda}_{\mathrm{d},j}$ and if $w_{1,i} = w_{1,j}$ for $\lambda_{\mathrm{d},i} = \bar{\lambda}_{\mathrm{d},j}$ is chosen [53]. This results in

$$\frac{\partial J}{\partial k_\mu} = \sum_{i=1}^{n} w_{1,i} g_\mu(\lambda_{\mathrm{d},i})\left(1+\boldsymbol{g}^*(\lambda_{\mathrm{d},i})\boldsymbol{k}\right) + w_2\boldsymbol{o}^T\boldsymbol{k} + w_3 k_\mu$$

with $\boldsymbol{g}^* = \bar{\boldsymbol{g}}^T$ denoting the adjoint vector to $\boldsymbol{g}$. Thus,

$$\begin{aligned}\frac{\partial J}{\partial \boldsymbol{k}} &= \sum_{i=1}^{n} w_{1,i}\boldsymbol{g}(\lambda_{\mathrm{d},i})\left(1+\boldsymbol{g}^*(\lambda_{\mathrm{d},i})\boldsymbol{k}\right) + w_2\boldsymbol{O}\boldsymbol{k} + w_3\boldsymbol{k} \\ &= \sum_{i=1}^{n} w_{1,i}\boldsymbol{g}(\lambda_{\mathrm{d},i}) + \sum_{i=1}^{n} w_{1,i}\boldsymbol{g}(\lambda_{\mathrm{d},i})\boldsymbol{g}^*(\lambda_{\mathrm{d},i})\boldsymbol{k} + w_2\boldsymbol{O}\boldsymbol{k} + w_3\boldsymbol{k}\end{aligned}$$

$$= \boldsymbol{\Gamma W o} + \boldsymbol{\Gamma W \Gamma}^* \boldsymbol{k} + w_2 \boldsymbol{O k} + w_3 \boldsymbol{k}$$
$$= \boldsymbol{\Gamma W o} + \left(\boldsymbol{\Gamma W \Gamma}^* + w_2 \boldsymbol{O} + w_3 \boldsymbol{I}_\mathrm{n}\right) \boldsymbol{k} \stackrel{!}{=} 0$$

with

$$\boldsymbol{\Gamma} = \begin{bmatrix} \boldsymbol{g}(\lambda_{\mathrm{d},1}) & \dots & \boldsymbol{g}(\lambda_{\mathrm{d},n}) \end{bmatrix}, \quad \boldsymbol{W} = \mathrm{diag}(w_{1,1}\,,\ \dots\ ,\ w_{1,n})$$

and $\boldsymbol{O}$ being a matrix consisting only of ones. An extremum of J requires $\frac{\partial J}{\partial \boldsymbol{k}} = 0$, yielding

$$\boldsymbol{k} = -\left(\boldsymbol{\Gamma W \Gamma}^* + w_2 \boldsymbol{O} + w_3 \boldsymbol{I}_\mathrm{n}\right)^{-1} \boldsymbol{\Gamma W o}\,,$$

which indeed results in a minimum of J [29]. As already mentioned, the approach is restricted to eigenvalues which are unequal to the eigenvalues of the open loop system. This can be overcome by specifying arbitrary support points instead of poles of the desired characteristic polynomial $p(z)$.

Theorem 2. *[90] A polynomial $p(z) = a_n z^n + a_{n-1} z^{n-1} + \dots + a_0$ of the order n is fully characterized by $n+1$ arbitrary support points ξ_i, $\xi_i \neq \xi_j$ for $i \neq j$, and the respective function values $p(\xi_i)$.*

This immediately results in

Theorem 3. *[54] A normalized polynomial $p(z) = z^n + a_{n-1} z^{n-1} + \dots + a_0$ of the order n is fully characterized by n arbitrary support points ξ_i, $\xi_i \neq \xi_j$ for $i \neq j$, and the respective function values $p(\xi_i)$.*

The desired characteristic polynomial

$$p_\mathrm{d}(z) = k_\mathrm{d} \prod_{i=1}^{n} (z - \lambda_{\mathrm{d},i})$$

of the closed loop system is defined by choosing n poles $\lambda_{\mathrm{d},i}$ which may equal poles of the open loop system or be not unique. For $k_\mathrm{d} = 1$ the polynomial is normalized and it is sufficient to choose n arbitrary but unique support points which differ from the poles of the open loop system. If however $k_\mathrm{d} \neq 1$ is chosen, one needs to select $n+1$ support points. In this case k_d can be regarded as an additional optimization variable to minimize J [72]. If support points are complex, also their complex conjugate should be selected [29]. In the following, the quality criterion J is formulated for $n+1$ support points and $k_\mathrm{d} \neq 1$.

The controller gain $\boldsymbol{K}$ now has to fulfill the equations

$$\det\left[\xi_i \boldsymbol{I}_n - \boldsymbol{A} + \boldsymbol{B}\boldsymbol{K}\boldsymbol{C}\right] = p_{\mathrm{d}}(\xi_i)\,, \quad i = 1\,, \dots\,, n+1$$

or

$$\det\left[\xi_i \boldsymbol{I}_p + \boldsymbol{K}\boldsymbol{G}(\xi_i)\right] = \frac{p_{\mathrm{d}}(\xi_i)}{\det\left[\xi_i \boldsymbol{I}_n - \boldsymbol{A}\right]}\,, \quad i = 1\,, \dots\,, n+1 \tag{5.13}$$

respectively. For the single input system ($q = 1$), Eq. (5.13) reduces to

$$1 + \boldsymbol{k}^T \boldsymbol{g}(\xi_i) = \frac{p_{\mathrm{d}}(\xi_i)}{\det\left[\xi_i \boldsymbol{I}_n - \boldsymbol{A}\right]} = \frac{p_{\mathrm{d}}(\xi_i)}{p_{\mathrm{o}}(\xi_i)}$$

where $p_{\mathrm{o}}(z) = \det\left[z\boldsymbol{I}_n - \boldsymbol{A}\right]$ is the characteristic polynomial of the open loop system. The quality criterion now reads

$$J = \frac{1}{2}\sum_{i=1}^{n} w_{1,i} \left| 1 + \boldsymbol{k}^T \boldsymbol{g}(\xi_i) - \frac{p_{\mathrm{d}}(\xi_i)}{p_{\mathrm{o}}(\xi_i)} \right|^2 + w_2 \left(\boldsymbol{k}^T \boldsymbol{o}\right)^2 + w_3 \boldsymbol{k}^T \boldsymbol{k}$$

and a minimum is obtained for

$$\boldsymbol{k} = -\left(\boldsymbol{\Gamma}\boldsymbol{W}\boldsymbol{\Gamma}^* + w_2 \boldsymbol{O} + w_3 \boldsymbol{I}_{\mathrm{n}}\right)^{-1} \left(\boldsymbol{\Gamma}\boldsymbol{W}\boldsymbol{o} - \boldsymbol{\Gamma}\boldsymbol{W}\boldsymbol{p}\right) \tag{5.14}$$

with

$$\boldsymbol{p} = \begin{bmatrix} \frac{p_{\mathrm{d}}(\xi_1)}{p_{\mathrm{o}}(\xi_1)} & \dots & \frac{p_{\mathrm{d}}(\xi_n)}{p_{\mathrm{o}}(\xi_n)} \end{bmatrix}^T .$$

The procedure strongly depends on the choice of the free parameters like the weights, the support points and k_{d}. An optimal choice for the weights $w_{1,i}$ in the sense that the quality criterion increases equally around the different support points is given in [54] for state systems and in [72] for descriptor systems. Assuming that an optimal solution $\boldsymbol{k}_{\mathrm{opt}}$ is known, the $w_{1,i}$-depending part of the error around a support point ξ_i is defined as

$$\epsilon_i(\boldsymbol{k}_{\mathrm{opt}}, \xi) = \frac{1}{2} w_{1,i} \left| 1 + \boldsymbol{k}_{\mathrm{opt}}^T \boldsymbol{g}(\xi) - \frac{p_{\mathrm{d}}(\xi_i)}{p_{\mathrm{o}}(\xi_i)} \right|^2 .$$

As for the optimal solution $\epsilon_i(\boldsymbol{k}_{\mathrm{opt}}, \xi_i) = 0$ as well as $\frac{\partial}{\partial \xi}\, \epsilon_i(\boldsymbol{k}_{\mathrm{opt}}, \xi)|_{\xi=\xi_i} = 0$ hold regardless of $w_{1,i}$, the second derivative of $\epsilon_i(\boldsymbol{k}_{\mathrm{opt}}, \xi)$

$$\frac{\partial^2}{\partial \xi^2}\, \epsilon_i(\boldsymbol{k}_{\mathrm{opt}}, \xi)|_{\xi=\xi_i} = \frac{\partial^2}{\partial \xi^2}\, \epsilon_j(\boldsymbol{k}_{\mathrm{opt}}, \xi)|_{\xi=\xi_j}$$

is regarded to establish an expression of the curvature of J. This leads –after some calculations– to the expression [54, 72]

$$w_{1,i} = \left| \frac{p_0(\xi_i)/p_\mathrm{d}(\xi_i)}{p_\mathrm{d}'(\xi_i)/p_\mathrm{d}(\xi_i) - p_0'(\xi_i)/p_\mathrm{o}(\xi_i)} \right|^2 = \left| \frac{p_0(\xi_i)/p_\mathrm{d}(\xi_i)}{\sum_{j=1}^{n} \frac{1}{\xi_i - \lambda_{\mathrm{d},j}} - \sum_{j=1}^{n} \frac{1}{\xi_i - \lambda_{\mathrm{o},j}}} \right|^2 . \tag{5.15}$$

It is obvious that (5.15) is not valid for any choice $\xi_i = \lambda_{\mathrm{d},j}$, i. e. when a support point equals a desired eigenvalue, because in this case $p_\mathrm{d}(\xi_i) = 0$. If desired eigenvalues are chosen as support points only the specific or all weights must be chosen arbitrarily.

5.4.1 Descriptor Model

Descriptor models allow the incorporation of additional algebraic equations of the form $h(\boldsymbol{x}) = 0$ in the description of the system dynamics. The system equations are formulated as

$$\begin{aligned} \boldsymbol{E}\boldsymbol{x}(k+1) &= \boldsymbol{A}\boldsymbol{x}(k) + \boldsymbol{B}\boldsymbol{u}(k) \,, \\ \boldsymbol{y}(k) &= \boldsymbol{C}\boldsymbol{x}(k) \,. \end{aligned}$$

For $\boldsymbol{E} = \boldsymbol{I}$ the descriptor model simplifies to a state space model. In the present case, the feedthrough can be accounted for by introducing the descriptor $x_3(k) = x_1(k) - \Delta\varphi_\mathrm{u}(k)$ leading to the linear condition $x_1(k) - x_3(k) - \Delta\varphi_\mathrm{u}(k) = 0$ and

$$\boldsymbol{E} = \begin{bmatrix} 1 & 0 & 0 & 0 & \dots & 0 \\ 0 & 1 & 0 & 0 & \dots & 0 \\ 0 & 0 & 0 & 0 & \dots & 0 \\ 0 & 0 & 0 & 1 & \dots & 0 \\ \vdots & \vdots & \vdots & \vdots & \ddots & \vdots \\ 0 & 0 & 0 & 0 & \dots & 1 \end{bmatrix} , \quad \boldsymbol{E} \in \mathbb{R}^{(N+3)\times(N+3)}$$

with the convention

$$x_4(k) = x_3(k-1) \,, \quad x_5(k) = x_4(k-1) \,, \dots \,, \quad x_{N+3}(k) = x_{N+2}(k-1)$$

for the feedback of N previous output measurements.

The system matrix $\boldsymbol{A}$ is composed by the discretized beam dynamics, the algebraic equation $x_1(k) - x_3(k) - \Delta\varphi_\mathrm{u}(k) = 0$ and the time delays for the descriptors x_4 , … , x_{N+3}. As the controller is time discrete with a sampling period of $T_\mathrm{s} = 3.22\,\mu\mathrm{s}$, the system transfer function is sampled with the same frequency. In the continuous time domain the beam dynamics are known from Eq. (3.18),

$$\begin{bmatrix} \Delta\dot{\varphi}_\mathrm{B} \\ \Delta\dot{W}_\mathrm{B} \end{bmatrix} = \underbrace{\begin{bmatrix} 0 & \kappa_1 \\ -\frac{\omega_{\mathrm{syn,coh}}^2}{\kappa_1} & -2d_\mathrm{coh} \end{bmatrix}}_{\boldsymbol{A}_\mathrm{con}} \begin{bmatrix} \Delta\varphi_\mathrm{B} \\ \Delta W_\mathrm{B} \end{bmatrix} + \underbrace{\begin{bmatrix} 0 \\ \frac{\omega_{\mathrm{syn,coh}}^2}{\kappa_1} \end{bmatrix}}_{\boldsymbol{b}_\mathrm{con}} \Delta\varphi_\mathrm{u} \,, \tag{5.16}$$

which are discretized by

$$\boldsymbol{A}_\mathrm{dis} = e^{\boldsymbol{A}_\mathrm{con} T_\mathrm{s}} \,, \tag{5.17a}$$

$$\boldsymbol{b}_\mathrm{dis} = \int_0^{T_\mathrm{s}} e^{\boldsymbol{A}_\mathrm{con}(T_\mathrm{s}-\tau)} \boldsymbol{b}_\mathrm{con}\, \mathrm{d}\tau \,. \tag{5.17b}$$

To obtain better numerical results, the continuous system equations can be normalized according to

$$\Delta\tilde{\varphi}_\mathrm{B} = \frac{\Delta\varphi_\mathrm{B}}{\pi} \,, \tag{5.18a}$$

$$\Delta\tilde{W}_\mathrm{B} = \frac{\Delta W_\mathrm{B}}{\max(\Delta W_\mathrm{sx})} \,, \tag{5.18b}$$

where $\max(\Delta W_\mathrm{sx})$ denotes the maximum normalized energy deviation of the separatrix. Thereby, the bucket spans within a square with edges of length 2 and the differential equations have coefficients of similar power. Normalization of the continuous system dynamics is simply obtained by using the coefficient

$$\tilde{\kappa}_1 = \frac{\max(\Delta W_\mathrm{sx})}{\pi} \kappa_1$$

instead of κ_1 in Eq. (5.16). For the output as well as for the state feedback design a normalized bucket was used. De-normalization of the output feedback parameters is not necessary as the normalization factor does not affect the resulting actuating variable. The system, input and output

matrix of the resulting descriptor system read

$$\boldsymbol{A} = \begin{bmatrix} & \boldsymbol{A}_{\mathrm{dis}} & & 0 & \dots & 0 & 0 \\ & & & 0 & \dots & 0 & 0 \\ 1 & 0 & & -1 & \dots & 0 & 0 \\ 0 & 0 & & 1 & \dots & 0 & 0 \\ \vdots & \vdots & & \vdots & \ddots & \vdots & \vdots \\ 0 & 0 & & 0 & \dots & 1 & 0 \end{bmatrix}, \quad \boldsymbol{A} \in \mathbb{R}^{(N+3)\times(N+3)},$$

$$\boldsymbol{b} = \begin{bmatrix} \boldsymbol{b}_{\mathrm{dis}} \\ -1 \\ 0 \\ \vdots \\ 0 \end{bmatrix}, \quad \boldsymbol{b} \in \mathbb{R}^{(N+3)},$$

$$\boldsymbol{C} = \begin{bmatrix} 0 & 0 & 1 & 0 & \dots & 0 \\ 0 & 0 & 0 & 1 & \dots & 0 \\ \vdots & \vdots & \vdots & \vdots & \ddots & \vdots \\ 0 & 0 & 0 & 0 & \dots & 1 \end{bmatrix}, \quad \boldsymbol{C} \in \mathbb{R}^{(N+1)\times(N+3)}.$$

As introduced in [72], a constant output feedback with the Direct Approach can be designed, keeping in mind that the transfer vector $\boldsymbol{g}(\xi_i)$ in case of a descriptor system reads

$$\boldsymbol{g}(\xi_i) = \boldsymbol{C}(\xi_i \boldsymbol{E} - \boldsymbol{A})^{-1}\boldsymbol{b}$$

and the characteristic polynomial of the open loop system is

$$p_{\mathrm{o}}(\xi_i) = \det\left[\lambda_{\mathrm{d},i}\boldsymbol{E} - \boldsymbol{A}\right].$$

The discretized (and linearized) state space model (5.16) describing rigid dipole oscillations of the exemplary beam (parameters given in Tab. B.1 in App. B) has the eigenvalues

$$\lambda_{1,2} = 0.9998 \pm 0.01758j$$

assuming $d_{\mathrm{coh}} = 0$. This corresponds to neglecting an additional damping due to coherent effects. For $d_{\mathrm{coh}} > 0$, the bunch is additionally stabilized. The case $d_{\mathrm{coh}} < 0$ corresponds to an unstable system. The controller has to be robust enough to still stabilize the beam if external disturbances

are present (cf. Subsec. 5.4.3 and Sec. 5.5). For the controller design the desired eigenvalues are chosen as

$$\lambda_{\mathrm{d},1,2} = 0.9839 \pm 0.01267j \,.$$

The rest of the finite eigenvalues [6] refer to the sampling shifts and can not be moved by the controller. They are thus chosen as

$$\lambda_{\mathrm{d},i} = 0 \,, \quad i = 3 \,, \; \ldots \,, \; n-1 \,.$$

The system has one infinite eigenvalue at $\lambda_\infty = -1$.

As an example, $N = 4$ previously measured values of y are fed back, whereby the descriptor system has the order $n = 7$ and $n_\mathrm{f} = 6$ finite eigenvalues. Using a normalized characteristic polynomial $p_\mathrm{d}(z) = \prod_{i=1}^{n_\mathrm{f}} (z - \lambda_{\mathrm{d},i})$, only n_f support points are needed which are chosen as

$$\boldsymbol{\xi} = \begin{bmatrix} 0.8 & 0.82 & 0.84 & 0.86 & 0.88 & 0.9 \end{bmatrix}^T \,.$$

From (5.15) the weights

$$\boldsymbol{W}_1 = \mathrm{diag}\,(0.5456 \,, \; 0.3566 \,, \; 0.2232 \,, \; 0.1325 \,, \; 0.07368 \,, \; 0.03771)$$

result. Furthermore,

$$w_2 = 100 \,, \quad w_3 = 0.01$$

are chosen. The high value of w_2 ensures that the sum over the elements of the controller gain $\boldsymbol{k}^T$ is small and its values do not have to be changed much to obtain $\boldsymbol{k}^T \boldsymbol{o} = 0$. Eq. (5.14) yields the controller gain

$$\boldsymbol{k}^T = \begin{bmatrix} 0.3621 & 0.1535 & -0.03638 & -0.1911 & -0.2883 \end{bmatrix}$$

with $\boldsymbol{k}^T \boldsymbol{o} = -1.8 \cdot 10^{-4}$. Therefore, $\boldsymbol{k}^T$ has to be changed only little. The resulting eigenvalues of the dipole oscillation are moved to the new location

$$\lambda_{\mathrm{k},1,2} = 0.9996 \pm 0.01758j \,,$$

which is far from the desired values but still provides some additional damping.

The results obtained with the Direct Approach strongly depend on the parameter settings including the weights, the desired pole placement and

[6] Following the convention for time continuous systems, the terms finite and infinite eigenvalues are used. Infinite eigenvalues in the time discrete domain are located at $\lambda_\infty = -1$.

the support points. It is potentially possible to find better parameter settings in order to improve the results, but the effort is quite high and subject to trial and error. The procedure is therefore not suitable for an effective controller design, because

1. the obtained damping is low and
2. for different beam parameters, i. e. different coherent synchrotron frequencies, the resulting pole placement may differ significantly.

It is therefore in general not possible to estimate the damping rate during acceleration of the beam. This is why the approach is not considered any further, especially as in the following much more effective controller designs are presented. For sake of completeness in the next subsection the modeling approach with an additional time delay in the feedthrough is discussed which suffers from the same problems as the descriptor system. In Subsec. 5.4.3 however the approach of using an additional DDS as a reference for the beam phase is presented which yields much better results and allows damping of rigid dipole oscillations with a very short filter.

5.4.2 Additional Time Delay in the Feedthrough

Using an additional time delay in the model equations for the feedthrough is another way to deal with the implicit control law, resulting in Eq. (5.5). With the convention

$$\boldsymbol{x}(k) = \begin{bmatrix} x_1(k) \\ x_2(k) \\ x_3(k) \\ x_4(k) \\ x_5(k) \\ x_6(k) \\ \vdots \\ x_{2N+1}(k) \\ x_{2N+2}(k) \end{bmatrix} = \begin{bmatrix} \Delta\varphi_\mathrm{B}(k) \\ \Delta W_\mathrm{B}(k) \\ \Delta\varphi_\mathrm{u}(k-1) \\ \Delta\varphi_\mathrm{B}(k-1) \\ \Delta\varphi_\mathrm{u}(k-2) \\ \Delta\varphi_\mathrm{B}(k-2) \\ \vdots \\ \Delta\varphi_\mathrm{u}(k-N) \\ \Delta\varphi_\mathrm{B}(k-N) \end{bmatrix}$$

the system, input and output matrix read

$$\boldsymbol{A} = \begin{bmatrix} \multicolumn{2}{c}{\multirow{2}{*}{$\boldsymbol{A}_{\mathrm{dis}}$}} & 0 & \dots & 0 & 0 \\ & & 0 & \dots & 0 & 0 \\ 0 & 0 & 0 & \dots & 0 & 0 \\ 1 & 0 & 0 & \dots & 0 & 0 \\ 0 & 0 & 1 & \dots & 0 & 0 \\ \vdots & \vdots & \vdots & \ddots & \vdots & \vdots \\ 0 & 0 & 0 & \dots & 1 & 0 \end{bmatrix}, \quad \boldsymbol{A} \in \mathbb{R}^{(2N+2)\times(2N+2)},$$

$$\boldsymbol{b} = \begin{bmatrix} \boldsymbol{b}_{\mathrm{dis}} \\ 1 \\ 0 \\ \vdots \\ 0 \end{bmatrix}, \quad \boldsymbol{b} \in \mathbb{R}^{(2N+2)},$$

$$\boldsymbol{C} = \begin{bmatrix} 0 & 0 & -1 & 1 & 0 & 0 & \dots & 0 & 0 \\ 0 & 0 & 0 & 0 & -1 & 1 & \dots & 0 & 0 \\ \vdots & \vdots & & & & & \ddots & \vdots & \vdots \\ 0 & 0 & 0 & 0 & 0 & 0 & \dots & -1 & 1 \end{bmatrix} \in \mathbb{R}^{N\times(2N+2)},$$

and as the previous values of the input variable are now contained in $\boldsymbol{x}(k)$, the system output reduces to

$$\boldsymbol{y}(k) = \begin{bmatrix} y_1(k) & y_2(k) & \dots & y_N(k) \end{bmatrix}^T = \boldsymbol{C}\boldsymbol{x}(k) + \boldsymbol{z}\,.$$

With e. g. $N = 5$, $2N + 2$ supporting points equally distributed within $[0.8,\ 0.9]$, a normalized polynomial (i. e. $k_{\mathrm{d}} = 1$), $\boldsymbol{W}_1 = 10{\cdot}\boldsymbol{I}_{2N+2}$, $w_2 = 1$, $w_3 = 0.01$ and desired poles

$$\lambda_{\mathrm{d},1,2} = 0.9839 \pm 0.01267j$$

for the beam dynamics, a controller gain

$$\boldsymbol{k}^T = \begin{bmatrix} -0.1546 & 0.2711 & 0.4045 & 0.1877 & -0.4385 \end{bmatrix}$$

is obtained. As $\boldsymbol{k}^T\boldsymbol{o} = 0.2702$, the applied changes to the controller parameters are not negligible. The controller is however still stable and places the poles of the beam dynamics at

$$\lambda_{\mathrm{k},1,2} = 0.9997 \pm 0.01759j\,,$$

which is again far from the desired poles.

Similar to the output controller design for the descriptor system, the procedure strongly depends on the parameter choice and will sometimes not yield a stable solution. The approach is therefore again not suitable for an effective controller design.

5.4.3 Removing the Feedthrough

If an additional DDS is used as a reference signal to determine the beam phase (cf. the phase discriminator in Fig. 5.1), the feedthrough is omitted. With the convention

$$\boldsymbol{x}(k) = \begin{bmatrix} x_1(k) \\ x_2(k) \\ x_3(k) \\ \vdots \\ x_{N+2}(k) \end{bmatrix} = \begin{bmatrix} \Delta\varphi_\mathrm{B}(k) \\ \Delta W_\mathrm{B}(k) \\ \Delta\varphi_\mathrm{B}(k-1) \\ \vdots \\ \Delta\varphi_\mathrm{B}(k-N) \end{bmatrix}$$

the system, input and output matrix for feeding back N previously measured values of y are

$$\boldsymbol{A} = \begin{bmatrix} & \boldsymbol{A}_\mathrm{dis} & & 0 & \dots & 0 & 0 \\ & & & 0 & \dots & 0 & 0 \\ 1 & 0 & 0 & \dots & 0 & 0 \\ 0 & 0 & 1 & \dots & 0 & 0 \\ \vdots & \vdots & \vdots & \ddots & \vdots & \vdots \\ 0 & 0 & 0 & \dots & 1 & 0 \end{bmatrix}, \quad \boldsymbol{A} \in \mathbb{R}^{(N+2)\times(N+2)},$$

$$\boldsymbol{b} = \begin{bmatrix} \boldsymbol{b}_\mathrm{dis} \\ 0 \\ \vdots \\ 0 \end{bmatrix}, \quad \boldsymbol{b} \in \mathbb{R}^{(N+2)},$$

$$\boldsymbol{C} = \begin{bmatrix} 1 & 0 & 0 & \dots & 0 \\ 0 & 0 & 1 & \dots & 0 \\ \vdots & \vdots & \vdots & \ddots & \vdots \\ 0 & 0 & 0 & \dots & 1 \end{bmatrix} \in \mathbb{R}^{(N+1)\times(N+2)},$$

with the output vector

$$y(k) = \boldsymbol{C}\boldsymbol{x}(k) + \boldsymbol{z}\,.$$

Choosing the support points

$$\boldsymbol{\xi}^T = \begin{bmatrix} \boldsymbol{\xi}_1^T & \lambda_{\mathrm{d},1} & \lambda_{\mathrm{d},2} \end{bmatrix}$$

with the values of $\boldsymbol{\xi}_1 \in \mathbb{R}^N$ being equally distributed within $[0.8\,,\ 0.9]$, the desired eigenvalues

$$\lambda_{\mathrm{d},1,2} = 0.9839 \pm 0.01267j$$

for the beam dynamics, $N = 6$ previously measured output values $y(k)$, and the weights

$$\boldsymbol{W}_1 = 1000\boldsymbol{I}_{N+2}\,, \quad w_2 = 750\,, \quad w_3 = 1$$

results in the feedback gain

$$\boldsymbol{k}^T = \begin{bmatrix} 7.7088 \\ 5.0830 \\ 2.4682 \\ -0.1173 \\ -2.6513 \\ -5.1063 \\ -7.4486 \end{bmatrix}^T .$$

After adjusting $\boldsymbol{k}^T$ to obtain $\boldsymbol{k}^T\boldsymbol{o} = 0$, the closed loop eigenvalues describing the beam dynamics are located at

$$\lambda_{\mathrm{k},1,2} = 0.9881 \pm 0.0138j$$

which is comparably close to the desired eigenvalues. Fig. 5.5 shows the simulation results with the proposed output feedback in form of the evolution of the bunch barycenter phase as well as the beam emittance according to Eq. (3.2), together with a comparison to the open loop case.

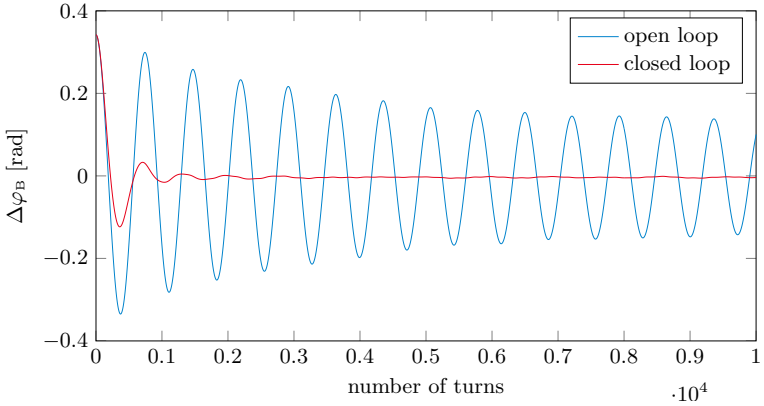

(a) Evolution of bunch barycenter phase in open and closed loop case

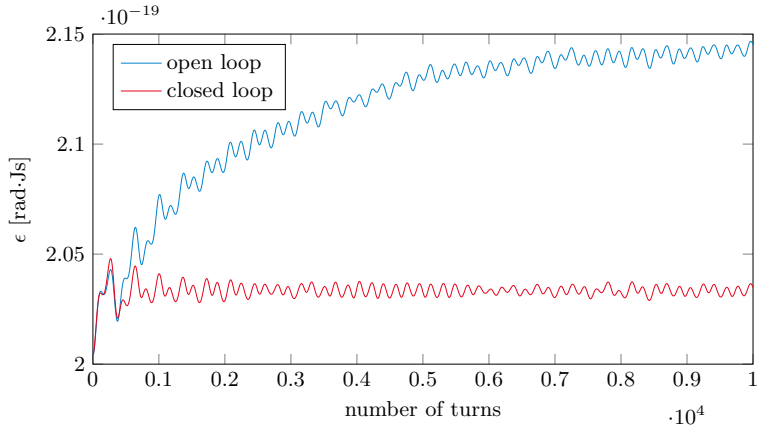

(b) Evolution of bunch emittance in open and closed loop case

Figure 5.5: Simulation results of output feedback

The linear model is however only roughly valid for the nonlinear process of a rigid dipole oscillation with filamentation. Furthermore, the model parameters, i. e. the coherent synchrotron frequency and the damping rate d_{coh} have to be estimated. While this is more or less accurately possible for the frequency (cf. Subsec. 3.2.3), the damping has to be estimated very conservatively. This is due to the fact that the dipole oscillation is not strictly damped for small perturbations, i. e. its amplitude does not necessarily decrease monotonously. Both parameters are furthermore time-varying as the bunch size changes and particles are redistributed in phase space. Therefore, the model suffers from parameter uncertainties which may cause instabilities because the poles of the real closed loop system differ from the pole placement carried out with nominal parameters. The robustness of the output feedback against parameter uncertainties is therefore an important question.

Analysis and optimization of robustness against parameter uncertainty can be carried out by means of *linear matrix inequalities (LMIs)* as demonstrated in [105] [7]. LMIs are widely used for stability analysis or controller design, cf. e. g. [7, 18, 24, 83]. An LMI problem is convex and several numerical solvers e. g. for Matlab like the free sdpt3 [94, 95] or SeDuMi [4, 91] are available. They do however not guarantee to find a valid solution even if one exists.

The aim of [105] is to maximize the region of parameter uncertainty in which stability can be guaranteed for the linear model by varying the initial controller gain. To this end a Lyapunov function $V(\boldsymbol{x}) = \boldsymbol{x}^T \boldsymbol{R} \boldsymbol{x}$ for quadratic stability [10] of the closed loop system

$$\boldsymbol{x}(k+1) = (\boldsymbol{A}_{\mathrm{dis}}(\boldsymbol{q}) - \boldsymbol{b}_{\mathrm{dis}}(\boldsymbol{q})\boldsymbol{k}^T \boldsymbol{C})\boldsymbol{x}(k) = \boldsymbol{A}_{\mathrm{cl}}(\boldsymbol{q}, \boldsymbol{k}^T)\boldsymbol{x}(k)$$

is sought, where $\boldsymbol{q}$ is a vector of uncertain parameters. The resulting stability conditions are

$$\begin{aligned} V(\boldsymbol{x}(k)) &= \boldsymbol{x}^T(k)\boldsymbol{R}\boldsymbol{x}(k) \quad \begin{cases} > 0 & \forall \boldsymbol{x} \neq \boldsymbol{0}\,, \\ = 0 & \boldsymbol{x} = \boldsymbol{0}\,, \end{cases} \\ V(\boldsymbol{x}(k+1)) - V(\boldsymbol{x}(k)) &= \boldsymbol{x}^T(k)\boldsymbol{A}_{\mathrm{cl}}^T \boldsymbol{R} \boldsymbol{A}_{\mathrm{cl}} \boldsymbol{x}(k) - \boldsymbol{x}^T(k)\boldsymbol{R}\boldsymbol{x}(k) \\ &= \boldsymbol{x}^T(k)(\boldsymbol{A}_{\mathrm{cl}}^T \boldsymbol{R} \boldsymbol{A}_{\mathrm{cl}} - \boldsymbol{R})\boldsymbol{x}(k) \\ &\quad \begin{cases} < 0 & \forall \boldsymbol{x} \neq \boldsymbol{0}\,, \\ = 0 & \boldsymbol{x} = \boldsymbol{0}\,, \end{cases} \end{aligned}$$

[7] In [105] robustness optimization for the state feedback presented in Sec. 5.5 is discussed. The results are however also valid in case of an output feedback.

leading to the matrix inequalities

$$\boldsymbol{R} \succ \boldsymbol{0}\,, \tag{5.20a}$$

$$\boldsymbol{A}_{\mathrm{cl}}^{T}(\boldsymbol{q},\boldsymbol{k}^{T})\boldsymbol{R}\boldsymbol{A}_{\mathrm{cl}}(\boldsymbol{q},\boldsymbol{k}^{T}) - \boldsymbol{R} \prec \boldsymbol{0}\,, \tag{5.20b}$$

with $\succ$ ($\prec$) denoting positive (negative) definiteness. The matrix $\boldsymbol{R} = \boldsymbol{R}^{T}$ is symmetric. Assuming a symmetric matrix $\boldsymbol{R}$ does not result in a loss of generality, because if $\boldsymbol{R}$ is not symmetric, always a symmetric matrix $\tilde{\boldsymbol{R}} = \frac{1}{2}(\boldsymbol{R} + \boldsymbol{R}^{T})$ can be defined with $\boldsymbol{x}^{T}\boldsymbol{R}\boldsymbol{X} = \boldsymbol{x}^{T}\tilde{\boldsymbol{R}}\boldsymbol{x}$. The solvers, however, assume matrix variables to be symmetric by default, and the determination of definiteness is simplified if the matrix under consideration is symmetric. If the polytope Q containing all sets of parameters $\boldsymbol{q}$ for which the complete system is stable is convex, it is sufficient to find a single matrix $\boldsymbol{R}$ which fulfills (5.20) for all $\boldsymbol{A}_{\mathrm{cl}}^{T}(\boldsymbol{q}_i,\boldsymbol{k}^{T})$, where $\boldsymbol{q}_i$ denotes the parameter set at the corner vertices of Q [83]. In the following, only hyperrectangles are considered in order to reduce computational cost.

After $\boldsymbol{k}_0^{T}$ has been determined assuming a nominal parameter set $\boldsymbol{q}_0$, the goal of the optimization is to maximize the region Q of parameters for which a Lyapunov function for the system $\boldsymbol{x}_{\mathrm{cl}}(k+1) = \boldsymbol{A}_{\mathrm{cl}}(\boldsymbol{q},\boldsymbol{k}^{T})\boldsymbol{x}_{\mathrm{cl}}(k)$ can be found by altering $\boldsymbol{k}^{T}$.

To express the system matrix $\boldsymbol{A}_{\mathrm{cl}}$ as a function of the uncertain coherent synchrotron frequency and damping rate in an easy fashion, at first discretization of the continuous equations of motion of the bunch barycenter,

$$\begin{bmatrix}\Delta\dot{\tilde{\varphi}}_{\mathrm{B}}\\ \Delta\dot{\tilde{W}}_{\mathrm{B}}\end{bmatrix} = \begin{bmatrix}0 & \tilde{\kappa}_1\\ -\frac{\omega_{\mathrm{syn,coh}}^{2}}{\tilde{\kappa}_1} & -2d_{\mathrm{coh}}\end{bmatrix}\begin{bmatrix}\Delta\tilde{\varphi}_{\mathrm{B}}\\ \Delta\tilde{W}_{\mathrm{B}}\end{bmatrix} + \begin{bmatrix}0\\ \frac{\omega_{\mathrm{syn,coh}}^{2}}{\tilde{\kappa}_1}\end{bmatrix}\Delta\varphi_{\mathrm{u}}$$

is no longer performed according to Eq. (5.17), but instead a simple Euler discretization

$$\begin{bmatrix}x_1(k+1)\\ x_2(k+1)\end{bmatrix} = \underbrace{\begin{bmatrix}1 & T_{\mathrm{s}}\tilde{\kappa}_1\\ -T_{\mathrm{s}}\frac{\omega_{\mathrm{syn,coh}}^{2}}{\tilde{\kappa}_1} & 1-2T_{\mathrm{s}}d_{\mathrm{coh}}\end{bmatrix}}_{\boldsymbol{A}_{\mathrm{dis}}}\begin{bmatrix}x_1(k)\\ x_2(k)\end{bmatrix} + \underbrace{\begin{bmatrix}0\\ T_{\mathrm{s}}\frac{\omega_{\mathrm{syn,coh}}^{2}}{\tilde{\kappa}_1}\end{bmatrix}}_{\boldsymbol{b}_{\mathrm{dis}}}\Delta\varphi_{\mathrm{u}}(k) \tag{5.21a}$$

$$y(k) = \underbrace{\begin{bmatrix}1 & 0\end{bmatrix}}_{\boldsymbol{c}^{T}}\begin{bmatrix}x_1(k)\\ x_2(k)\end{bmatrix} + \underbrace{(-1)}_{d}\Delta\varphi_{\mathrm{u}}(k) + z(k) \tag{5.21b}$$

with

$$\begin{bmatrix} x_1(k) \\ x_2(k) \end{bmatrix} = \begin{bmatrix} \Delta\tilde{\varphi}_{\mathrm{B}}(k) \\ \Delta\tilde{W}_{\mathrm{B}}(k) \end{bmatrix}$$

is used. The Euler discretization is a good approximation of Eq. (5.17) if the sampling time T_{s} is small. In the present case the sampling frequency is $1/T_{\mathrm{s}} \approx 310\,\mathrm{kHz}$ [48] while the coherent synchrotron frequency is in the region of $f_{\mathrm{syn,coh}} \approx 1\,\mathrm{kHz}$, justifying the approximate discretization.

With the uncertain parameter set

$$\boldsymbol{q} = \begin{bmatrix} q_1 \\ q_2 \end{bmatrix} = \begin{bmatrix} \frac{\omega_{\mathrm{syn,coh}}^2}{\tilde{\kappa}_1} \\ 2d_{\mathrm{coh}} \end{bmatrix} = \boldsymbol{q}_0 + \Delta\boldsymbol{q}\,, \tag{5.22}$$

where $\boldsymbol{q}_0 = \begin{bmatrix} q_{1,0} & q_{2,0} \end{bmatrix}^T$ denotes the nominal values, the hyperrectangle Q is reduced to a rectangle with the four corner vertices

$$\begin{aligned} \boldsymbol{q}_i &= \Delta_i \boldsymbol{q}_{\max} + \Delta_i^- \boldsymbol{q}_{\min}\,, \quad i \in \{1,2,3,4\} \\ \boldsymbol{\Delta}_1 &= \begin{bmatrix} 0 & 0 \\ 0 & 0 \end{bmatrix}\,, \quad \boldsymbol{\Delta}_2 = \begin{bmatrix} 1 & 0 \\ 0 & 0 \end{bmatrix}\,, \\ \boldsymbol{\Delta}_3 &= \begin{bmatrix} 0 & 0 \\ 0 & 1 \end{bmatrix}\,, \quad \boldsymbol{\Delta}_4 = \begin{bmatrix} 1 & 0 \\ 0 & 1 \end{bmatrix}\,, \\ \boldsymbol{\Delta}_i^- &= \boldsymbol{I} - \boldsymbol{\Delta}_i \end{aligned}$$

and $\boldsymbol{q}_{\max}$ and $\boldsymbol{q}_{\min}$ denoting the maximum and minimum values of uncertain parameters within the convex envelope spanned by the corners $\boldsymbol{q}_i$, as shown in Fig. 5.6. The rectangle Q can thus be expressed as

$$Q = \{\boldsymbol{q} \in \mathrm{conv}(\Delta_i \boldsymbol{q}_{\max} + \Delta_i^- \boldsymbol{q}_{\min})\}\,.$$

It is easy to see that the inequality (5.20b) is not linear in the variables $\boldsymbol{q}$, $\boldsymbol{k}^T$ and $\boldsymbol{R}$, first because of the multiplication $\boldsymbol{A}_{\mathrm{cl}}\boldsymbol{R}\boldsymbol{A}_{\mathrm{cl}}$ and second because $\boldsymbol{A}_{\mathrm{cl}}(\boldsymbol{q}, \boldsymbol{k}^T)$ features multiplications of the variables $q_{i,1}$ and $\boldsymbol{k}^T$. This renders the problem non-convex. For non-convex matrix inequalities several solving algorithms exist of which two are combined here. The algorithm is divided into two iteration steps in which either $\boldsymbol{R}$ or $\boldsymbol{k}^T$ acts as a variable while the other one is kept constant, analogously to the *V-K-iteration* known from literature [32]. In both cases, however, the corner vertices $\boldsymbol{q}_i$, $i = 1, \ldots 4$ of the domain Q are pushed in order to enlarge the area of Q. Therefore, in each iteration step still a nonlinear matrix

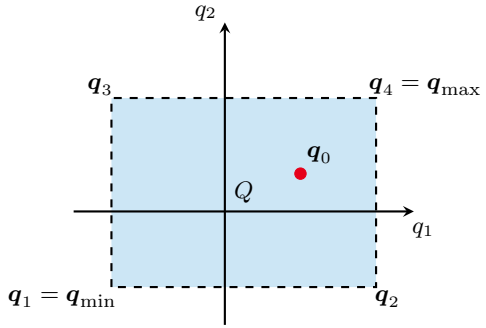

Figure 5.6: Region Q of stable parameters with corner vertices $\boldsymbol{q}_i$ and nominal parameter set $\boldsymbol{q}_0$

inequality has to be solved. This is done by a *path-following algorithm* [39] which linearizes the matrix $\boldsymbol{A}_{\mathrm{cl}}$ around the working points $\boldsymbol{q}_i$. The combined algorithm is depicted in Fig. 5.7. Predefined step sizes for both the optimization of $\boldsymbol{R}$ and $\boldsymbol{k}^T$ keep the search domain within some limits [105].

A validation step is added in each iteration because it is possible that the LMI solver returns an invalid solution. In this case, the new values of $\boldsymbol{q}_i$ and either of $\boldsymbol{R}$ or $\boldsymbol{k}^T$ are discarded and the corresponding step size for the path-following algorithm is reduced.

The algorithm is very sensitive to the choice of the LMI-solver, the Matlab-interface and initial parameters regarding the quality of the solution. Here the solver SeDuMi [4, 91] together with the interface Yalmip [5, 65] were used. Parameter settings are listed in Tab. B.3 in the appendix.

The bunch was initialized according to the parameters in Tab. B.1, but as already mentioned normalized to the new phase space coordinates

$$\Delta\tilde{W} = \frac{\Delta W}{\max(\Delta W_{\mathrm{sx}})}\,, \quad \Delta\tilde{\varphi} = \frac{\Delta\varphi}{\pi}\,,$$

in order to obtain well-conditioned matrices rendering the optimization process numerically more stable.

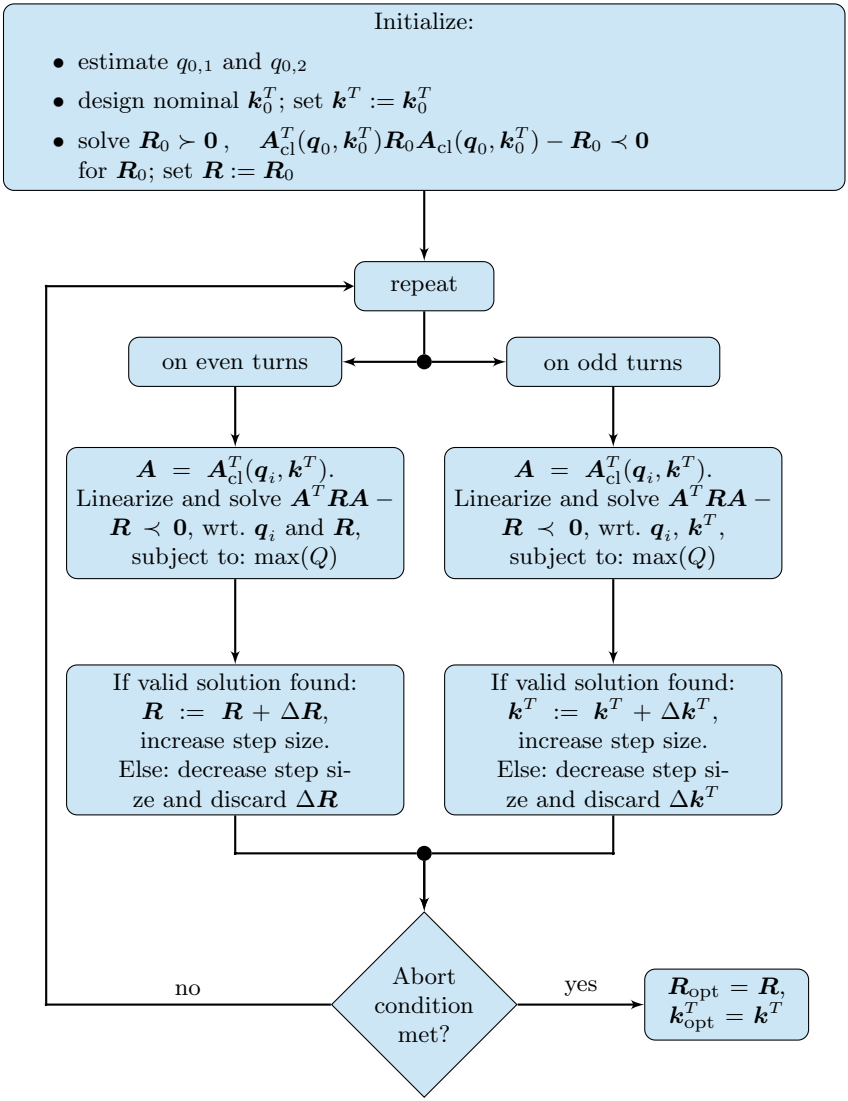

Figure 5.7: Algorithm to solve non-convex matrix inequalities

The applied path-following algorithm needs an initial solution for the controller gain, which is available from the Direct Approach. For the initial controller gain

$$\boldsymbol{k}_0^T = \begin{bmatrix} 7.7088 \\ 5.0830 \\ 2.4682 \\ -0.1173 \\ -2.6513 \\ -5.1063 \\ -7.4486 \end{bmatrix}^T$$

the solver is able to find a Lyapunov matrix guarantying stability of the linear system within the region

$$f_{\mathrm{syn,coh,0,min}} = 490.04\,\mathrm{Hz}\,, \quad f_{\mathrm{syn,coh,0,max}} = 1448.64\,\mathrm{Hz}\,,$$
$$d_{\mathrm{coh,0,min}} = -6.06 \cdot 10^{-6}\,\frac{1}{\mathrm{s}}\,, \quad d_{\mathrm{coh,0,max}} = 277.93\,\frac{1}{\mathrm{s}}\,.$$

After optimization the new gain

$$\boldsymbol{k}^T = \begin{bmatrix} 7.4051 \\ 5.0323 \\ 2.4723 \\ -0.1082 \\ -2.6465 \\ -5.1269 \\ -7.5153 \end{bmatrix}^T$$

is found which differs only little from the initial values. The region of stability for the linearized dynamics,

$$f_{\mathrm{syn,coh,min}} = 152.09\,\mathrm{Hz}\,, \quad f_{\mathrm{syn,coh,max}} = 3948.58\,\mathrm{Hz}\,,$$
$$d_{\mathrm{coh,min}} = -9.03 \cdot 10^{-5}\,\frac{1}{\mathrm{s}}\,, \quad d_{\mathrm{coh,max}} = 2220.24\,\frac{1}{\mathrm{s}}$$

on the other hand increased significantly. Especially the region of uncertainty in which the coherent synchrotron frequency may vary is more than sufficient also for a very rough estimation. The coherent synchrotron frequency may even vary on a large range, e. g. on the acceleration ramp.

It is worth to emphasize that the fact that stability for the initial controller is guaranteed in a smaller region does not necessarily mean that it is unstable outside, but can also mean that the LMI solver was simply

not able to find a better Lyapunov matrix. This is the case here as the controller gain was just slightly altered, and it is apparent that the initial system was already comparably robust. By changing the controller gain, though, the proof of stability for the linear system was possible on a much larger parameter region. The same procedure is however also applied to the state feedback designed in the next section where it is demonstrated that robustness is nonetheless increased.

5.5 State Feedback

To overcome the drawbacks of the output feedback, namely the imprecise pole placement and the sensitivity toward parameter settings, a state space controller can be designed. It is again based on the linearized and normalized discrete equations of motion for rigid dipole oscillations, which are subject to parameter uncertainties. As only the phase of the bunch barycenter can be measured, an observer is needed which estimates the energy deviation of the barycenter, ΔW_B from the measurement output y. However, for deviations of the parameters from their nominal values, i. e. for $\Delta q_1 \neq 0$ or $\Delta q_2 \neq 0$ not only the eigenvalues of the closed loop system differ from the design values, but also the separation theorem is not valid and the controller and the observer cannot be designed separately. Therefore, the controller and the observer are designed simultaneously by means of LMIs as presented in [105] and discretization of the model equations is again performed by a Euler discretization, cf. Eq. (5.21).

Now the feedthrough $d = -1$ proves to be not problematic anymore as it is known to the observer which also estimates $\Delta\varphi_\mathrm{B}$. Nonetheless, the system is not only characterized by the feedthrough, but also by the measurement offset z. Offset-free control, i. e. the robust control of a system subject to measurement offsets is a problem widely discussed in literature. The approach used in this dissertation was presented in [9]. The beam dynamics are extended with a model of the constant offset, as well as with an additional white noise which can affect the states, the offset and the output,

$$\boldsymbol{x}(k+1) = \boldsymbol{A}_\mathrm{dis}\boldsymbol{x}(k) + \boldsymbol{b}_\mathrm{dis}\Delta\varphi_\mathrm{u}(k) + \boldsymbol{G}_\mathrm{x}\boldsymbol{w}_\mathrm{x}(k)\,, \tag{5.23a}$$

$$z(k+1) = z(k) + w_\mathrm{z}(k)\,, \tag{5.23b}$$

$$y(k) = \boldsymbol{c}^T\boldsymbol{x}(k) + d\Delta\varphi_\mathrm{u}(k) + z(k) + w_\mathrm{y}(k)\,. \tag{5.23c}$$

The state process covariance matrix $\boldsymbol{Q}_\mathrm{x}$, offset noise covariance Q_z and

measurement output noise covariance Q_y are given by

$$\begin{aligned} \boldsymbol{Q}_\mathrm{x} = \boldsymbol{Q}_\mathrm{x}^T = \mathrm{E}\left(\boldsymbol{w}_\mathrm{x}\boldsymbol{w}_\mathrm{x}^T\right) \succ \boldsymbol{0}\,, \\ Q_\mathrm{z} = \mathrm{E}\left(w_\mathrm{z} w_\mathrm{z}^T\right) > 0\,, \\ Q_\mathrm{y} = \mathrm{E}\left(w_\mathrm{y} w_\mathrm{y}^T\right) > 0\,. \end{aligned}$$

The noises are furthermore uncorrelated. The extended system (5.23) is rewritten as

$$\begin{aligned} \boldsymbol{X}(k+1) &= \check{\boldsymbol{A}}\boldsymbol{X}(k+t) + \check{\boldsymbol{B}}\Delta\varphi_\mathrm{u}(k) + \check{\boldsymbol{G}}w(k)\,, \\ Y(k) &= \check{\boldsymbol{c}}^T\boldsymbol{X}(k) + d\Delta\varphi_\mathrm{u}(k) + w_\mathrm{y}(k)\,, \end{aligned} \tag{5.24}$$

where

$$\begin{aligned} &\boldsymbol{X} = \begin{bmatrix}\boldsymbol{x}^T & z\end{bmatrix}^T\,, \quad \check{\boldsymbol{A}} = \begin{bmatrix}\boldsymbol{A}_\mathrm{dis} & 0\\ 0 & 1\end{bmatrix}\,, \quad \check{\boldsymbol{b}} = \begin{bmatrix}\boldsymbol{b}_\mathrm{dis}\\ 0\end{bmatrix}\,, \\ &\check{\boldsymbol{G}} = \begin{bmatrix}\boldsymbol{G}_\mathrm{x} & 1\end{bmatrix}\,, \quad \boldsymbol{w} = \begin{bmatrix}\boldsymbol{w}_\mathrm{x}^T & w_\mathrm{z}\end{bmatrix}^T\,, \quad \check{\boldsymbol{c}}^T = \begin{bmatrix}\boldsymbol{c}^T & 1\end{bmatrix}\,. \end{aligned}$$

An observer designed for the extended system (5.24) will estimate the states $\boldsymbol{x}$ of the original system and the constant offset z. In [9], as well as in this dissertation, a Kalman filter [25] is used due to the fact that the measured phase may suffer from stochastic noise (cf. Chap. 6). The observed states $\hat{x}_1$ and $\hat{x}_2$ can be fed back with a state controller as shown in Fig. 5.8. Note that an additional feedthrough in the observer is introduced to compensate the feedthrough of the system.

With the uncertain parameters

$$\boldsymbol{q} = \begin{bmatrix}\frac{\omega_\mathrm{syn,coh}^2}{\tilde{\kappa}_1}\\ 2d_\mathrm{coh}\end{bmatrix}$$

according to Eq. (5.22), the beam dynamics (5.21) extended with the measurement offset z are given by the system matrices

$$\begin{aligned} \check{\boldsymbol{A}}(\boldsymbol{q}) &= \underbrace{\begin{bmatrix}1 & T_\mathrm{s}\kappa_1 & 0\\ -T_\mathrm{s}q_{1,0} & 1 - T_\mathrm{s}q_{2,0} & 0\\ 0 & 0 & 1\end{bmatrix}}_{\check{\boldsymbol{A}}(\boldsymbol{q}_0)} + \underbrace{\begin{bmatrix}0 & 0 & 0\\ -T_\mathrm{s}\Delta q_1 & -T_\mathrm{s}\Delta q_2 & 0\\ 0 & 0 & 0\end{bmatrix}}_{\check{\boldsymbol{A}}(\Delta\boldsymbol{q})}\,, \\ \check{\boldsymbol{b}}(\boldsymbol{q}) &= \underbrace{\begin{bmatrix}0\\ T_\mathrm{s}q_{1,0}\\ 0\end{bmatrix}}_{\check{\boldsymbol{b}}(\boldsymbol{q}_0)} + \underbrace{\begin{bmatrix}0\\ T_\mathrm{s}\Delta q_1\\ 0\end{bmatrix}}_{\check{\boldsymbol{b}}(\Delta\boldsymbol{q})}\,, \end{aligned}$$

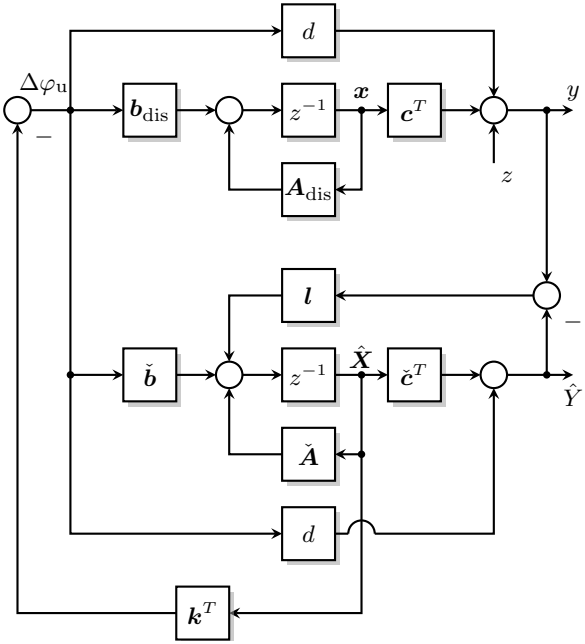

Figure 5.8: Block diagram of state space controller with offset free observer

$$\check{\boldsymbol{c}}^T = \begin{bmatrix} 1 & 0 & 1 \end{bmatrix} .$$

Both, the controller $\boldsymbol{k}^T = \begin{bmatrix} k_1 & k_2 & 0 \end{bmatrix}$ and the observer $\boldsymbol{l} = \begin{bmatrix} l_1 & l_2 & l_3 \end{bmatrix}^T$ are first designed assuming the nominal parameters $\boldsymbol{q}_0$ and optimized later for robustness. The estimation errors

$$\boldsymbol{e} = \begin{bmatrix} e_1 \\ e_2 \\ e_3 \end{bmatrix} = \begin{bmatrix} x_1 - \hat{x}_1 \\ x_2 - \hat{x}_2 \\ z - \hat{z} \end{bmatrix}$$

can thus be described by the difference equation

$$\begin{aligned} \boldsymbol{e}(k+1) &= \boldsymbol{X}(k+1) - \hat{\boldsymbol{X}}(k+1) \\ &= \left(\check{\boldsymbol{A}}(\boldsymbol{q}_0) + \check{\boldsymbol{A}}(\Delta\boldsymbol{q})\right) \boldsymbol{X}(k) - \left(\check{\boldsymbol{b}}(\boldsymbol{q}_0) + \check{\boldsymbol{b}}(\Delta\boldsymbol{q})\right) \boldsymbol{k}^T \hat{\boldsymbol{X}}(k) \\ &\quad - \check{\boldsymbol{A}}(\boldsymbol{q}_0)\hat{\boldsymbol{X}}(k) + \check{\boldsymbol{b}}(\boldsymbol{q}_0)\boldsymbol{k}^T \hat{\boldsymbol{X}}(k) \\ &\quad - \boldsymbol{l}\left(\check{\boldsymbol{c}}^T \boldsymbol{X}(k) + d\boldsymbol{k}^T \hat{\boldsymbol{X}}(k) - \check{\boldsymbol{c}}^T \hat{\boldsymbol{X}}(k) - d\boldsymbol{k}^T \hat{\boldsymbol{X}}(k)\right) \end{aligned}$$

$$
\begin{aligned}
&= \check{\boldsymbol{A}}(\Delta\boldsymbol{q})\boldsymbol{X}(k) - \check{\boldsymbol{b}}(\Delta\boldsymbol{q})\boldsymbol{k}^T\hat{\boldsymbol{X}}(k) + \check{\boldsymbol{A}}(\boldsymbol{q}_0)\boldsymbol{e}(k) + \boldsymbol{l}\check{\boldsymbol{c}}^T\boldsymbol{e}(k) \\
&= \left(\check{\boldsymbol{A}}(\Delta\boldsymbol{q}) - \check{\boldsymbol{b}}(\Delta\boldsymbol{q})\boldsymbol{k}^T\right)\boldsymbol{X}(k) + \left(\check{\boldsymbol{A}}(\boldsymbol{q}_0) + \check{\boldsymbol{b}}(\Delta\boldsymbol{q})\boldsymbol{k}^T + \boldsymbol{l}\check{\boldsymbol{c}}^T\right)\boldsymbol{e}(k)
\end{aligned}
$$

$$
\begin{aligned}
&= \begin{bmatrix} 0 & 0 & 0 \\ -T_\mathrm{s}\Delta q_1(1+k_1) & -T_\mathrm{s}\Delta q_2 - T_\mathrm{s}\Delta q_1 k_2 & 0 \\ 0 & 0 & 0 \end{bmatrix}\boldsymbol{X}(k) \\
&\quad + \begin{bmatrix} 1-l_1 & T_\mathrm{s}\kappa_1 & -l_1 \\ -T_\mathrm{s}q_{1,0}+T_\mathrm{s}\Delta q_1 k_1 - l_2 & 1-T_\mathrm{s}q_{2,0}+T_\mathrm{s}\Delta q_1 k_2 & -l_2 \\ -l_3 & 0 & 1-l_3 \end{bmatrix}\boldsymbol{e}(k)\,.
\end{aligned}
$$

Expressing the control law in terms of the estimation errors, the extended closed loop beam dynamics are

$$
\begin{aligned}
\boldsymbol{X}(k+1) &= \check{\boldsymbol{A}}(\boldsymbol{q})\boldsymbol{X}(k) - \check{\boldsymbol{b}}(\boldsymbol{q})\boldsymbol{k}^T\left(\boldsymbol{X}(k) - \boldsymbol{e}(k)\right) \\
&= \begin{bmatrix} 1 & T_\mathrm{s}\kappa_1 & 0 \\ -T_\mathrm{s}q_1(1+k_1) & 1 - T_\mathrm{s}q_2 - T_\mathrm{s}q_1 k_2 & 0 \\ 0 & 0 & 1 \end{bmatrix}\boldsymbol{X}(k) \\
&\quad + \begin{bmatrix} 0 & 0 & 0 \\ T_\mathrm{s}q_1 k_1 & T_\mathrm{s}q_1 k_2 & 0 \\ 0 & 0 & 0 \end{bmatrix}\boldsymbol{e}(k)\,.
\end{aligned}
$$

Combining the states of the beam dynamics and the observer to the closed loop system $\boldsymbol{x}_\mathrm{cl} = \begin{bmatrix} x_1 & x_2 & z & e_1 & e_2 & e_3 \end{bmatrix}^T$, its dynamics including the controller and observer read

$$
\boldsymbol{x}_\mathrm{cl}(k+1) = \boldsymbol{A}_\mathrm{cl}(\boldsymbol{q}, \boldsymbol{k}^T, \boldsymbol{l})\boldsymbol{x}_\mathrm{cl}(k)\,,
$$

with

$$
\boldsymbol{A}_\mathrm{cl}(\boldsymbol{q}, \boldsymbol{k}^T, \boldsymbol{l}) =
$$

$$
\begin{bmatrix}
1 & T_\mathrm{s}\kappa_1 & 0 & 0 & 0 & 0 \\
-T_\mathrm{s}q_1(1+k_1) & 1-T_\mathrm{s}q_2-T_\mathrm{s}q_1k_2 & 0 & T_\mathrm{s}q_1k_1 & T_\mathrm{s}q_1k_2 & 0 \\
0 & 0 & 1 & 0 & 0 & 0 \\
0 & 0 & 0 & 1-l_1 & T_\mathrm{s}\kappa_1 & -l_1 \\
-T_\mathrm{s}\Delta q_1(1+k_1) & -T_\mathrm{s}(\Delta q_1k_2+\Delta q_2) & 0 & T_\mathrm{s}(-q_{1,0}+\Delta q_1k_1)-l_2 & 1+T_\mathrm{s}(\Delta q_1k_2-q_{2,0}) & -l_2 \\
0 & 0 & 0 & -l_3 & 0 & 1-l_3
\end{bmatrix}.
$$

Note that the measurement offset z has understandably no effect on the dynamics of any other state. For stability analysis it can thus be neglected and in the following $\boldsymbol{x}_\mathrm{cl} = \begin{bmatrix} x_1 & x_2 & e_1 & e_2 & e_3 \end{bmatrix}^T$ and

$$
\boldsymbol{A}_\mathrm{cl}(\boldsymbol{q}, \boldsymbol{k}^T, \boldsymbol{l}) =
$$

$$\begin{bmatrix} 1 & T_s\kappa_1 & 0 & 0 & 0 \\ -T_s q_1(1+k_1) & 1-T_s q_2 - T_s q_1 k_2 & T_s q_1 k_1 & T_s q_1 k_2 & 0 \\ 0 & 0 & 1-l_1 & T_s\kappa_1 & -l_1 \\ -T_s\Delta q_1(1+k_1) & -T_s(\Delta q_1 k_2 + \Delta q_2) & T_s(-q_{1,0}+\Delta q_1 k_1) - l_2 & 1+T_s(\Delta q_1 k_2 - q_{2,0}) & -l_2 \\ 0 & 0 & -l_3 & 0 & 1-l_3 \end{bmatrix}$$

are defined.

Similar to the previous section, finding robust controller and parameter gains is addressed by linear matrix inequalities as demonstrated in [105]. After $\boldsymbol{k}_0^T$ and $\boldsymbol{l}_0$ have been determined assuming a nominal parameter set $\boldsymbol{q}_0$, the goal of the optimization is again to maximize the region Q of parameters in which stability of the linearized system is guaranteed. As the inequality

$$\begin{aligned} \boldsymbol{R} &\succ 0\,, \\ \boldsymbol{A}_{\mathrm{cl}}^T(\boldsymbol{q}, \boldsymbol{k}^T, \boldsymbol{l})\boldsymbol{R}\boldsymbol{A}_{\mathrm{cl}}(\boldsymbol{q}, \boldsymbol{k}^T, \boldsymbol{l}) - \boldsymbol{R} &\prec 0\,, \end{aligned}$$

is again nonlinear in the variables $\boldsymbol{q}$, $\boldsymbol{k}^T$, $\boldsymbol{l}$ and $\boldsymbol{R}$, the same approach as in Sec. 5.4 is applied. The algorithm is now divided into three iteration steps in which either $\boldsymbol{R}$, $\boldsymbol{k}^T$ or $\boldsymbol{l}$ acts as a variable while the other two are kept constant, and in all three cases the corner vertices $\boldsymbol{q}_i$, $i = 1, \ldots 4$ of the domain Q are pushed in order to enlarge the area of Q. The remaining nonlinear matrix inequality in each iteration step is solved by a path-following algorithm.

For a bunch initialized according to Tab. B.3, the desired poles of the controller were placed at

$$\lambda_{\mathrm{des},1,2} = 0.9961 \pm j0.0019$$

and the Kalman filter was designed with assumed noise covariances

$$\boldsymbol{Q}_{\mathrm{x}} = \begin{bmatrix} 0.05 & 0 \\ 0 & 0.05 \end{bmatrix}\,, \quad Q_{\mathrm{z}} = 0.05\,, \quad Q_{\mathrm{y}} = 0.0025\,.$$

While no data for the process and offset noise are available, the measurement noise is comparable to the results obtained in the beam experiment presented in Chap. 6. The covariances $\boldsymbol{Q}_{\mathrm{x}}$ and Q_{z} instead act as weighting coefficients for the observer design. They were chosen heuristically by comparing the resulting pole placements of the observer for the nominal system with the closed loop poles defined by the controller.

Without varying the initial normalized controller and observer gain

$$\tilde{\boldsymbol{k}}_0^T = \begin{bmatrix} -0.9398 & -0.3404 & 0 \end{bmatrix}\,, \quad \tilde{\boldsymbol{l}}_0 = \begin{bmatrix} 0.3060 & -0.9718 & 0.6851 \end{bmatrix}^T\,,$$

the solver is able to find a Lyapunov matrix $\boldsymbol{R}$ guaranteeing stability within the region

$$f_{\mathrm{syn,coh,0,min}} = 629.52\,\mathrm{Hz}\,, \quad f_{\mathrm{syn,coh,0,max}} = 1213.42\,\mathrm{Hz}\,,$$
$$d_{\mathrm{coh,0,min}} = 4.71 \cdot 10^{-5}\,\frac{1}{\mathrm{s}}\,, \quad d_{\mathrm{coh,0,max}} = 195.17\,\frac{1}{\mathrm{s}}\,.$$

After the optimization process the new gains

$$\tilde{\boldsymbol{k}}^T = \begin{bmatrix} -0.9559 & -0.3066 & 0 \end{bmatrix}\,, \quad \tilde{\boldsymbol{l}} = \begin{bmatrix} 0.3041 & -0.9786 & 0.7273 \end{bmatrix}$$

are found which differ once more only little from the initial values. The region of stability for the linearized dynamics however,

$$f_{\mathrm{syn,coh,min}} = 296.62\,\mathrm{Hz}\,, \quad f_{\mathrm{syn,coh,max}} = 2647.43\,\mathrm{Hz}\,,$$
$$d_{\mathrm{coh,min}} = -8.80 \cdot 10^{-7}\,\frac{1}{\mathrm{s}}\,, \quad d_{\mathrm{coh,max}} = 993.17\,\frac{1}{\mathrm{s}}$$

was, like before in Sec. 5.4, significantly increased. For denormalization the relations

$$k_1 = \tilde{k}_1\,, \quad k_2 = \frac{\pi}{\max(\Delta W_{\mathrm{sx}})}\tilde{k}_2$$
$$l_1 = \tilde{l}_1\,, \quad l_2 = \frac{\max(\Delta W_{\mathrm{sx}})}{\pi}\tilde{l}_2\,, \quad l_3 = \tilde{l}_3$$

hold.

Fig. 5.9 shows the simulation results with the proposed state feedback.

After 2000 turns of the bunches in the synchrotron a phase kick of $\Delta\varphi_0 = 20°$ was applied to drive dipole oscillations, giving the observer time to engage. The measurement offset was artificially set to $z(k) = \pi\ \forall k$, i. e. to the maximum possible value. Besides the evolution of the bunch barycenter phase also the emittance growth is depicted in Fig 5.9, both for the closed loop and the open loop case.

As stated above, the fact that the controller and observer gain are changed only little implies that also the initial system may be stable on a larger region than indicated by the initial Lyapunov matrix. To demonstrate that robustness is nonetheless increased, an academic example can be given in which the damping rate of the bunch is lowered by applying a driving force

$$w(k) = -1.55 \cdot \Delta\tilde{W}_{\mathrm{B}}(k)\,,$$
$$\Delta\varphi_{\mathrm{u}}(k) = -\boldsymbol{k}^T\hat{\boldsymbol{X}} + w(k)\,.$$

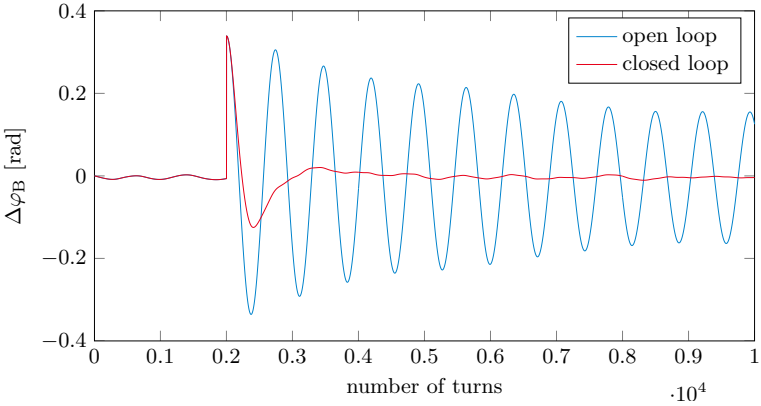

(a) Evolution of bunch barycenter phase in open and closed loop case

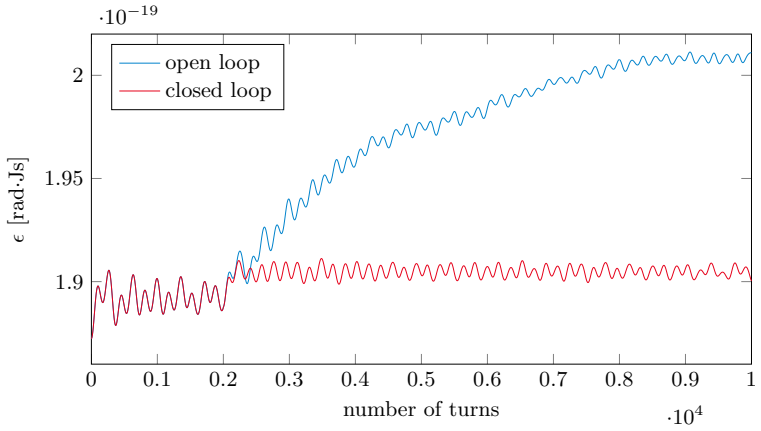

(b) Evolution of bunch emittance in open and closed loop case

Figure 5.9: Simulation results of state feedback

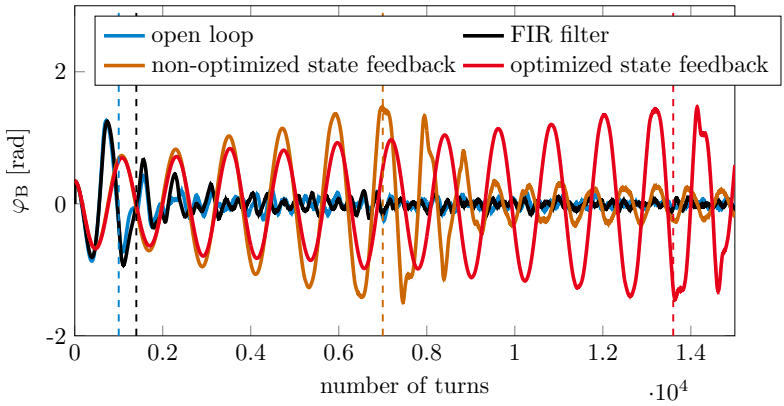

Figure 5.10: Bunch barycenter under a continuous disturbance

Note that $w(k)$ carries a negative sign because the input matrix $\boldsymbol{b}$ of the system has the entry $\frac{\omega_{\mathrm{syn,coh}}^2}{\kappa_1} < 0$. The driving force can be interpreted as an instability due to external effects, where the choice of the gain of 1.55 is arbitrary. The results are depicted in Fig. 5.10 showing the phase of the bunch barycenter φ_B of an open loop bunch and bunches damped by the optimized and the non-optimized state feedback. The bunches were furthermore dislocated by $\varphi_{\mathrm{B},0}$ at the beginning of the simulation, and the measurement offset z was set to zero here to close the control loops already at the first turn. In the open loop case, the particles are lost after only approximately 1000 turns, visible in the noisy evolution and indicated by the vertical blue dashed line. The non-optimized controller loses the bunch after approximately 7500 turns while the optimized controller is able to keep the particles bunched for about 13500 turns. Also shown for comparison is the currently used FIR filter presented in Sec. 5.3 which stabilizes the beam for approximately 1500 turns. Note that a very strong and non-realistic disturbance was applied here to demonstrate robustness.

For implementation, the observer can be expressed as an infinite impulse respond (IIR) filter, avoiding the explicit implementation of the additional states x_2, $\hat{x}_1$, $\hat{x}_2$ and $\hat{z}$ by storage registers. However, one has to keep in mind that the observer has to engage before the control loop is closed. In particular the estimation of the measurement offset z is crucial, and instability of the system may result if the estimated offset differs too much from its actual value.

From the observer equations

$$\begin{aligned}\hat{\boldsymbol{X}}(k+1) &= \left(\check{\boldsymbol{A}}(\boldsymbol{q}_0) - \boldsymbol{l}\check{\boldsymbol{c}}^T\right)\hat{\boldsymbol{X}}(k) + \check{\boldsymbol{b}}(\boldsymbol{q}_0)\Delta\varphi_\mathrm{u}(k) + \boldsymbol{l}(y(k) - d\Delta\varphi_\mathrm{u}(k)) \\ &= \left(\check{\boldsymbol{A}}(\boldsymbol{q}_0) - \boldsymbol{l}\check{\boldsymbol{c}}^T\right)\hat{\boldsymbol{X}}(k) + \tilde{\boldsymbol{b}}(\boldsymbol{q}_0)\Delta\varphi_\mathrm{u}(k) + \boldsymbol{l}y(k)\end{aligned}$$

with

$$\tilde{\boldsymbol{b}}(\boldsymbol{q}_0) = \check{\boldsymbol{b}}(\boldsymbol{q}_0) - \boldsymbol{l}\cdot d = \begin{bmatrix} l_1 \\ T_\mathrm{s}q_{1,0} + l_2 \\ l_3 \end{bmatrix},$$

a z-transform leads to

$$\begin{aligned}\hat{\boldsymbol{X}} &= \left(z\boldsymbol{I} - \check{\boldsymbol{A}}(\boldsymbol{q}_0) + \boldsymbol{l}\check{\boldsymbol{c}}^T\right)^{-1}\left(\tilde{\boldsymbol{b}}(\boldsymbol{q}_0)\Delta\varphi_\mathrm{u} + \boldsymbol{l}y\right) \\ \Leftrightarrow \Delta\varphi_\mathrm{u} &= -\boldsymbol{k}^T\left(z\boldsymbol{I} - \check{\boldsymbol{A}}(\boldsymbol{q}_0) + \boldsymbol{l}\check{\boldsymbol{c}}^T\right)^{-1}\left(\tilde{\boldsymbol{b}}(\boldsymbol{q}_0)\Delta\varphi_\mathrm{u} + \boldsymbol{l}y\right) \\ \Leftrightarrow \Delta\varphi_\mathrm{u}&\left(1 + \boldsymbol{k}^T\left(z\boldsymbol{I} - \check{\boldsymbol{A}}(\boldsymbol{q}_0) + \boldsymbol{l}\check{\boldsymbol{c}}^T\right)^{-1}\tilde{\boldsymbol{b}}(\boldsymbol{q}_0)\right) \\ &= -\boldsymbol{k}^T\left(z\boldsymbol{I} - \check{\boldsymbol{A}}(\boldsymbol{q}_0) + \boldsymbol{l}\check{\boldsymbol{c}}^T\right)^{-1}\boldsymbol{l}y \\ \Leftrightarrow \Delta\varphi_\mathrm{u} &= -\boldsymbol{k}^T\left(z\boldsymbol{I} - \check{\boldsymbol{A}}(\boldsymbol{q}_0) + \boldsymbol{l}\check{\boldsymbol{c}}^T\right)^{-1}\boldsymbol{l} \\ &\quad\left(1 + \boldsymbol{k}^T\left(z\boldsymbol{I} - \check{\boldsymbol{A}}(\boldsymbol{q}_0) + \boldsymbol{l}\check{\boldsymbol{c}}^T\right)^{-1}\tilde{\boldsymbol{b}}(\boldsymbol{q}_0)\right)^{-1} y \\ &= g_{y,\Delta\varphi_\mathrm{u}}(z)y\end{aligned}$$

with the transfer function

$$\begin{aligned}g_{y,\Delta\varphi_\mathrm{u}}(z) = &\Big(z^2(-k_1l_1 - k_2l_2) \\ &+ z(2k_1l_1 + 2k_2l_2 + l_1T_\mathrm{s}(q_{1,0}k_2 - q_{2,0}k_1) - k_1l_2T_\mathrm{s}\kappa_1) \\ &- k_1l_1 - k_2l_2 + l_1T_\mathrm{s}(q_{2,0}k_1 - q_{1,0}k_2) + k_1l_2T_\mathrm{s}\kappa_1\Big) \Big/ \\ &\Big(z^3 + z^2(-3 + l_1 + l_3 + k_2q_{1,0}T_\mathrm{s} + q_{2,0}T_\mathrm{s}) \\ &+ z(3 - 2l_1 - 2l_3 + T_\mathrm{s}(-2 + l_1 + l_3)(k_2q_{1,0} + q_{2,0}) \\ &\quad + l_2T_\mathrm{s}\kappa_1 + q_{1,0}T_\mathrm{s}^2\kappa_1(1 + k_1)) \\ &- 1 + l_1 + l_3 + T_\mathrm{s}(1 - l_1 - l_3)(k_2q_{1,0} + q_{2,0}) - l_2T_\mathrm{s}\kappa_1 +\end{aligned}$$

$$q_{1,0} T_\mathrm{s}^2 \kappa_1 (k_1 + 1)(l_3 - 1)\Big)$$

representing an IIR filter. It is worth noting that designing a classical IIR low pass filter similar to the FIR design presented in Sec. 5.3 suffers from the fact that the cutoff frequency is extremely low compared to the sampling frequency whereby the IIR filters are ill-conditioned. Alternative filter designs dealing with this issue exist, however, and can e. g. be found in [69]. The problem is also overcome (respectively avoided) by the state feedback and observer design.

5.6 Discussion

In this chapter it was demonstrated, that the FIR filter currently used at GSI can be transferred to the dual-harmonic cavity mode, if a phase instead of a frequency correction is provided to the group DDS. For this purpose an additional integrator is implemented in the beam phase control DSP and an optical splitter is used as conducted by the ring RF group at GSI. Also alternative filter designs are possible if they provide the necessary phase shift and suppress the measurement offset and possibly even multiples of the coherent synchrotron frequency.

Instead of an FIR filter design by choosing the passing frequency and phase shift, an output feedback can be designed, e. g. by means of the Direct Approach introduced by U. Konigorski [54]. The procedure is however very sensitive to the chosen parameter settings and may result in a non-optimal solution. On the other hand, if a valid solution is found one ends up with a short FIR filter which effectively damps the dipole oscillation. In addition, no integrator is needed providing a $-90°$ phase shift. Designing longer FIR filters by means of an output feedback, feeding back more previous measurements, tends to result in an invalid solution if the Direct Approach is used. It is worth noting that the output feedback gains in all presented cases have an antisymmetric structure, similar to a type III FIR filter. This indicates an FIR derivative estimator.

A much more accurate pole placement is possible if instead of the output feedback a state feedback along with an observer is used, resulting in an IIR filter. The measurement offset can easily be suppressed by the observer.

For both, the output and the state feedback an analysis and optimization of robustness against parameter uncertainties of the controlled system can be conducted by means of linear matrix inequalities. In principle LMIs can also be used to find initial solutions for the nominal system without

parameter uncertainties in a very convenient way, if the equations of motion are noted in the continuous time domain [105]. In this case also a region for the pole placement can be defined, but no exact pole placement is possible. If the region in which the closed loop poles may vary is chosen too narrow, the solvers might also not be able to find a valid solution. It is thus more constructive to design an initial controller and observer by pole placement or the Direct Approach in case of an output feedback.

6 Beam Experiment

To verify the beam stabilization with an FIR filter, two experiments in the synchrotron SIS18 at GSI were conducted on November 21st, 2012 and on March 23rd, 2014, where the second experiment was a repetition of the first one with a different ion species. The experiments were carried out in close cooperation with the ring RF group at GSI.

In this chapter the results from both experiments are presented, starting with the setting and procedure in Sec. 6.1 and followed by the results in Sec. 6.2. The chapter ends with a discussion in Sec. 6.3.

Some of the results were already published in [106, 108, 110, 113].

6.1 Setting and Procedure

The principal scheme of the beam phase control loop is shown in Fig. 5.1 and the setup for the experiment is depicted in Fig. 6.1.

To create a dual-harmonic bucket, the cavity S02BE1 runs with the harmonic number $h = 4$ while the second cavity S08BE2 is driven with twice the frequency and $h = 8$. Both cavities get their target frequency and amplitude from the central control room (CCR). The target frequency drives the cavity direct digital synthesizer (DDS), whose signal is amplified with the specified peak voltage by the cavity control (cav. ctrl.) which represents nested amplitude and frequency control loops [38]. The summation card (sum. card) adds a desired voltage amplitude specified by an arbitrary wave generator (AWG) to the one defined by the central control room. A phase shift can be applied to the cavity direct digital synthesizer by means of a digital signal processor (DSP) and a calibration electronic (CEL), communicating via a fiber optical hub (FOH). Providing a voltage to the calibration electronic with another arbitrary wave generator causes phase shifts exciting dipole oscillations, while the digital signal processor closes the inner control loop forcing the phase of the cavity voltage to follow a desired value provided to the digital signal processor, if the calibration electronic does not shift the phase further. To drive dipole oscillations, a step voltage was applied to the cavity calibration electronics, repeated

several times with a period of 40 ms. The output voltage of each cavity (cav.) is composed of the voltages at the left and right gap half which add up to the total voltage seen by the beam,

$$\begin{aligned} V_1(t) &= V_{1,\mathrm{l}}(t) + V_{1,\mathrm{r}}(t)\,, \\ V_2(t) &= V_{2,\mathrm{l}}(t) + V_{2,\mathrm{r}}(t)\,, \\ V(t) &= V_1(t) + V_2(t)\,. \end{aligned}$$

Pre-amplifiers amplify the signal coming from the group direct digital synthesizer which the single cavities synchronize to. While the group direct digital synthesizer running at $h = 1$ and the first one running at $h = 4$ are used as a reference for the analysis of the experiment, the second group DDS running at $h = 4$ and the one running at $h = 8$ are shifted in phase by the beam phase control digital signal processor (BPC DSP). The beam phase control DSP uses another fiber optical hub to communicate with the splitter [102] which doubles the desired phase shift at its input on its second output for the second-harmonic cavity S08BE2, while it also passes an unchanged phase on its first output for the first-harmonic cavity S02BE1. On the beam phase control DSP, a phase discriminator is implemented which compares the phase of the beam signal provided by a fast current transformer (FCT) with the signal of the first-harmonic ($h = 4$) group DDS, which is shifted by the controller. The phase discriminator computes the phase difference

$$\Delta\varphi_{\mathrm{det}}(k) = \Delta\varphi_{\mathrm{B}}(k) - \Delta\varphi_{\mathrm{DDS},h=4}(k) + z(k)\,.$$

Note that the measured phase difference is again afflicted by the offset z. The relative phase $\Delta\varphi_{\mathrm{det}}$ is filtered by the filter given in Eq. (5.2) and afterward integrated with the discrete integrator

$$H_{\mathrm{int}}(z) = \frac{z}{z-a}$$

with $a = \frac{32767}{32768}$ [1]. The algorithm is depicted in Fig. 6.2. In the DSP software, the filter gain K in (5.2) is composed of the scaling factor s_{F} and a gain $\tilde{K}$,

$$K = \tilde{K} \cdot s_{\mathrm{F}}\,. \tag{6.1}$$

While the scaling factor was set to the constant value $s_{\mathrm{F}} = \frac{1}{4}$, the gain $\tilde{K}$ is varied.

[1] Note that $a < 1$ to avoid a wind-up effect.

During the experiment the filter parameters, i. e. the center frequency of the first passband f_{pass} [2] and the controller gain $\tilde{K}$ were fixed during one acceleration cycle and adjusted for a specific coherent synchrotron frequency. Therefore, an RF switch driven by an arbitrary wave generator was used to make sure that the beam phase control loop is only closed after the beam reached its flattop energy. For different acceleration cycles different filter gains $\tilde{K}$ and passing frequencies f_{pass} were chosen to analyze the region of stable parameter settings. The beam parameters of the first experiment which took place on November 21st, 2012 are listed in Tab. B.4, and the beam parameters of the second experiment of March 23rd, 2014 in Tab. B.5. Both tables can be found in the appendix.

[2] Further on denoted as the "passing frequency".

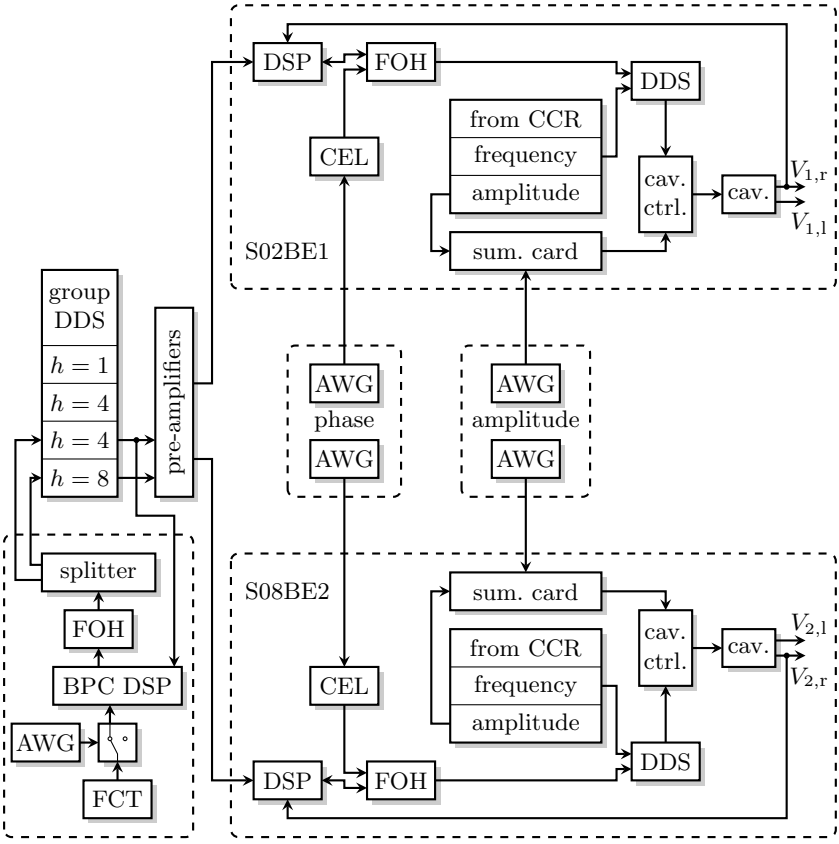

Figure 6.1: Setup of beam experiment

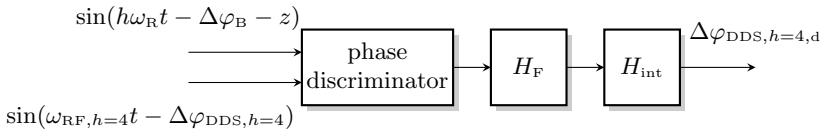

Figure 6.2: The algorithm implemented on the beam phase control digital signal processor (BPC DSP)

6.2 Results

Fig. 6.3 shows the results from the first beam experiment. The stability diagram of the second beam experiment with voltage amplitudes $\hat{V}_1 = 6\,\mathrm{kV}$ and $\hat{V}_2 = 3\,\mathrm{kV}$ is depicted in Fig. 6.4, while the stability diagram of the second experiment with $\hat{V}_1 = 10\,\mathrm{kV}$ and $\hat{V}_2 = 5\,\mathrm{kV}$ is depicted in Fig. 6.5.

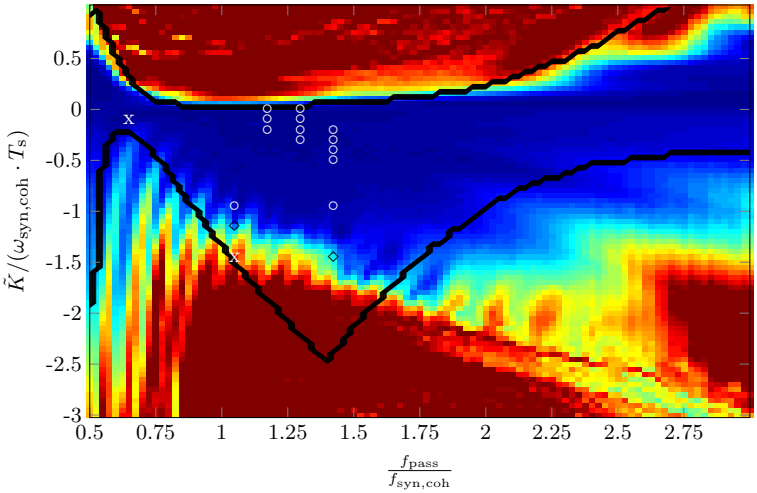

Figure 6.3: Stability diagram of the first beam experiment (November 21st, 2012), $^{238}\mathrm{U}^{73+}$, $\hat{V}_1 = 4\,\mathrm{kV}$

The colored background represents the results from macro-particle simulations in a qualitative manner. Each pixel represents a simulation with the respective filter settings for $\tilde{K}$ and f_{pass}, cf. (5.2) and (6.1). Both parameters are normalized in the diagram with the coherent synchrotron frequency, and $\tilde{K}$ in addition with the sampling time. This makes the shape of the stability region independent of the beam parameters like ion type or beam energy, and of the cavity voltage amplitude.

Blue regions represent stable filter settings while red regions are unstable, where as a stability criterion for the simulations the number of lost particles (i. e. particles outside the bucket) after 5000 turns in the synchrotron was used. The black line surrounds the stable area according to the Nyquist criteria for discrete systems [68], for which also a total time delay of $T_{\mathrm{D}} = 20\,\mu\mathrm{s}$ was assumed in the feedback to account for computation

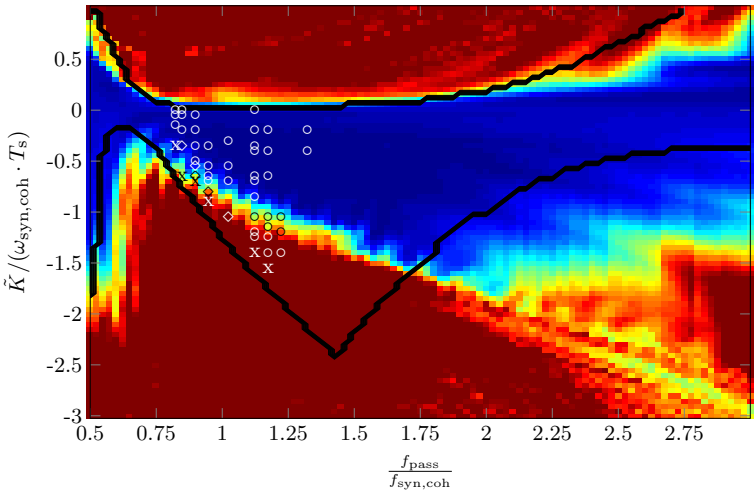

Figure 6.4: Stability diagram of the second beam experiment (March 23rd, 2014), $^{86}\mathrm{Kr}^{33+}$, $\hat{V}_1 = 6\,\mathrm{kV}$

and procession time as well as for delays in the cavities. High intensity effects were not taken into account in this plot in contrast to the other simulations presented in this dissertation, because by omitting high intensity effects the simulations for the stability diagram could be performed on a parallel computing graphics processing unit (GPU). Due to the rather low intensities during the beam experiments this does not contradict the validity of the results. In addition, only $N = 5000$ macro-particles were used to save computation time. A circle (white or black) marks a stable parameter setting in the beam experiment. If the beam was lost or heavily driven by the feedback, the unstable setting is marked with an x. Some parameter settings on the other hand did not cause beam loss but caused significant disturbances in the bunches and were marked with a diamond to indicate critical stability.

The gain $\tilde{K}$ is normalized with the coherent synchrotron frequency and the sampling $T_\mathrm{s} = 3.22\,\mu\mathrm{s}$ of the DSP to make the results comparable to the single-harmonic case (cf. [52]). The additional normalization with the sampling frequency is performed here because of the usage of a time discrete integrator and the provision of a phase correction to the group DDS in the dual-harmonic case, while in the single-harmonic case a frequency correction was supplied. In this case the cavities act as a time continuous

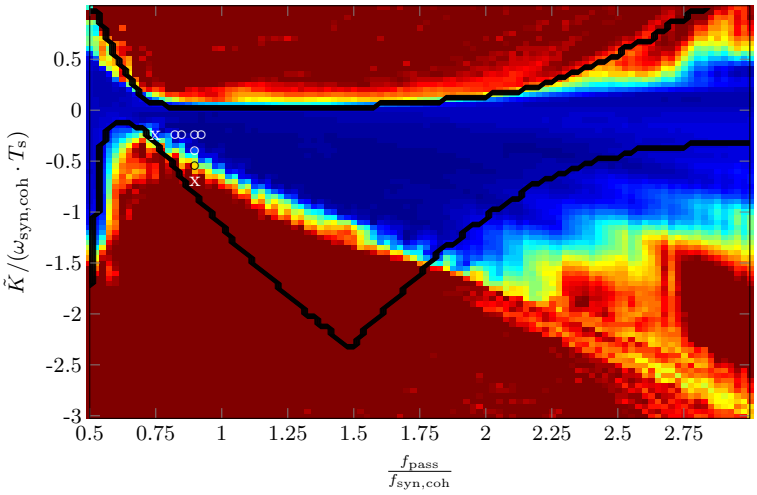

Figure 6.5: Stability diagram of the second beam experiment (March 23rd, 2014), $^{86}\mathrm{Kr}^{33+}$, $\hat{V}_1 = 10\,\mathrm{kV}$

integrator.

It is evident that the macro-particle simulations are in very good agreement with the measurements in all three cases. The Nyquist criterion, however, differs to some extent due to the linearization of the beam dynamics and the neglect of coherent effects, apart from a linear damping term. It can thus only be used as a first estimation of stable filter parameters. Furthermore, it is worth noting that the stability diagrams of all experimental settings are similar, although different ion species and different voltage amplitudes were used. This is due to the normalization with the coherent synchrotron frequency, which depends on the ion species and the voltage amplitude.

Fig. 6.6 shows as an example two measurements from the second experiment, $^{86}\mathrm{Kr}^{33+}$, $\hat{V}_1 = 6\,\mathrm{kV}$, once in open-loop and once with $\tilde{K}/(\omega_{\mathrm{syn,coh}} \cdot T_{\mathrm{s}}) \approx -0.34$, $f_{\mathrm{pass}}/f_{\mathrm{syn,coh}} \approx 1.08$ in closed-loop.

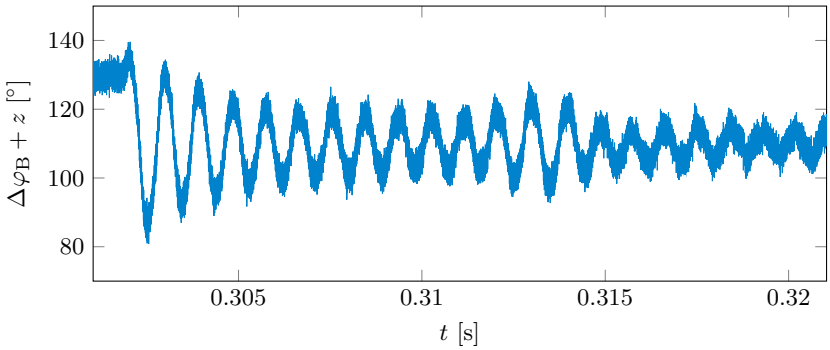

(a) $^{86}Kr^{33+}$, $\hat{V}_1 = 6$kV, open-loop

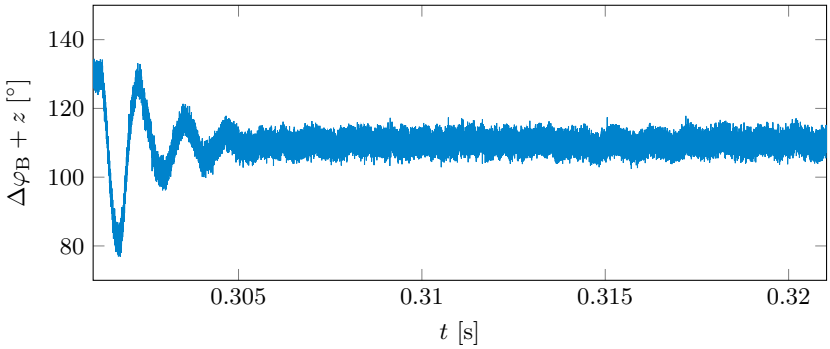

(b) $^{86}Kr^{33+}$, $\hat{V}_1 = 6$kV, $\tilde{K}/(\omega_{\mathrm{syn,coh}} \cdot T_s) \approx -0.34$, $f_{\mathrm{pass}}/f_{\mathrm{syn,coh}} \approx 1.08$

Figure 6.6: Example for measured bunch barycenter evolution after a voltage phase shift, causing a dipole oscillation: $^{86}Kr^{33+}$, $\hat{V}_1 = 6$ kV in open-loop (a), and with $\tilde{K}/(\omega_{\mathrm{syn,coh}} \cdot T_s) \approx -0.34$, $f_{\mathrm{pass}}/f_{\mathrm{syn,coh}} \approx 1.08$ in closed-loop (b)

To find an optimal parameter set $(\tilde{K}/(\omega_{\mathrm{syn,coh}} \cdot T_{\mathrm{s}}),\ f_{\mathrm{pass}})$, the relative emittance growth

$$\Delta\epsilon_{\mathrm{rel}}(k_{\mathrm{end}}) = \frac{\epsilon(k_{\mathrm{end}}) - \epsilon(1)}{\epsilon(1)}$$

after $k_{\mathrm{end}} = 5000$ simulated turns as well as a measure for the signal energy,

$$E_{\mathrm{sig}}(k_{\mathrm{end}}) = \sum_{k=1}^{k_{\mathrm{end}}} \Delta\varphi_{\mathrm{B}}(k)^2$$

were regarded. The results can be seen in Fig. 6.7. Note that the maximum values have been limited for sake of clarity.

A low emittance growth is obtained for a gain comparatively close to the border of stability, while a smaller signal energy is reached for a gain and passing frequency with some tolerance to unstable parameter settings. It is suggested to use the parameters for a small signal energy in the synchrotron to increase robustness against parameter uncertainties because of the normalization with the coherent synchrotron frequency. Furthermore, the optimal parameter set obtained for a *small signal energy* also yields a comparatively *low emittance growth*. Therefore, only a little trade-off is necessary when using the optimal parameters for small signal energy, but robustness is strongly increased. Tab. 6.1 lists the optimal parameters obtained in the three presented simulations.

Table 6.1: Optimal parameter settings according to simulations

	$^{238}\mathrm{U}^{73+}$, $\hat{V}_1 = 4\,\mathrm{kV}$	$^{86}\mathrm{Kr}^{33+}$, $\hat{V}_1 = 6\,\mathrm{kV}$	$^{86}\mathrm{Kr}^{33+}$, $\hat{V}_1 = 10\,\mathrm{kV}$
$\frac{\tilde{K}_{\mathrm{opt}}}{\omega_{\mathrm{syn,coh}} \cdot T_{\mathrm{s}}}$	-0.25	-0.3	-0.3
$\frac{f_{\mathrm{pass,opt}}}{f_{\mathrm{syn,coh}}}$	1.025	1.1	1.125
$T_{\mathrm{D,est}}$	$16\,\mu\mathrm{s}$	$45\,\mu\mathrm{s}$	$22\,\mu\mathrm{s}$

For both the normalized gain and the passing frequency, the simulations yield similar optimal values. Note that the optimal passing frequency is slightly bigger than the coherent synchrotron tune shift. The phase shift of 180° required to provide damping to the system is exactly met for $f_{\mathrm{pass}} = f_{\mathrm{syn,coh}}$. Nevertheless, the dead time due to cable lengths, computation time or cavity dynamics shifts the phase further, cf. Sec. 5.2. By changing

f_{pass}, this phase shift can be compensated by the filter. This is depicted in Fig. 6.8 showing the phase response of two FIR filters, which were both designed for $^{86}\mathrm{Kr}^{33+}$, $\hat{V}_1 = 6\,\mathrm{kV}$. The filter, whose phase response is shown in red has a passing frequency of $f_{\mathrm{pass}} = f_{\mathrm{syn,coh}}$, while the one whose phase response is shown in blue has a passing frequency of $f_{\mathrm{pass}} = 1.1 f_{\mathrm{syn,coh}}$. By the phase difference

$$\begin{aligned}\Delta\varphi_{\mathrm{D}} = &\arg(H_{\mathrm{F},f_{\mathrm{pass}}=1.1f_{\mathrm{syn,coh}}}(f_{\mathrm{syn,coh}})) \\ &- \arg(H_{\mathrm{F},f_{\mathrm{pass}}=f_{\mathrm{syn,coh}}}(f_{\mathrm{syn,coh}}))\,,\end{aligned}$$

the unknown dead time can be estimated. The respective values for the three experimental settings are also listed in Tab. 6.1.

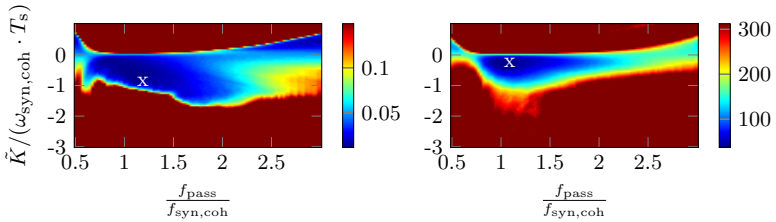

(a) Emittance growths $\Delta\epsilon_{\mathrm{rel}}(k_{\mathrm{end}})$, $^{238}\mathrm{U}^{73+}$, $\hat{V}_1 = 4\mathrm{kV}$

(b) Signal energy $E_{\mathrm{sig}}(k_{\mathrm{end}})$, $^{238}\mathrm{U}^{73+}$, $\hat{V}_1 = 4\mathrm{kV}$

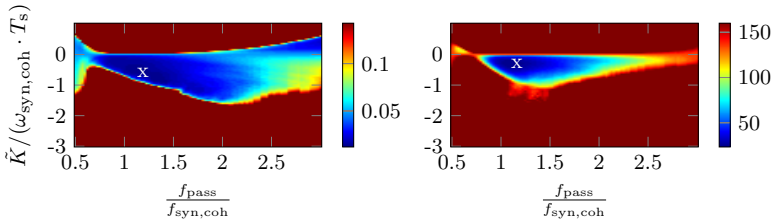

(c) Emittance growths $\Delta\epsilon_{\mathrm{rel}}(k_{\mathrm{end}})$, $^{86}\mathrm{Kr}^{33+}$, $\hat{V}_1 = 6\mathrm{kV}$

(d) Signal energy $E_{\mathrm{sig}}(k_{\mathrm{end}})$, $^{86}\mathrm{Kr}^{33+}$, $\hat{V}_1 = 6\mathrm{kV}$

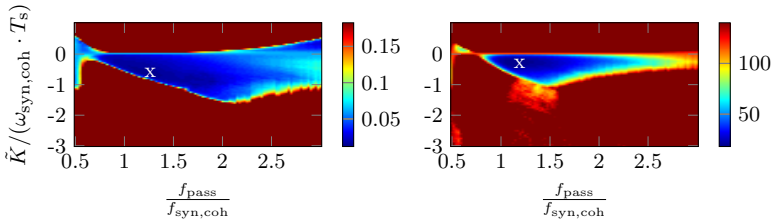

(e) Emittance growths $\Delta\epsilon_{\mathrm{rel}}(k_{\mathrm{end}})$, $^{86}\mathrm{Kr}^{33+}$, $\hat{V}_1 = 10\mathrm{kV}$

(f) Signal energy $E_{\mathrm{sig}}(k_{\mathrm{end}})$, $^{86}\mathrm{Kr}^{33+}$, $\hat{V}_1 = 10\mathrm{kV}$

Figure 6.7: Relative emittance growth $\Delta\epsilon_{\mathrm{rel}}(k_{\mathrm{end}})$ and measure for signal energy $E_{\mathrm{sig}}(k_{\mathrm{end}})$ (in arbitrary units) after $k_{\mathrm{end}} = 5000$ simulated turns

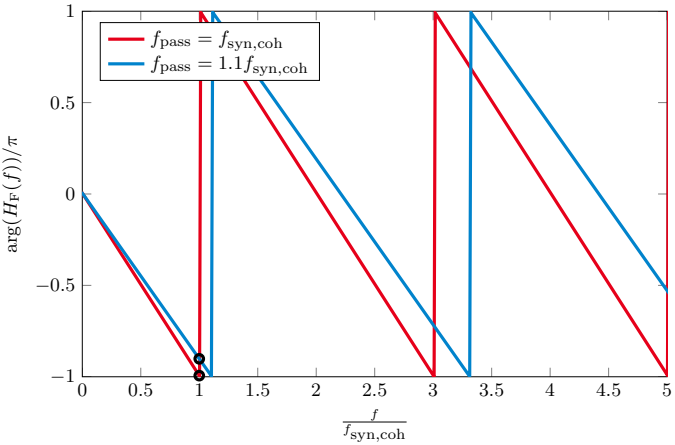

Figure 6.8: Phase response of FIR filters

6.3 Discussion

The coherent synchrotron frequency was badly estimated during the first beam experiment which is why measurements are concentrated at a passing frequency of $f_{\mathrm{pass}} \approx 1.25 f_{\mathrm{syn,coh}}$. This was corrected in the second experiment, and more measurements could be taken due to a longer beam time.

From the experiments it is evident that

1. the FIR filter can effectively be used to damp rigid dipole oscillations also in a dual-harmonic bucket.

2. in all three cases, the stability diagram obtained with macro-particle simulations could be accurately verified by the measurements.

3. the Nyquist criterion can be used to get a first estimation of stable filter parameters.

4. the damping of longitudinal rigid dipole oscillations in SIS18 operating in dual-harmonic cavity mode is now fully understood.

Furthermore, in all experiments the obtained stability diagram and optimal parameter set is comparable regardless of the ion species or the cavity voltage amplitude, due to the normalization with the coherent synchrotron frequency $f_{\mathrm{syn,coh}}$.

So far the beam phase feedback is only implemented for a stationary bucket in which the coherent synchrotron frequency and thus the optimal passing frequency of the filter does not change. During acceleration, the filter parameters have to be adjusted e. g. by switching between several parameter sets. To this end, the current coherent synchrotron frequency has to be provided to the beam phase control DSP.

7 Conclusion

Particle bunches in a synchrotron are in general subject to various disturbances which may drive different kinds of coherent bunch oscillations. These can furthermore be caused by non-ideal initial conditions like e. g. phase or energy errors due to an incorrect injection. As bunch oscillations lower the beam quality by increasing the rms emittance and can also result in particle loss, control measures are taken to damp the coherent bunch oscillations and to stabilize the beam.

In the course of the construction of the Facility for Antiproton and Ion Research (FAIR) at GSI Helmholtzzentrum für Schwerionenforschung GmbH, the existing synchrotron SIS18 is switched from single-harmonic to dual-harmonic cavity operation in bunch lengthening mode. This introduces an additional nonlinearity in the longitudinal particle dynamics. "Classical" controller design approaches for the single-harmonic cavity mode, which linearize the particle dynamics around the reference point are thus not applicable anymore, and new methods are needed, e. g. to obtain the coherent synchrotron frequency of the dipole mode. For more sophisticated controller designs also a mathematical model of the beam dynamics is needed.

This question was answered in the dissertation at hand by means of a central moment modeling approach which results in a simple, yet sufficiently accurate linear model of the dipole oscillation, also yielding the coherent synchrotron frequency. Based on these results, the FIR filter currently used for the damping of dipole oscillations in the single-harmonic domain is transferred to the dual-harmonic case and its suitability is analyzed. Furthermore, an alternative filter design is presented and the results are compared. As an FIR filter represents a constant output feedback, it seems logical to design an output feedback by e. g. pole placement. The procedure suffers however from a high sensitivity toward parameter settings. This can be avoided if instead of the output feedback a state feedback is designed, requiring an observer to estimate the non-measurable energy deviation of the bunch barycenter. For a more convenient implementation, the state feedback and observer can be expressed as an IIR filter. The output and the state feedback are optimized concerning their

robustness against modeling parameter uncertainties by means of linear matrix inequalities. Stability and effectiveness of the controllers are verified in macro-particle simulations taking into account time delays, the cavity dynamics and high intensity effects. Especially the state feedback proves to be very efficient, providing a fast damping while keeping the rms emittance of the bunch low, and as it is designed by pole placement, its performance is easy to adjust. Although the controllers were only presented for stationary bunches, the design approaches are also valid during acceleration. In this case, however, a more sophisticated distribution function is needed to describe the particles in phase space, which is used during the modeling of the bunch barycenter dynamics.

In addition to the simulations, two beam experiments were performed where the feedback was closed with an FIR filter and discrete integrator as developed by the ring RF group at GSI. Thereby the stability diagrams of stable filter parameters as predicted in simulations could be verified and an optimal parameter set could be found. In the experiment, the bunches were excited to perform dipole oscillations by shifting the phase of the RF voltage after the bunches reached extraction energy. An RF switch made sure that the control loop was not closed earlier on the acceleration ramp in which case the filter parameters would have been to be adjusted online.

Further development is needed to close the feedback loop also during acceleration. The parameters of the FIR filters have to be adjusted frequently as the coherent synchrotron frequency changes which has to be provided to the beam phase control DSP.

If other controllers than the FIR filter used in the experiments are to be implemented, it has to be investigated whether the DSP is capable of a real time operation even when the calculations become more complex. Eventually an implementation on FPGAs should be considered. While the matched filter only requires more multiplications and the summation over more elements, the state feedback requires the implementation of an IIR filter. It also has to be made sure that the observer has enough time to engage before the control loop is closed. The time needed depends on the value of the measurement offset.

Damping of quadrupole oscillations is not yet treated for dual-harmonic RF systems. In principle the same approach is practicable consisting of the linearization of the central moment dynamics and a corresponding feedback design. If a coupling of the dipole and quadrupole mode in case of a non-stationary beam exists, a multivariable control is worth to be considered.

A Accelerator Physics

A.1 Quantity Relations for Relativistic Particles

This section gives a short overview on the relations between different quantities of relativistic particles which can e. g. be found in [17].

Quantities which are important in the main part of the thesis are the relativistic normalized velocity β, the relativistic normalized energy γ which is also known as the Lorentz factor, the total energy E, the kinetic energy E_{kin} and the momentum p. They depend on the rest mass m_0 and the speed of light in vacuum c and can be expressed as a function of one other quantity as listed in Tab. A.1. In addition, the relativistic mass m is defined as

$$m = \gamma m_0 \,.$$

The first derivatives can also be put into relation resulting in

$$\frac{\mathrm{d}p}{p} = \gamma^2 \frac{\mathrm{d}v}{v} = \gamma^2 \frac{\mathrm{d}\beta}{\beta} = \frac{1}{\beta^2}\frac{\mathrm{d}\gamma}{\gamma} = \frac{1}{\beta^2}\frac{\mathrm{d}E}{E} \,.$$

If deviations are small, the approximation $\mathrm{d} \to \Delta$ holds and

$$\frac{\Delta p}{p} \approx \gamma^2 \frac{\Delta v}{v} \approx \gamma^2 \frac{\Delta \beta}{\beta} \approx \frac{1}{\beta^2}\frac{\Delta \gamma}{\gamma} \approx \frac{1}{\beta^2}\frac{\Delta E}{E} \,. \tag{A.1}$$

Table A.1: Relativistic quantities as a function $y = f(x)$ of one other quantity

$f(x)$ \ x	β	γ	E	E_{kin}	p
β	β	$\sqrt{1-\frac{1}{\gamma^2}}$	$\sqrt{1-\left(\frac{m_0c^2}{E}\right)^2}$	$\sqrt{1-\left(\frac{m_0c^2}{E_{\mathrm{kin}}+m_0c^2}\right)^2}$	$\frac{p}{m_0^2c^2+p^2}$
γ	$\frac{1}{\sqrt{1-\beta^2}}$	γ	$\frac{E}{m_0c^2}$	$\frac{E_{\mathrm{kin}}}{m_0c^2}+1$	$\sqrt{\left(\frac{p}{m_0c}\right)^2+1}$
E	$\frac{m_0c^2}{\sqrt{1-\beta^2}}$	γm_0c^2	E	$E_{\mathrm{kin}}+m_0c^2$	$\sqrt{p^2c^2+m_0^2c^4}$
E_{kin}	$m_0c^2\left(\frac{1}{\sqrt{1-\beta^2}}-1\right)$	$(\gamma-1)m_0c^2$	$E-m_0c^2$	E_{kin}	$c\sqrt{p^2+m_0^2c^2}-m_oc^2$
p	$\frac{\beta m_0c}{\sqrt{1-\beta^2}}$	$\sqrt{\gamma^2-1}m_0c$	$\frac{1}{c}\sqrt{E^2-(m_0c^2)^2}$	$\frac{1}{c}\sqrt{E_{\mathrm{kin}}^2+2E_{\mathrm{kin}}m_oc^2}$	p

B Simulation and Beam Experiment Parameters

B.1 General Simulation Examples

If not stated differently the simulation parameters listed in Tab. B.1 where used to obtain the results shown in various plots in this thesis.

Table B.1: General simulation parameters

parameter	value
ion species	$^{238}\mathrm{U}^{73+}$
kinetic energy	$E_{\mathrm{kin}} = 120\,\frac{\mathrm{MeV}}{\mathrm{u}}$
first cavity voltage	$\hat{V}_1 = 5\,\mathrm{kV}$
reference voltage	$V_{\mathrm{R}} = 0$
first cavity harmonic number	$h = 4$
reference revolution frequency	$f_{\mathrm{R}} \approx 641\,\mathrm{kHz}$
coherent synchrotron frequency	$f_{\mathrm{syn,coh}} \approx 870\,\mathrm{Hz}$
particle distribution	parabolic (cf. Tab. 3.1)
bunch size	$\sigma_\varphi \approx 0.90\,\mathrm{rad}$ $\sigma_{\Delta W} \approx 2.08 \cdot 10^{-19}\,\mathrm{Js}$
number of macro-particles	$N = 50{,}000$
number of assumed particles per bunch	$N = 5 \cdot 10^8$
nominal damping of linearized state model	$d_{\mathrm{coh}} = 100\,\frac{1}{\mathrm{s}}$
cavity time constant (modeled as first order lag element)	$T_{\mathrm{cav}} = 20\,\mu\mathrm{s}$
total time delay in the feedback	$T_{\mathrm{D}} = 10\,\mu\mathrm{s}$

B.2 Controller Optimization with Matrix Inequalities

For the optimization of the output feedback (Subsec. 5.4.3) and the state feedback (Sec. 5.5) the following parameter settings were used.

Table B.3: Parameter settings for output and state feedback optimization with matrix inequalities

parameter	value
interface	yalmip version 13-Feb-2013
solver	SeDuMi version 1.3
nominal damping	$d_{\mathrm{coh},0} = 100\,\frac{1}{\mathrm{s}}$

B.3 Beam Experiments

The beam parameters of the experiments conducted on November 21st, 2012 and March 23rd, 2014 are listed in Tab. B.4 and Tab. B.5.

Table B.4: Beam parameters of first experiment from November 21st, 2012

parameter	value
ion species	$^{238}\mathrm{U}^{73+}$
kinetic energy	$E_{\mathrm{kin}} = 120\,\frac{\mathrm{MeV}}{\mathrm{u}}$
first cavity voltage	$\hat{V}_1 = 4\,\mathrm{kV}$
reference voltage	$V_{\mathrm{R}} = 0$
first cavity harmonic number	$h = 4$
reference revolution frequency	$f_{\mathrm{R}} \approx 641\,\mathrm{kHz}$
coherent synchrotron frequency	$f_{\mathrm{syn,coh}} \approx 780\,\mathrm{Hz}$
number of ions per bunch	$N \approx 2.5 \cdot 10^8$

Table B.5: Beam parameters of second experiment from March 23rd, 2014

parameter	value
ion species	$^{86}\mathrm{Kr}^{33+}$
kinetic energy	$E_{\mathrm{kin}} = 120\,\frac{\mathrm{MeV}}{\mathrm{u}}$
first cavity voltage (first/second setting)	$\hat{V}_1 = 6\,\mathrm{kV}/10\,\mathrm{kV}$
reference voltage	$V_{\mathrm{R}} = 0$
first cavity harmonic number	$h = 4$
reference revolution frequency	$f_{\mathrm{R}} \approx 641\,\mathrm{kHz}$
coherent synchrotron frequency	$f_{\mathrm{syn,coh}} \approx 1100\,\mathrm{Hz}/1400\,\mathrm{Hz}$
number of ions per bunch	$N \approx 1.5 \cdot 10^8$

C Model of Central Moments

C.1 Lagrangian Polynomial

The parameters p_l of the Lagrangian fit to the dual-harmonic voltage for $\varphi_\mathrm{R} = 0$ are listed in Tab. C.1.

Table C.1: Parameters of 11th order Lagrangian polynomial

l	p_l	l	p_l
1	0.00001342	9	−0.0006160
3	0.4998	11	0.00001399
5	−0.1246	else	0
7	0.01221		

C.2 Time Derivatives of First and Second Order Moments

With the actuating variables $\Delta\hat{V}_\mathrm{u}$ and $\Delta\varphi_\mathrm{u}$, as well as with the modeling parameters κ_1 and κ_2, the time derivatives of the first and second order central moments derived in Sec. 3.4, assuming a bunch with a parabolic-Gaussian distribution read

$$\dot{m}_{(1,0)} = \kappa_1 m_{(0,1)} \,, \tag{C.1a}$$

$$\begin{aligned}\dot{m}_{(0,1)} =& \kappa_2(1+\Delta\hat{V}_\mathrm{u})\Big[p_1(m_{(1,0)}-\Delta\varphi_\mathrm{u}) \\ &+ p_3\left((m_{(1,0)}-\Delta\varphi_\mathrm{u})^3 + 3(m_{(1,0)}-\Delta\varphi_\mathrm{u})\mu_{(2,0)}\right) \\ &+ p_5\Big((m_{(1,0)}-\Delta\varphi_\mathrm{u})^5 + 10(m_{(1,0)}-\Delta\varphi_\mathrm{u})^3\mu_{(2,0)} \\ &\quad + \frac{75}{7}(m_{(1,0)}-\Delta\varphi_\mathrm{u})\mu_{(2,0)}^2\Big)\end{aligned}$$

$$
\begin{aligned}
&+ p_7\Bigg((m_{(1,0)} - \Delta\varphi_\mathrm{u})^7 + 21(m_{(1,0)} - \Delta\varphi_\mathrm{u})^5 \mu_{(2,0)} \\
&\quad + 75(m_{(1,0)} - \Delta\varphi_\mathrm{u})^3 \mu_{(2,0)}^2 \\
&\quad + \frac{125}{3}(m_{(1,0)} - \Delta\varphi_\mathrm{u}) \mu_{(2,0)}^3 \Bigg) \\
&+ p_9\Bigg((m_{(1,0)} - \Delta\varphi_\mathrm{u})^9 + 36(m_{(1,0)} - \Delta\varphi_\mathrm{u})^7 \mu_{(2,0)} \\
&\quad + 270(m_{(1,0)} - \Delta\varphi_\mathrm{u})^5 \mu_{(2,0)}^2 \\
&\quad + 500(m_{(1,0)} - \Delta\varphi_\mathrm{u})^3 \mu_{(2,0)}^3 \\
&\quad + \frac{1875}{11}(m_{(1,0)} - \Delta\varphi_\mathrm{u}) \mu_{(2,0)}^4 \Bigg) \\
&+ p_{11}\Bigg((m_{(1,0)} - \Delta\varphi_\mathrm{u})^{11} + 55(m_{(1,0)} - \Delta\varphi_\mathrm{u})^9 \mu_{(2,0)} \\
&\quad + \frac{4950}{7}(m_{(1,0)} - \Delta\varphi_\mathrm{u})^7 \mu_{(2,0)}^2 \\
&\quad + 2750(m_{(1,0)} - \Delta\varphi_\mathrm{u})^5 \mu_{(2,0)}^3 \\
&\quad + 3125(m_{(1,0)} - \Delta\varphi_\mathrm{u})^3 \mu_{(2,0)}^4 \\
&\quad + \frac{9375}{13}(m_{(1,0)} - \Delta\varphi_\mathrm{u}) \mu_{(2,0)}^5 \Bigg) \Bigg] , \qquad \text{(C.1b)}
\end{aligned}
$$

$$
\dot{\mu}_{(2,0)} = 2\kappa_1 \mu_{(1,1)} , \qquad \text{(C.1c)}
$$

$$
\begin{aligned}
\dot{\mu}_{(1,1)} =& \kappa_1 \mu_{(0,2)} \\
&+ \kappa_2 (1 + \Delta\hat{V}_\mathrm{u}) \mu_{(2,0)} \\
&\cdot \Bigg[p_1 + p_3 \Bigg(3(m_{(1,0)} - \Delta\varphi_\mathrm{u})^2 + \frac{15}{7}\mu_{(2,0)} \Bigg) \\
&+ p_5 \Bigg(5(m_{(1,0)} - \Delta\varphi_\mathrm{u})^4 + \frac{450}{21}(m_{(1,0)} - \Delta\varphi_\mathrm{u})^2 \mu_{(2,0)} \\
&\qquad + \frac{125}{21}\mu_{(2,0)}^2 \Bigg) \\
&+ p_7 \cdot \frac{1}{33} \Bigg(231(m_{(1,0)} - \Delta\varphi_\mathrm{u})^6 \\
&\qquad + 2475(m_{(1,0)} - \Delta\varphi_\mathrm{u})^4 \mu_{(2,0)} \\
&\qquad + 4125(m_{(1,0)} - \Delta\varphi_\mathrm{u})^2 \mu_{(2,0)}^2 + 625\mu_{(2,0)}^3 \Bigg)
\end{aligned}
$$

$$
\begin{aligned}
&+ p_9 \cdot \frac{3}{143}\Big(429(m_{(1,0)} - \Delta\varphi_\mathrm{u})^8 \\
&\qquad + 8580(m_{(1,0)} - \Delta\varphi_\mathrm{u})^6 \mu_{(2,0)} \\
&\qquad + 35750(m_{(1,0)} - \Delta\varphi_\mathrm{u})^4 \mu_{(2,0)}^2 \\
&\qquad + 32500(m_{(1,0)} - \Delta\varphi_\mathrm{u})^2 \mu_{(2,0)}^3 + 3125\mu_{(2,0)}^4\Big) \\
&+ p_{11} \cdot \frac{1}{91}\Big(1001(m_{(1,0)} - \Delta\varphi_\mathrm{u})^{10} \\
&\qquad + 32175(m_{(1,0)} - \Delta\varphi_\mathrm{u})^8 \mu_{(2,0)} \\
&\qquad + 250250(m_{(1,0)} - \Delta\varphi_\mathrm{u})^6 \mu_{(2,0)}^2 \\
&\qquad + 568750(m_{(1,0)} - \Delta\varphi_\mathrm{u})^4 \mu_{(2,0)}^3 \\
&\qquad + 328125(m_{(1,0)} - \Delta\varphi_\mathrm{u})^2 \mu_{(2,0)}^4 + 21875\mu_{(2,0)}^5\Big)\Big], \qquad \text{(C.1d)}
\end{aligned}
$$

$$
\begin{aligned}
\dot{\mu}_{(0,2)} =& 2 \cdot \kappa_2 (1 + \Delta\hat{V}_\mathrm{u}) \mu_{(1,1)} \\
&\cdot \Big[p_1 + p_3 \cdot 3(m_{(1,0)} - \Delta\varphi_\mathrm{u})^2 + p_5 \cdot 5(m_{(1,0)} - \Delta\varphi_\mathrm{u})^4 \\
&+ p_7 \cdot 7(m_{(1,0)} - \Delta\varphi_\mathrm{u})^6 + p_9 \cdot 9(m_{(1,0)} - \Delta\varphi_\mathrm{u})^8 \\
&+ p_{11} \cdot 11(m_{(1,0)} - \Delta\varphi_\mathrm{u})^{10}\Big]. \qquad \text{(C.1e)}
\end{aligned}
$$

C.3 Higher Order Moments for Parabolic-Gaussian Distribution

Assuming the bunch to be parabolic-Gaussian distributed according to Tab. 3.1, the central moments of order $n = n_x + n_y > 2$ can be expressed as functions of second order moments as listed in Tab. C.2.

Table C.2: Higher order moments as functions of second order moments

$n_x + n_y$	central moments
3	$\mu_{(n_x,n_y)} = 0$

4	$\mu_{(4,0)} = \frac{75}{35}\mu_{(2,0)}^2\,, \quad \mu_{(3,1)} = 0\,, \quad \mu_{(2,2)} = \mu_{(2,0)}\mu_{(0,2)}\,,$ $\mu_{(1,3)} = 0\,, \quad \mu_{(0,4)} = 3\mu_{(0,2)}^2$
5	$\mu_{(n_x,n_y)} = 0$
6	$\mu_{(6,0)} = \frac{125}{21}\mu_{(2,0)}^3\,, \quad \mu_{(5,1)} = 0\,, \quad \mu_{(4,2)} = \frac{15}{7}\mu_{(2,0)}^2\mu_{(0,2)}\,,$ $\mu_{(3,3)} = 0\,, \quad \mu_{(2,4)} = 3\mu_{(2,0)}\mu_{(0,2)}^2\,, \quad \mu_{(1,5)} = 0\,,$ $\mu_{(0,6)} = 15\mu_{(0,2)}^3$
7	$\mu_{(n_x,n_y)} = 0$
8	$\mu_{(8,0)} = \frac{625}{33}\mu_{(2,0)}^4\,, \quad \mu_{(7,1)} = 0\,, \quad \mu_{(6,2)} = \frac{125}{21}\mu_{(2,0)}^3\mu_{(0,2)}\,,$ $\mu_{(5,3)} = 0\,, \quad \mu_{(4,4)} = \frac{225}{35}\mu_{(2,0)}^2\mu_{(0,2)}^2\,, \quad \mu_{(3,5)} = 0\,,$ $\mu_{(2,6)} = 15\mu_{(2,0)}\mu_{(0,2)}^3\,, \quad \mu_{(1,7)} = 0\,, \quad \mu_{(0,8)} = 105\mu_{(0,2)}^4$
9	$\mu_{(n_x,n_y)} = 0$
10	$\mu_{(10,0)} = \frac{9375}{143}\mu_{(2,0)}^5\,, \quad \mu_{(9,1)} = 0\,, \quad \mu_{(8,2)} = \frac{625}{33}\mu_{(2,0)}^4\mu_{(0,2)}\,,$ $\mu_{(7,3)} = 0\,, \quad \mu_{(6,4)} = \frac{125}{7}\mu_{(2,0)}^3\mu_{(0,2)}^2\,, \quad \mu_{(5,5)} = 0\,,$ $\mu_{(4,6)} = \frac{225}{7}\mu_{(2,0)}^2\mu_{(0,2)}^3\,, \quad \mu_{(3,7)} = 0\,,$ $\mu_{(2,8)} = 105\mu_{(2,0)}\mu_{(0,2)}^4\,, \quad \mu_{(1,9)} = 0\,, \quad \mu_{(0,10)}^2 = 945\mu_{(0,2)}^5$
11	$\mu_{(n_x,n_y)} = 0$
12	$\mu_{(12,0)} = \frac{3125}{13}\mu_{(2,0)}^6\,, \quad \mu_{(11,1)} = 0\,,$ $\mu_{(10,2)} = \frac{9375}{143}\mu_{(2,0)}^5\mu_{(0,2)}\,, \quad \mu_{(9,3)} = 0\,,$ $\mu_{(8,4)} = \frac{625}{11}\mu_{(2,0)}^4\mu_{(0,2)}^2\,, \quad \mu_{(7,5)} = 0\,,$ $\mu_{(6,6)} = \frac{625}{7}\mu_{(2,0)}^3\mu_{(0,2)}^3\,, \quad \mu_{(5,7)} = 0\,,$ $\mu_{(4,8)} = 45\mu_{(2,0)}^2\mu_{(0,2)}^4\,, \quad \mu_{(3,9)} = 0\,,$ $\mu_{(2,10)}^2 = 945\mu_{(2,0)}\mu_{(0,2)}^5\,, \quad \mu_{(1,11)} = 0\,,$ $\mu_{(0,12)}^2 = 10395\mu_{(0,2)}^6$

Bibliography

[1] FAIR - Facility for Antiproton and Ion Research. online: https://www.gsi.de/forschung_beschleuniger/fair.htm, June 2013.

[2] Fermilab's Tevatron. online: https://www.fnal.gov/pub/science/accelerator/, December 2013.

[3] GSI Helmholtzzentrum für Schwerionenforschung GmbH. online: https://www.gsi.de/, May 2014.

[4] SeDuMi. online: http://coral.ie.lehigh.edu/~newsedumi/, February 2014.

[5] Yalmip. online: http://users.isy.liu.se/johanl/yalmip/, February 2014.

[6] A. M. Al-khateeb, O. Boine-Frankenheim, I. Hofmann, and G. Rumolo. Analytical Calculation of the Longitudinal Space Charge and Resistive Wall Impedances in a Smooth Cylindrical Pipe. *Physical Review E*, 63:026503/1 – 026503/8, 2001.

[7] F. Amato. *Robust Control of Linear Systems Subject to Uncertain Time-Varying Parameters*. Springer-Verlag Berlin Heidelberg, 2006.

[8] S. Appel. *Simulation und Messung longitudinaler Raumladungseffekte in intensiven Ionenstrahlen im SIS18 Synchrotron*. PhD thesis, TU Darmstadt, 2011.

[9] V. L. Bageshwar and F. Borrelli. Observer Pole Placement Limitations for a Class of Offset-Free Model Predictive Controllers. In *Proc. of 2008 American Control Conference*, 2008.

[10] B. R. Barmish. Necessary and Sufficient Conditions for Quadratic Stabilizabilty of an Uncertain System. *Journal of Optimization Theory and Applications*, 46(4):399 – 408, 1985.

[11] J.-L. Basdevant. *Variational Principles in Physics*. Springer Science+Business Media, LLC, New York, 2007.

[12] C. M. Bhat, F. Caspers, H. Damerau, S. Hancock, E. Mahner, and F. Zimmermann. Stabilizing Effect of a Double-Harmonic RF System in the CERN PS. In *Proc. of 2009 Particle Accelerator Conference*, 2009.

[13] C. K. Birdsall and A. B. Langdon. *Plasma Physics via Computer Simulation.* Taylor and Francis Group, New York, 2005.

[14] O. Boine-Frankenheim and I. Hofmann. Space Charge Effects and Coherent Stability Limits in Barrier Buckets. *Physical Review Special Topics - Accelerators and Beams*, 6:034207/1 – 034207/10, 2003.

[15] O. Boine-Frankenheim and T. Shukla. Space Charge Effects in Bunches for Different RF Wave Forms. *Physical Review Special Topics - Accelerators and Beams*, 8(3):034201/1 – 034201/14, 2005.

[16] D. Boussard. Design of a Ring RF System. Technical Report CERN SL/91-2, Conseil Européen pour la Recherche Nucléaire (CERN), 1991.

[17] C. Bovet, R. Gouiran, I. Gumowski, and K. H. Reich. A Selection of Formulae and Data Useful for the Design of A. G. Synchrotrons. Technical Report CERN-MPS-SI-INT-DL-70-4, Conseil Européen pour la Recherche Nucléaire (CERN), April 1970.

[18] S. Boyd, L. El Ghaoui, E. Feron, and V. Balakrishnan. *Linear Matrix Inequalities in System and Control Theory.* SIAM, 1994.

[19] J. M. Brennan. The RF Beam Control System for the Brookhaven AGS Synchrotron. In *Proc. of XVth International Conference on High Energy Accelerators*, 1992.

[20] J. M. Brennan, A. Campbell, J. DeLong, T. Hayes, E. Onillon, J. Rose, and K. Vetter. RF Beam Control System for the Brookhaven Relativistic Heavy Ion Collider, RHIC. In *Proc. of 1998 European Particle Accelerator Conference*, 1998.

[21] D. Bug. Dämpfung der longitudinalen Dipolschwingung in Schwerionen-Synchrotrons durch FIR-Filter im Fall doppeltharmonischer Beschleunigungsspannungen. Bachelor's Thesis, TU Darmstadt, 2012.

[22] A. W. Chao. *Physics of Collective Beam Instabilities in High Energy Accelerators.* John Wiley & Sons, INC., 1993.

[23] A. W. Chao and M. Tigner, editors. *Handbook of Accelerator Physics and Engineering*. World Scientific Publishing Co. Pte. Ltd. Singapore, 1999.

[24] M. Chilali and P. Gahinet. H_∞ Design with Pole Placement Constraints: an LMI Approach. *IEEE Transactions on Automatic Control*, 41(3):358 – 367, 1996.

[25] C. K. Chui and G. Chen. *Kalman Filtering with Real-Time Applications*. Springer-Verlag Berlin Heidelberg, 2009.

[26] E. D. Courant, H. S. Snyder, and M. S. Livingston. The Strong-Focusing Synchrotron - A New High Energy Accelerator. *Pysical Review*, 88:1190 – 1196, 1952.

[27] J. Eschke. International Facility for Antiproton and Ion Research (FAIR) at GSI and Darmstadt. *Journal of Physics G: Nuclear and Particle Physics*, 31:967 – 973, 2005.

[28] L. Evans, editor. *The Large Hydron Collider: a Marvel of Technology*. Taylor and Francis Group, LLC, Boca Raton, 2009.

[29] O. Föllinger. *Regelungstechnik - Einführung in die Methoden und ihre Anwendung*. Hüthig Verlag Heidelberg, 2008.

[30] B. Franczak. SIS Parameter List. Technical Report GSI-SIS-TN/ 87-13, GSI Helmholtzzentrum für Schwerionenforschung GmbH, 1987.

[31] T. Frey and M. Bossert. *Signal- und Systemtheorie*. B. G. Teubner Verlag, 2004.

[32] L. El Ghaoui and V. Balakrishnan. Synthesis of Fixed-Structure Controllers via Numerical Optimization. In *Proc. of 33rd Conference on Decision and Control*, Lake Buena Vista, USA, 1994.

[33] J. Ginsberg. *Engineering Dynamics*. Cambridge University Press, New York, 2008.

[34] K. Groß, H. Klingbeil, and D. Lens. Impact of Simplified Stationary Cavity Beam Loading on the Longitudinal Feedback System for SIS100. In *Proc. of 5th International Particle Accelerator Conference*, 2014.

[35] T. T. Ha. *Theory and Design of Digital Communication Systems*. Cambridge University Press, Cambridge, 2011.

[36] R. W. Hamm and M. E. Hamm, editors. *Industrial Accelerators and their Applications*. World Scientific Publishing Co. Pte. Ltd. Singapore, 2012.

[37] S. Hanna. *RF Linear Accelerators for Medical and Industrial Applications*. Artech House, Norwood, 2012.

[38] U. Hartel. Modellierung des Regelungs- und Steuerungssystems einer Beschleunigungseinheit für Synchrotrons. Master's thesis, TU Darmstadt, 2011.

[39] A. Hassibi, J. How, and S. Boyd. A Path-Following Method for Solving BMI Problems in Control. In *Proc. of 1999 American Control Conference*, volume 2, pages 1385–1389, San Diego, USA, 1999.

[40] L. Heil and U. Hartel. Realisierung eines schaltbaren Verstärkers für Strahlstrommonitore - FCT Verstärkerschaltung. Technical Report 11102013, GSI Helmholtzzentrum für Schwerionenforschung GmbH, 2013.

[41] F. Hinterberger. *Physik der Teilchenbeschleuniger*. Springer-Verlag Berlin Heidelberg, 2008.

[42] A. Hofmann. Landau Damping. In *Proc. of 2003 CERN Accelerator School: Intermediate Course on Accelerator Physics (CERN 2006-002)*, 2003.

[43] A. Hofmann and F. Pedersen. Bunches with Local Elliptic Energy Distribution. *IEEE Transactions on Nuclear Science*, 26(3):3526 – 3528, 1979.

[44] R. A. Howland. *Intermediate Dynamics: A Linear Algebraic Approach*. Springer Science+Business Media, Inc., New York, 2006.

[45] G. Kalisch. *Erzeugung und Untersuchung gepulster Schwerionen-Strahlen höchster Phasenraumdichte im Experimentier-Speichering der GSI*. PhD thesis, TU Darmstadt, 1993.

[46] D. W. Kerst and R. Serber. Electronic Orbits in the Induction Accelerator. *Physical Review*, 60:53 – 58, 1941.

[47] H. Klingbeil. A Fast DSP-Based Phase-Detector for Closed-Loop RF Control in Synchrotrons. *IEEE Transactions on Instrumentation and Measurement*, 54(3):1209 – 1213, 2005.

[48] H. Klingbeil. DSP Software Implementation, Draft 2.20. Technical report, GSI Helmholtzzentrum für Schwerionenforschung GmbH, 2012.

[49] H. Klingbeil. Acceleration of Charged Particles in Electromagnetic Fields. Lecture Notes, TU Darmstadt, 2013.

[50] H. Klingbeil, U. Laier, and D. Lens. *Theoretical Foundations of Synchrotron and Storage Ring RF Systems.* Springer-Verlag Cham Heidelberg New York Dordrecht London, 2015.

[51] H. Klingbeil, D. Lens, M. Mehler, and B. Zipfel. Modeling Longitudinal Oscillations of Bunched Beams in Synchrotrons. *[physics.acc-ph]*, 2010. Published online: arXiv:1011.3957v1.

[52] H. Klingbeil, B. Zipfel, M. Kumm, and Peter Moritz. A Digital Beam-Phase Control System for Heavy-Ion Synchrotrons. *IEEE Transactions on Nuclear Science*, 54(6):2604 – 2610, 2007.

[53] U. Konigorski. A New Direct Approach to the Design of Structurally Constrained Controllers. In *Preprints of 10th IFAC World Congress on Automatic Control*, Munich, Germany, 1987.

[54] U. Konigorski. *Ein direktes Verfahren zum Entwurf strukturbeschränkter Zustandsrückführungen durch Polvorgabe.* VDI Verlag GmbH Düsseldorf, 1988.

[55] S. Koscielniak. Longitudinal Space-Charge Geometric Factor for an Elliptical Beam. In *Proc. of 2001 Particle Accelerator Conference*, 2001.

[56] S. Koscielniak. LONG1D User's Guide. Technical Report TRI-DN-97-12, Tri University Meson Facility (TRIUMF), 2003.

[57] B. Kriegbaum and F. Pedersen. Electronics for the Longitudinal Active Damping System for the CERN PS Booster. *IEEE Transactions on Nuclear Science*, 24(3):1695 – 1697, 1977.

[58] C. H. Kuo, W. K. Lau, M. S. Yeh, K. H. hu, D. Lee, M. H. Wang, P. J. Chou, D. Lee, S. Y. Hsu, J. Chen, C. J. Wang, K. T. Hsu, K. Kobayashi, T. Nakamura, and M. Dehler. FPGA-Based Longitudinal Bunch-by-Bunch Feedback System for TLS. In *Proc. of 2006 European Particle Accelerator Conference*, 2006.

[59] J. L. Laclare. Introduction to Coherent Instabilities. In *Proc. of 1985 CERN Accelerator School: General Accelerator Physics (CERN 85-19), Vol. 2*, 1985.

[60] L. D. Landau. On the Vibration of the Electronic Plasma. *Journal of Physics USSR*, 10:25 – 34, 1946.

[61] S. Y. Lee. *Accelerator Physics.* World Scientific Publishing Co. Pte. Ltd. Singapore, 2004.

[62] D. Lens. *Modeling and Control of Longitudinal Single-Bunch Oscillations in Heavy-Ion Synchrotrons.* VDI Verlag GmbH Düsseldorf, 2012.

[63] D. Lens and H. Klingbeil. Stability of Longitudinal Bunch Length Feedback for Heavy-Ion Synchrotrons. *Physical Review Special Topics - Accelerators and Beams*, 16(3), 2013. Published online, DOI: 10.1103/PhysRevSTAB.16.032801.

[64] N. Levanon and E. Mozeson. *Radar Signals.* John Wiley & Sons, INC., 2004.

[65] J. Löfberg. YALMIP: A Toolbox for Modeling and Optimization in MATLAB. In *Proc. of 2004 IEEE International Symposium on Computer Aided Control Systems Design*, pages 284–289, Taipei, Taiwan, 2004.

[66] D. Lipka. *Untersuchungen zum longitudinalen Phasenraum an einem Photoinjektor für minimale Strahlemittanz.* PhD thesis, Humboldt-Universität Berlin, 2004.

[67] J.-K. Lu. *Boundary Value Problems for Analytic Functions.* World Scientific Publishing Co. Pte. Ltd. Singapore, 1993.

[68] J. Lunze. *Regelungstechnik 2.* Springer-Verlag Berlin Heidelberg, 2010.

[69] R. Lyons. Improved narrowband low-pass IIR filters in fixed-point systems [DSP Tips & Tricks]. *IEEE Signal Processing Magazine*, 26(2):128, 130, 132, 2009.

[70] J. A. MacLachlan. Particle Tracking in E-ϕ Space as a Design Tool for Cyclic Accelerators. In *Proc. of 12th IEEE Particle Accelerator Conference*, 1987.

[71] B. R. Mahafza. *Radar Systems Analysis and Design Using MATLAB ®, 2nd Edition*. Chapman & Hall/CRC, 2005.

[72] M. Manderla. *Eine Methodik zum Regler- und Beobachterentwurf für Mehrgrößensysteme in Deskriptorform*. VDI Verlag GmbH Düsseldorf, 2011.

[73] E. M. McMillan. The Synchrotron - A Proposed High Energy Particle Accelerator. *Physical Review*, 68:143 – 144, 1945.

[74] D. Moss. *Biomedical Applications of Synchrotron Infrared Microspectroscopy: A Practical Approach*. Royal Society of Chemistry, Cambridge, 2011.

[75] R. B. Neal, editor. *The Stanford Two-Mile Accelerator*. W. A. Benjamin Inc., New York, 1968.

[76] K. Y. Ng. *Physics of Intensity Dependent Beam Instabilities*. World Scientific Publishing Co. Pte. Ltd. Singapore, 2006.

[77] K.-P. Ningel, P. Hülsmann, H. Klingbeil, U. Laier, C. Thielmann, and B. Zipfel. Dual Harmonic Operation at SIS18. In *Proc. of 1st International Particle Accelerator Conference*, 2010.

[78] A. Papoulis and S. Pillai. *Probability, Random Variables and Stochastic Processes*. McGraw-Hill, New York, 2002.

[79] F. Pedersen. *Frontiers of Particle Beams: Factories with e^+ e^- Rings*, volume 425 of *Lecture Notes in Physics*, chapter Multibunch instabilities, pages 269–292. Springer-Verlag Berlin Heidelberg, 1994.

[80] F. Pedersen and F. J. Sacherer. Theory and Performance of the Longitudinal Active Damping System for the CERN PS Booster. *IEEE Transactions on Nuclear Science*, 24(3):1396 – 1398, 1977.

[81] I. Percival and D. Richards. *Introduction to Dynamics*. Cambridge University Press, New York, 1982.

[82] S. Poornachandra and B. Sasikala. *Digital Signal Processing*. Tata McGraw Hill Education Private Limited, New Delhi, 2010.

[83] D. C. W. Ramos and P. L. D. Peres. An LMI Condition for the Robust Stability of Uncertain Continuous-Time Linear Systems. *IEEE Transactions on Automatic Control*, 47(4):675 – 678, 2002.

[84] W. C. Röntgen. *Eine neue Art von Strahlen (On a New Kind of Rays)*. Stahel'sche K. Hof- und Universitäts- Buch- und Kunsthandlung, 1895.

[85] F. J. Sacherer. RMS Envelope Equations with Space Charge. *IEEE Transactions on Nuclear Science*, 18(3):1105 – 1107, 1971.

[86] F. J. Sacherer. A Longitudinal Stability Criterion for Bunched Beams. *IEEE Transactions on Nuclear Science*, 20(3):825 – 829, 1973.

[87] K. Schindl. Instabilities. In *Proc. 2003 CERN Accelerator School: Intermediate Course on Accelerator Physics (CERN 2006-002)*, 2003.

[88] K. Schindl. Space Charge. In *Proc. 2003 CERN Accelerator School: Intermediate Course on Accelerator Physics (CERN 2006-002)*, 2003.

[89] D. Schlichthärle. *Digital Filters*. Springer-Verlag Berlin Heidelberg, 2011.

[90] J. Stoer. *Introduction to Numerical Analysis*. Springer-Verlag New York, 2002.

[91] J. F. Sturm. Using SeDuMi 1.02, a MATLAB toolbox for optimization over symmetric cones. *Optimization Methods and Software*, 11–12:625 – 653, 1999.

[92] F. Tamura, A. Schnase, M. Yoshii, C. Ohmori, M. Yamamoto, M. Nomura, M. Toda, H. Suzuki, T. Shimada, K. Hara, and K. Hasegawa. Dual-Harmonic Phase Control in the J-PARC RCS. In *Proc. of 1st International Particle Accelerator Conference*, 2010.

[93] C. Y. Tan and J. Steimel. The Tevatron Bunch by Bunch Longitudinal Dampers. In *Proc. of 2003 Particle Accelerator Conference*, 2003.

[94] K. C. Toh, M.J. Todd, and R. H. Tütüncü. SDPT3 – a MATLAB software package for semidefinite programming. *Optimization Methods and Software*, 11:545 – 581, 1999.

[95] R. H. Tütüncü, K. C. Toh, and M. J. Todd. Solving semidefinite-quadratic-linear programs using SDPT3. *Mathematical Programming*, 95:189 – 217, 2003.

[96] V. I. Veksler. A New Method of Acceleration of Relativistic Particles. *Journal of Physics USSR*, 9:153 – 158, 1945.

[97] J. G. Wang, H. Suk, D. X. Wang, and M. Reiser. Determination of the Geometry Factor for Longitudinal Perturbations in Space-Charge Dominated Beams. *Pysical Review Letters*, 72(13):2029 – 2032, 1994.

[98] H. Wiedemann. *Particle Accelerator Physics*. Springer-Verlag Berlin Heidelberg, 2007.

[99] K. Wille. *The Physics of Particle Accelerators*. Oxford University Press, Oxford, 2000.

[100] S. Y. Zhang and W. T. Weng. Analysis of Acceleration Control Loops of a Synchrotron. *Nuclear Instruments and Methods in Physics Research*, A317:405 – 412, 1992.

[101] F. Zimmermann and K. Oide. Resistive-wall Wake and Impedances for Non-ultrarelativistic Beams. Technical Report CERN-AB-2004-015(ABP), Conseil Européen pour la Recherche Nucléaire (CERN), 2004.

[102] B. Zipfel. Fiber Optical Splitter. GSI internal note, August 2013.

[103] B. W. Zotter and S. A. Kheifets. *Impedances and Wakes in High-Energy Particle Accelerators*. World Scientific Publishing Co. Pte. Ltd. Singapore, 2000.

Publications

[104] M. Alhumaidi, J. Grieser, and A. M. Zoubir. Determination of Optics Transfer between the Kicker and BPMs for Transverse Feedback System. In *Proc. of 4th International Particle Accelerator Conference*, 2013.

[105] S. Gering, J. Grieser, and A. Wahrburg. Using LMIs to Optimize Robustness of Observer-based State-feedback for a Synchrotron. *International Journal of Robust and Nonlinear Control*, 2013. Published online, DOI: 10.1002/rnc.3066.

[106] J. Grieser, J. Adamy, T. Ferrand, K. Groß, U. Hartel, H. Klingbeil, U. Laier, D. Lens, K.-P. Ningel, S. Schäfer, and B. Zipfel. A Digital Beam-Phase Control System for a Heavy-Ion Synchrotron with a Dual-Harmonic Cavity System. *IEEE Transactions on Nuclear Science*, 61(6):3584 – 3591, 2014.

[107] J. Grieser, D. Bug, H. Klingbeil, and J. Adamy. Comparison of Filter Designs for a Digital Beam-Phase Feedback System in a Heavy-Ion Synchrotron. In *Proc. of 21st Mediterranean Conference on Control and Automation*, 2013.

[108] J. Grieser and H. Klingbeil. Beam Experiment: Dual-Harmonic Beam Phase Control in SIS18. Technical Report 1902014, GSI Helmholtzzentrum für Schwerionenforschung GmbH, 2014.

[109] J. Grieser, H. Klingbeil, and J. Adamy. Fuzzy Controller for Beam Stabilization in a Heavy-Ion Synchrotron. In *Proc. of 2nd International Conference on Instrumentation, Control and Automation*, 2011.

[110] J. Grieser, D. Lens, U. Hartel, H. Klingbeil, U. Laier, K.-P. Ningel, S. Schäfer, and B. Zipfel. A Digital Beam Phase Control System for a Heavy-Ion Synchrotron with a Double-Harmonic Cavity System. In *Proc. of 4th International Particle Accelerator Conference*, 2013.

[111] J. Grieser, D. Lens, H. Klingbeil, and J. Adamy. A Method to Obtain the Frequency of the Longitudinal Dipole Oscillation for Modeling and Control in Synchrotrons with Single or Double Harmonic RF Systems. In *Proc. of 3rd International Particle Accelerator Conference*, 2012.

[112] U. Hartel, J. Grieser, H. Klingbeil, U. Laier, D. Lens, K.-P. Ningel, S. Schäfer, and B. Zipfel. Precise Verification of Phase and Amplitude Calibration by Means of a Debunching Experiment in SIS18. In *Proc. of 4th International Particle Accelerator Conference*, 2013.

[113] H. Klingbeil and J. Grieser. Beam Experiment: Dual-Harmonic Beam Phase Control in SIS18. Technical Report 07012013, GSI Helmholtzzentrum für Schwerionenforschung GmbH, 2012.

[114] D. Lens, J. Grieser, and H. Klingbeil. Longitudinal Closed-Loop beam control in Heavy-Ion Synchrotrons: Simulation Methods and Results. In *SimTech2011 - International Conference on Simulation Technology 2011*, 2011.

Curriculum Vitae

Personal Details	
Name	Jochen Michael Grieser
Date and place of birth	April 5th, 1984 in Göppingen

Education and Work Experience	
since 2014	Development engineer at ITK Engineering AG
2010 – 2014	PhD student at Technische Universität Darmstadt, Institute for Automation and Control, Control Methods and Robotics lab, in cooperation with GSI Helmholtzzentrum für Schwerionenforschung GmbH
2008	Student (electrical engineering, specialization: automation and control) at Lunds Tekniska Högskola, Sweden
2004 – 2010	Student (electrical engineering, specialization: automation and control) at Uni Ulm, degree: Dipl.-Ing.
2003 – 2004	Civil service at Samariterstiftung Geislingen/Steige
2003	Baccalaureate at Helfenstein-Gymnasium Geislingen/Steige